

# Examination of high energy electron diffraction in strained crystals using adiabatic iteration theory

Kelly, Mark

*Award date:*
1993

*Awarding institution:*
University of Bath

# EXAMINATION OF HIGH ENERGY ELECTRON DIFFRACTION IN STRAINED CRYSTALS USING ADIABATIC ITERATION THEORY

submitted by Mark Kelly

for the degree of Doctor of Philosophy

of the University of Bath

1993

## COPYRIGHT



M Kelly





ProQuest LLC
789 East Eisenhower Parkway
P.O. Box 1346
Ann Arbor, MI 48106-1346

## ABSTRACT

This thesis contains an examination of the effects of strain fields upon electron propagation in transmission electron microscopy. Two particular examples of such High Energy Electron Diffraction (HEED) microscopes, large angle convergent beam diffraction and scanning transmission electron microscopes, are used to illustrate the various effects strained crystals may have in transmission electron microscopy The particular strain fields to be examined are dislocations.

Chapter 1 gives a brief introduction to the advantages and disadvantages of HEED as a crystallographic tool and to the mathematical technique, adiabatic iteration, to be used to approximate solutions analytically.

The usual starting equations for governing HEED are derived in chapter 2, highlighting the various standard approximations generally made. These equations are shown to be equivalent to the low-energy Schrödinger equation and will be the basis for forming theoretical HEED images in chapters 4 and 5. The chapter also contains a derivation of the modified Bloch wave theory (to be used later in conjunction with the adiabatic theory) and a discussion of dislocations (used as a particular example of strain fields).

A general nxn matrix adiabatic iteration scheme , based on that of Berry (1987), is derived in chapter 3. The more simple 2x2 matrix case is discussed in more detail. The relevance of the adiabatic iteration as an approximation technique in TEM is then discussed. The chapter ends with a discussion of Berry's geometrical phase (1984).

Two specific examples of the affects of strain fields upon HEED images are examined in the following two chapters. In chapter 4 Large Angle Convergent

Beam Electron Diffraction (LACBED) is introduced and the simple 2x2 matrix adiabatic iteration scheme is used to form approximate LACBED images for a number of differing cases. In chapter 5 the general adiabatic iteration scheme is used to illustrated strain effects upon High Angle Annular Dark Field (HAADF) imaging in Scanning Transmission Electron Microsopy (STEM).

## ACKNOWLEDGEMENTS

I should like to take this opportunity to express my gratitude and thanks to David Bird. His understanding, patience and enthusiatic supervision have been the major factors in completing this thesis. I would also like to thank David for his repeated reading and the many suggestions for the improvement of this thesis. All of the successes contained within are due, to a large degree, to David, whilst any mistakes are of my own making.

Other people to whom I am also grateful for their help and consideration include David Jesson, for providing a number of experimental images at my request, Dick James for kind permission to reproduce his derivation of the undeformed scattering potential in section 2.1 and figures 2.1, 2.2 & 4.1, and Ali Bari for reading and commenting upon this research, and all of the members of the School of Physics.

I would also like to thank the School of Physics for their help, and the University of Bath for the unlimited use of computing facilities. Finally I should like to thank SERC for their financial support.

## CONTENTS

# CHAPTER 1

# INTRODUCTION.

In this thesis we will be investigating electron propagation in srained crystals and the variety of effects this can cause. We shall restrict ourselves to looking only at High Energy Electron Diffraction (HEED) in Transmission Electron Microscopy (TEM). We shall only concern ourselves with TEM theory and not with actual experimental details, other than to observe that various experimental techniques do exist and are used, and to compare and contrast our findings with those from experiments. Wherever possible we shall keep the results general, so that they are applicable to a wide range of related situations. Specific cases will be examined in order to better illustrate the general results. Thus chapter 2 deals with deriving the general equations governing HEED and chapter 3 shows how the adiabatic iteration scheme (Berry 1987) can be used to approximate a solution to a Schrödinger equation with a general hermitian Hamiltonian. Two specific examples of the effects of strain fields in TEM are then looked at the following 2 chapters.

Real crystals are almost always imperfect in some manner. Such imperfections may include point or surface defects, as well as line defects such as dislocations, all of which can have important effects upon the nature of the crystal. For example the mechanical and plasticity properties of many materials are greatly influenced by dislocations. The type of strain field we shall be using, will almost exclusively be that due to a dislocation. The nature and influence of dislocations in crystalline specimens is discussed in section 2.8. Although a number of techniques exist to study dislocations (or other strain fields), such as etching,

decoration methods, x-ray and neutron diffraction (Friedel 1964), we shall only be concerned with TEM.

TEM has a number of advantages, and naturally disadvantages, for studying strain fields over other techniques. These arise because electrons are strongly affected by electro-magnetic forces. This has important consequences both for the microscope and for electron interactions within the crystal specimen itself. Inside the microscope, by using a thermonic or field emission gun system, it is possible to produce a controlled stream of electrons with well defined energies and small wavelengths of less than atomic spacings (Reimer 1984). Electro-magnetic lenses can be used not only to magnify, but also to focus and deflect the electron beam. It is thus possible to form a convergent beam and to position the beam on the desired specimen area. Because we are interested in a theoretical study of TEM we shall not concern ourselves with the actual workings of any particular microscope. As electrons have such strong interactions with atoms, thereby undergoing multiple scattering in TEM, an electron diffraction pattern (a map of the spatial distribution of scattered electrons) contains a great amount of useful information about the arrangement of atoms in the specimen. Indeed one of the problems in TEM is not the lack of information in an electron diffraction pattern, but rather its over abundance, leading to extremely difficult problems in interpretation. A second problem is that electrons do not penetrate far into solids, so that the thickness of materials studied is limited to the range $\sim$ 100 to 1000 nm. TEM is hence restricted to studying materials which may be prepared in very thin slices.

Although the equations governing HEED can be solved exactly for perfect un-

strained crystals or computationally for strained crystals, in order to obtain an analytical solution, approximation techniques must be employed. The particular analytical technique we shall be using to approximate the solution to the governing HEED equations is adiabatic iteration (Berry 1987). As Berry (1984) has shown, and will be discussed further in section 3.3, the phase of an adiabatically evolving system around a closed path contains not only the familar dynamical but also a geometric part. The geometric phase is a function only of the path taken and not of the time taken to traverse the path. In a second paper Berry (1987) has included small non adiabatic correction terms which are due to the finite time taken to travel the path. By using an iteration scheme under approximate adiabatic conditions, successively better approximations can be made to the geometric phase, and so to the system's wavefunction.

As we shall analyse in chapters 3 and 4, Bird and Preston (1988) have shown that the effects of the geometric phase can be observed in TEM. Using both the adiabatic iteration scheme and the modified Bloch wave technique (discussed in section 2.7) they have shown that the familiar fringe bending upon crossing a dislocation in a 2-beam electron diffraction pattern can be interpreted in terms of the geometric phase. Here in thesis we shall extend their work in two directions. First in chapter 3 we shall derive the general n-beam matrix adiabatic iteration scheme and in chapter 5 illustrate its use in TEM, whilst in chapter 4 we shall investigate the usefulness of making further iterations in an attempt to make better approximations.

# CHAPTER 2

# HIGH ENERGY ELECTRON DIFFRACTION.

In this chapter the equations which govern high energy electron diffraction (HEED) are derived. These equations will form the basis for the formation and interpretation of the theoretical electron micrographs to be used in later chapters. The equations will be derived by making a number of conventional approximations, which are discussed in sections 2.1 to 2.4. Two particular cases will be looked at, first in section 2.5, the two beam case, in which there is considered to be only one diffracted beam. Next in section 2.6 the general case where an unlimited number of diffracted beams is considered. Then in section 2.7 a modified transformation is discussed. This will be used in later chapters to find better appoximations to the solutions of the HEED equations for strained crystals. Finally in section 2.8 the type of strain field to be used in actual calculations is introduced.

## 2.1 THE SCATTERING POTENTIAL.

The potential seen by an incident electron should in principle include the effects from every crystal electron and nucleus, both as individual scatterers and as part of collective excitations. Fortunately there are features of HEED which make the construction of a realistic and usable scattering potential somewhat easier than first appears. The first of these is that the incident electron is distinguishable from the crystal electrons by its high kinetic energy (typically 200keV). This means that the probability of exchange between an incident and a crystal electron is negligible and so exchange effects may be ignored in the

construction of the scattering potential $V$ (Dederichs 1972).

The second feature is that the majority of scattering events are elastic and contribute to the intensity diffracted into Bragg beams. It is these Bragg beams that contain nearly all of the information of interest in crystallography, so most of the important details may be incorporated by the construction of a fairly simple periodic potential. In doing so we shall ignore the effects of the inelastically scattered events. Although they are less frequent than elastic events, their most important effects are a loss of flux, due scattering of electrons out of the microscope aperture, and also to redistribute electrons among the Bragg beams, and into a diffuse background between beams. This redistribution, for which it is difficult to establish a good model, distorts the useful information carried by the Bragg diffracted electrons, and thus puts an effective limit on the accuracy which can be expected from quantitative electron crystallography. We shall return to inelastic scattering towards the end of this section.

Let us first construct the basic periodic potential responsible for Bragg diffraction. the treatment and notation will follow that of Bird (1989). It will be assumed that the crystal is perfectly periodic, rigid and static. It is found in practice that the electrons involved in bonding are almost undetectable in HEED experiments (but see Zuo, Spence and O'Keeffe 1988), so an accurate static potential can be constructed from a sum of the neutral atom potentials:

$$V(\mathbf{r}) = \sum_{\mathbf{l}} \sum_{\kappa} v_{\kappa}^{o}(\mathbf{r} - \mathbf{l} - \mathbf{r}_{\kappa}). \qquad (2.1.1)$$

Here the $\mathbf{l}$ are the lattice vectors, and $\mathbf{r}_{\kappa}$ is the position of the $\kappa^{th}$ atom in the unit cell. The potentials $v_{\kappa}^{o}(\mathbf{r})$ may be obtained from the electronic and nuclear charge densities of the individual atoms by solving Poisson's equation (Ashcroft

and Mermin 1976). The potential $V$ is written as the Fourier series

$$V(\mathbf{r}) = \sum_{\mathbf{g}} V_{\mathbf{g}} \exp(i\mathbf{g} \cdot \mathbf{r}) \tag{2.1.2}$$

with

$$V_{\mathbf{g}} = \frac{1}{\Omega_c} \int_{\Omega_c} V(\mathbf{r}) \exp(-i\mathbf{g} \cdot \mathbf{r})\, d^3\mathbf{r}, \tag{2.1.3}$$

where the g are the reciprocal lattice vectors and $\Omega_c$ is the volume of the unit cell. Note that $|\mathbf{g}| = \frac{2\pi}{d}$ where $d$ is the lattice spacing. From (2.1.1), (2.1.2) and (2.1.3) it is found that

$$V_{\mathbf{g}} = \sum_{\kappa} v_{\kappa}^{0}(\mathbf{g}) \exp(-i\mathbf{g} \cdot \mathbf{r}_{\kappa}), \tag{2.1.4}$$

where the atomic form factors $v_{\kappa}^{0}(\mathbf{g})$ are essentially the Fourier transform of the atomic potentials $v_{\kappa}^{0}(\mathbf{r})$

$$v_{\kappa}^{0}(\mathbf{g}) = \frac{1}{\Omega_c} \int_{\Omega_c} v_{\kappa}^{0}(\mathbf{r}) \exp(-i\mathbf{g} \cdot \mathbf{r}) d^3\mathbf{r},$$

and are, apart from a few scaling factors, the quantities tabulated by Doyle and Turner (1968), Smith and Burge (1962) and others. Most HEED calculations use these tabulated atomic form factors as the basis of a scattering potential. The $V_{\mathbf{g}}$ are then typically of order a few electron volt or less in magnitude (Metherell 1976).

Let us assume that the mean equilibrium position of each ion is the same as for the static lattice, and that the deviation of the atom $\kappa$ at lattice site $\mathbf{l}$ is $\mathbf{u}_{l\kappa}(t)$ and is small compared with interionic spacings. We may then work within the harmonic approximation (Ashcroft and Mermin 1976) to produce a simple analytical correction to the atomic form factors.The Bragg beams will then arise from a thermally averaged potential and the deviations will go into a thermal

diffuse scattering background. With this additional displacement included, the incident electrons will effectively see a thermally averaged elastic potential

$$V_{\mathbf{g}} = \sum_{\kappa} v_{\kappa}^{0}(\mathbf{g}) \exp(-i\mathbf{g} \cdot \mathbf{r}_{\kappa}) \langle \exp(-i\mathbf{g} \cdot \mathbf{u}_{l\kappa}) \rangle. \tag{2.1.5}$$

If it is further assumed that the ionic vibrations are isotropic about the equilibrium positions, then the thermal averaging term $\langle\rangle$ may be written as (eg Dederichs 1972)

$$\langle \exp(-i\mathbf{g} \cdot \mathbf{u}_{l\kappa}) \rangle = \exp(-M_{\kappa} g^2), \tag{2.1.6}$$

which is the Debye-Waller factor. In the notation used here, $M_{\kappa} = \frac{1}{2}\langle u_{l\kappa}^2 \rangle$. Effective form factors may be written as

$$v_{\kappa}(\mathbf{g}) = v_{\kappa}^{0}(\mathbf{g}) \exp(-M_{\kappa} g^2) \tag{2.1.7}$$

and these can be used in an elastic scattering potential which takes into account the average thermal motion of the ions. It should be noted that the $v_{\kappa}^{o}(\mathbf{g})$ are themselves rapidly decreasing functions of $\mathbf{g}$, ($\propto g^{-2}$ at large $g$, see Doyle and Turner 1968), so that the structure factors $V_{\mathbf{g}}$ are strongest for the shortest reciprocal lattice vectors, and diffraction through large angles is much weaker than through shallow angles.

We now suppose that the perfect crystal is subject to a strain field which causes a deformation of the atomic arrangement. Let an atom $i$ which would be at position $\mathbf{r}_i$ in the perfect crystal be displaced by $\Delta\mathbf{r}_i$, to the position $\mathbf{r}_i + \Delta\mathbf{r}_i$ in the deformed crystal. The displacement is assumed to be a function of both the particular strain field and the position in the crystal, $\Delta\mathbf{r} = \Delta\mathbf{r}(\mathbf{r})$. Because of the change of position the deformation will also cause a change in the potential. The deformable ion approximation (Howie and Basinski 1968; Humpreys 1979)

assumes the potential deforms smoothly, so that the potential at the point $\mathbf{r}$ in the deformed crystal is the same as that of the perfect crystal at $\mathbf{r} - \Delta\mathbf{r}$. The potential in a deformed crystal may then be written

$$V(\mathbf{r}) = \sum_{\mathbf{g}} V_{\mathbf{g}} \exp(i\mathbf{g} \cdot (\mathbf{r} - \Delta\mathbf{r})). \tag{2.1.8}$$

Thus although $V$ is still constructed from Fourier coeffients it may now, because of the deformation, be no longer periodic, $V(\mathbf{r}) \neq V(\mathbf{r} + \mathbf{l})$. Comparing (2.1.2) and (2.1.8) the potential of the deformed crystal may be represented by the perfect crystal potential in which the structure factors have gained an extra phase such that

$$V_{\mathbf{g}} \rightarrow V_{\mathbf{g}} \exp(-i\mathbf{g} \cdot \Delta\mathbf{r}). \tag{2.1.9}$$

The deformable ion approximation ignores changes in the unit cell, caused by the deformation, and will only be valid if the displacement $\Delta\mathbf{r}$ does not change significantly in a lattice distance. It also does not take into account the changes in the electron distribution. However provided that the displacement, due to a strain field, is small and slowly varying, the deformable ion approximation should be both a valid and useful approximation.

So far then, we have considered the elastic process. These have been described using a real potential $V(\mathbf{r})$, which contributes to an hermitian Hamiltonian. As discussed in the next section this leads to flux conserving solutions of the diffraction equations. Inelastic processes may cause flux to be lost from the Bragg beams (and the experiment as a whole if electrons are scattered out of the microscope apertures). For fast electrons the 3 main processes for absorption are inelastic scattering by single electron excitation, plasmons and phonons. As

in optics these effects may be described using an imaginary part of the crystal potential $iV'(\mathbf{r})$ (Yoshioka 1957), which renders the Hamiltonian non-hermitian, and hence leads to a loss of of flux. Because of this loss, $iV(\mathbf{r})$ is usually refered to as an absorptive potential, even though no electrons may have physically been absorbed by the crystal. Because the imaginary part of the potential is associated with the crystal lattice we again expand the potential as a Fourier series based on the crystal lattice. Absorption may then be taken into account in HEED by modifying the potential in sections 2.1 to 2.4, so that

$$\begin{aligned} V(\mathbf{r}) &\rightarrow V(\mathbf{r}) + iV'(\mathbf{r}) \\ V_{\mathbf{g}} &\rightarrow V_{\mathbf{g}} + iV'_{\mathbf{g}} \\ U_{\mathbf{g}} &\rightarrow U_{\mathbf{g}} + iU'_{\mathbf{g}}. \end{aligned} \tag{2.1.10}$$

Unfortunately, most of the absorptive contributions to the optical potential are extremely difficult to calculate (Dedrichs 1972), because they tend to be non-local and cannot in general be contructed from individual atomic contributions. Instead they must be found, for example, by first principle calculations of the electronic structure or the phonon spectrum of a particular material. See for example Howie (1963) for a discussion of plasmon scattering, Rez (1970) for a discussion of single electron excitation and Rez *et al* (1977) for a discussion of phonon scattering. It has become established practice where high precision accuracy is not required to assuume that the imaginary part of the potential is equal to a multiple of the real part of the potential (Hasimoto, Howie and Whelan 1962; Humphreys 1979).

Here in this thesis because of the complexity in including absorption, we shall only concern ourselves with 2-beam case. We will also make the assumption

that the absorptive potential may taken to be a multiple of the real potential. Absorption will thus place a limit on the accuracy obtainable. This will provide a useful qualitative picture of the effects of absorption in the simple 2-beam case, but will not provide any valid quantitative information.

## 2.2 FORWARD SCATTERING APPROXIMATION.

The dynamical theory, which will be used to find the scattered intensity, is a wave mechanical treatment, where the crystal is treated as a periodic potential. The incident electron wavefunction is scattered from the potential field as a whole rather than from individual atoms. For electrons having energies which lie in the non relativistic range, the electron wavefunction can be found by solving the Schrödinger equation. As the electrons in HEED have energies greater than 100 keV, and therefore velocities greater than 55% of the speed of light, they are highly relativistic. However it has been shown (Fujiwara 1961, 1962) that the nonrelativistic Schrödinger equation can be used with sufficient accuracy provided the relativistic electron wavevector, $\mathbf{k}$, and mass, $m$, are used. The electron wavefunction $\Psi$ at the point $\mathbf{r}$ may then found by solving the effective Schrödinger (or Fujiwara) equation

$$\left(-\nabla_{\mathbf{r}}^2 + U(\mathbf{r})\right)\Psi(\mathbf{r}) = \mathbf{k}^2\Psi(\mathbf{r}). \tag{2.2.1}$$

Here $\mathbf{k}^2$ is an effective energy given by $\mathbf{k}^2 = m_0 c\sqrt{\gamma^2 - 1}/\hbar$; $\gamma = 1 + ev/m_0c^2$ in which $v$ is the accelerating voltage (Bird 1989), and $U(\mathbf{r})$ is the effective potential at $\mathbf{r}$ and is given by

$$U(\mathbf{r}) = \frac{2m}{\hbar^2}V(\mathbf{r}), \tag{2.2.2}$$

where $V(\mathbf{r})$ is the crystal potential (discussed in the last section). Although we have called $\mathbf{k}^2$ the effective energy and $U$ an effective potential, their units are in fact $\text{Å}^{-2}$. With $V(\mathbf{r})$ of order an electron Volt, the $U(\mathbf{r})$ are of order 1 $\text{Å}^{-2}$.

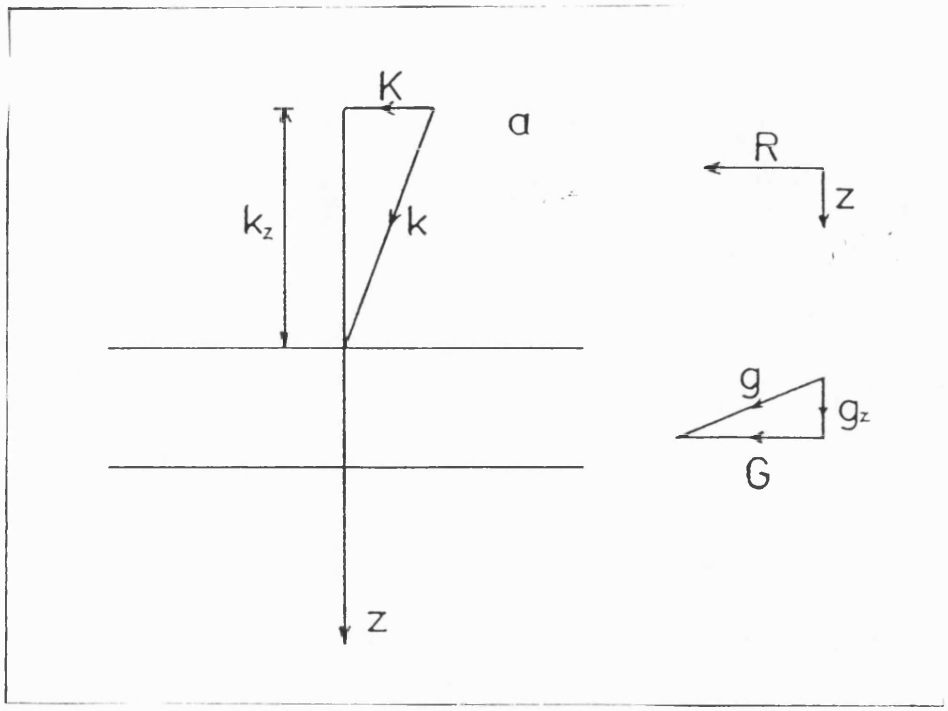


Figure 2.1 Schematic of the HEED geometry considered in this thesis. Note that $z$ is always taken as the zone axis direction. Upper case letters indicate 2-dimensional vectors perpendicular to this $z$-direction.

Figure 2.1 shows a simple schematic of the geometry and nomenclature that will be used throughout the thesis. In the general case, the incident electron beam is directed along or close by a zone axis. The angle between the zone axis and the surface normal does not have a significant effect on the diffracted beam pattern, provided it is small (see for example Bird 1989). The zone axis is defined to be in the $z$ direction, and a point in $x-y$ plane, which is perpendicular to the zone axis, by the vector $\mathbf{R}$. It is assumed that the specimen is an infinite parallel

sided crystal with surfaces lying in the $z = 0$ and $z = t$ planes.

The effects of surface relaxation and twisting will be ignored in this thesis. Although in ignoring them we may be making a bad approximation, we are forced to do so due to the difficulty of including them. For a perfect crystal this is probably an acceptable approximation, as they are expected to have little influence on experimental micrographs (Bird 1989). However for a deformed crystal both surface relaxation and twisting can significantly alter an electron micrograph. For a deformed crystal they may change the *details* but probably not the basic struture.

All 3-dimensional vectors may then be written in terms of their transverse $\mathbf{R}$ and longitudinal $z$ parts. For example the incident electron wavevector becomes $\mathbf{k} = \mathbf{K} + k_z\hat{\mathbf{z}}$. The incident orientation of an electron can therefore be defined by its transverse wavevector $\mathbf{K}$. The quantity which we would like to calculate is the intensity of the diffracted electron beams at the exit surface of the crystal as a function of orientation; ie $I(\mathbf{K}, t)$ for as many diffracted beams as is considered necessary and for deformed crystals as a function of position.

The range of angles between the zone axis and the incident electron wavevector is small, of order a few degrees or less. Because of this small angle of incidence the magnitudes of $\mathbf{k}$ and $k_z$ are almost the same, whilst that of $\mathbf{K}$ is much smaller. For a 200 keV incident electron, $k \simeq k_z \sim 250\text{Å}^{-1}$, but $K \sim 1\text{Å}^{-1}$. The effective energy $k^2$ is much larger than the effective potential $U$, which decreases rapidly at large angles due to the rapid fall off of the atomic form factors (discussed in section 2.1). It is thus expected, and confirmed experimentally, that the electron wavefunction will only be scattered through small angles, and

the large differences between the transverse and longitudinal parts of the electron wavevector will remain inside the crystal. The significance of this is that the scattering will be predominantly forward directed and the rapid variation of $\Psi$ with $z$ may be factored out by writing (Bird 1989)

$$\Psi(\mathbf{r}) = \psi(\mathbf{R}, z)\exp(ikz), \tag{2.2.3}$$

where $\psi(\mathbf{R}, z)$ is a slowly varying function in $\mathbf{R}$ and $z$. Upon making the substitution for $\Psi$, (2.2.3), the Fujiwara equation (2.2.1) becomes

$$\Big(-\nabla^2_{\mathbf{R}} + U(\mathbf{r})\Big)\psi(\mathbf{R}, z) = 2ik\frac{\partial\psi}{\partial z} + \frac{\partial^2\psi}{\partial z^2}. \tag{2.2.4}$$

Having factored out the rapid variation in the $z$ direction, it is expected that the second derivative in $z$ is small in comparison with the first and may be neglected with little loss of accuracy. For a plane wave solution, $\frac{\partial\psi}{\partial z} \sim \frac{K^2}{k}\psi$, and the second derivative is then $\sim (\frac{K}{k})^2$ smaller than the first term. The relevant equation governing HEED is then

$$\Big(-\nabla^2_{\mathbf{R}} + U(\mathbf{r})\Big)\psi(\mathbf{R}, z) = 2ik\frac{\partial\psi}{\partial z}. \tag{2.2.5}$$

In (2.2.5) the Laplacian operator $\nabla$ is only with respect to $\mathbf{R}$, but the effective potential is still $U = U(\mathbf{R}, z)$. By dropping the second derivative an error has been introduced. The free space wavefunction, given by (2.2.3) with $\psi(\mathbf{R}, z)$ found by solving (2.2.5) for $U = 0$, is

$$\Psi(\mathbf{r}) = \exp(i\mathbf{K}\cdot\mathbf{R})\exp(i\{k - K^2/2k\}z),$$

but the true free space wavefunction is

$$\Psi(\mathbf{r}) = \exp(i\mathbf{K}\cdot\mathbf{R})\exp(ik_z z),$$

with $k_z = (k^2 - K^2)^{1/2}$. Thus by ignoring the second derivative an approximation in $k_z$ has been made. The free space sphere $k_z = (k^2 - K^2)^{1/2}$ has been replaced by the parabola $k_z = k - K^2/2k$. For HEED this difference will be small as $k \gg K$.

Thus this approximation has transformed the Fujiwara equation (2.2.1) into an equation identical in form to the low energy time dependent Schrödinger equation in 2-dimensions,

$$\left(\frac{-\hbar^2}{2m_0}\nabla^2_{\mathbf{R}} + V(\mathbf{R},t)\right)\psi(\mathbf{R},t) = i\hbar\frac{\partial\psi}{\partial t},$$

where $z$, the depth of an electron in the crystal, effectively represents time and Planck's constant, $\hbar$, becomes $m_0/k$ (and is through $k$ a variable). The propagation of the electron wavefunction through the crystal is then equivalent to the time evolution of the electron wavefunction through a 2-dimensional potential space $V(\mathbf{R},t)$. It is thus possible to apply many of the standard techniques of low energy quantum mechanics to the analysis of HEED and is why high energy electrons exhibit many of the characteristics of low energy quantum mechanics. One of these, Berry's geometric phase (Berry 1984), will be looked at in the next chapter.

## 2.3 THE PROJECTION APPROXIMATION.

As already mentioned the electrons are incident near a zone axis. Such an axis describes a direction in the crystal which is perpendicular to a set of reciprocal lattice layers (Hirsch *et al* 1977). In this case, as shown in figure 2.2, all of the reciprocal lattice vectors lie in 2-dimensional layers perpendicular to the zone axis direction $[uvw]$. Here again there is a natural separation of 3-dimensional

vectors into transverse ($\mathbf{R}$) and longitudinal ($z$) components. A general reciprocal lattice vector which lies in the $n^{th}$ layer may be written as $\mathbf{g}^{(n)} = (\mathbf{G}, ng_z)$. Thus a zeroth layer reciprocal lattice vector is written as $\mathbf{G}[hkl]$ and obeys the rule $uh+vk+lw = 0$; that is, any zeroth layer reciprocal lattice vector is perpendicular to the zone axis direction. All other higher layers ($n > 0$) are identical to the zeroth layer (apart from a possible offset) but equally spaced by $g_z$ in the zone axis direction.

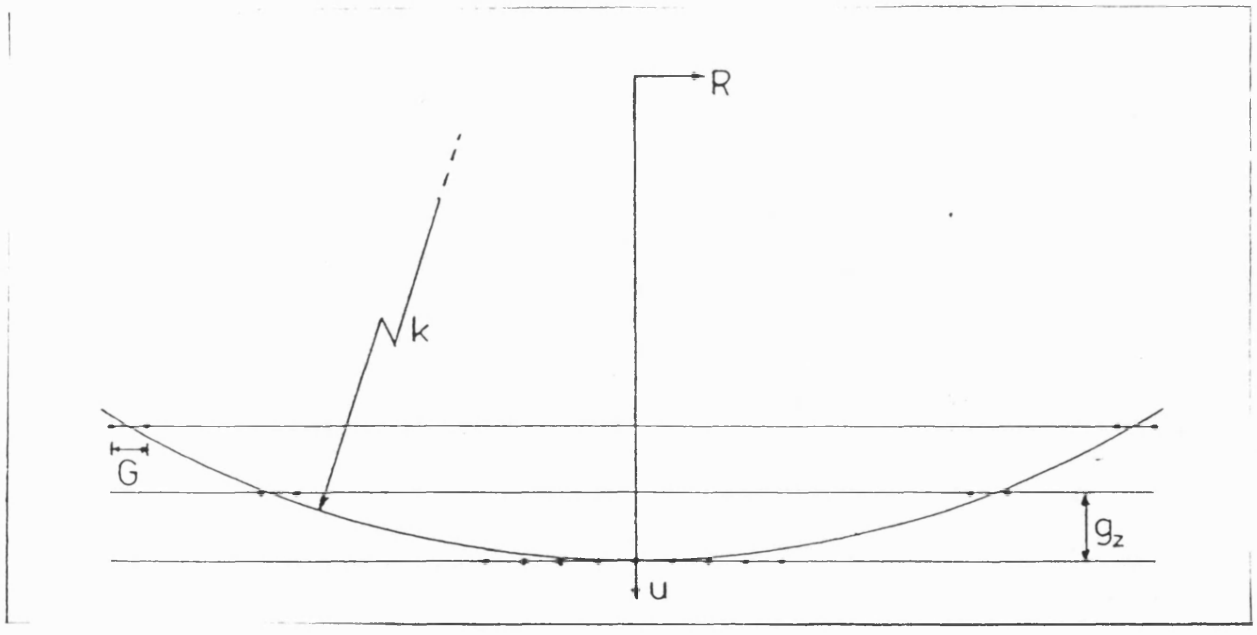


Figure 2.2 The separation of the reciprocal lattice into layers perpendicular to the zone axis. The strongest diffraction is observed in the central, zero-layer region.

The potential $V(\mathbf{r})$ may then be separated into its longitudinal and transverse components (Bird 1989),

$$V(\mathbf{r}) = \sum_n V^{(n)}(\mathbf{R}) \exp(ing_z z), \tag{2.3.1}$$

where

$$V^{(n)}(\mathbf{R}) = \frac{1}{d}\int_0^d V(\mathbf{R})\exp(-ing_z z)dz. \tag{2.3.2}$$

Here $d$, equal to $2\pi/g_z$, is the zone axis repeat distance.

In the projection approximation (Humphreys 1979) it is assumed that for a perfect crystal only reciprocal lattice vectors lying in the zeroth layer of the Ewald sphere produce significant diffraction and all higher order effects may be ignored. Thus at most only a plane of $\mathbf{G}'s$ contribute, though this may in practice become a 1 dimensional line or even just 2 points. The potential $V$ for a perfect crystal is then 2-dimensional, depending only on $\mathbf{R}$ and the equation governing HEED is then

$$\left(-\nabla^2_{\mathbf{R}} + U(\mathbf{R})\right)\psi(\mathbf{R}, z) = 2ik\frac{\partial\psi}{\partial z}, \tag{2.3.3}$$

where $U$ is found from (2.2.2) and (2.3.1) with $n = 0$,

$$U(\mathbf{R}) = \frac{2m}{\hbar^2}\sum_{\mathbf{G}} V_{\mathbf{G}}\exp(i\mathbf{G}\cdot\mathbf{R}). \tag{2.3.4}$$

Here $V^{(0)}_{\mathbf{G}}$ is given from (2.1.5).

In the case of a deformed crystal it is assumed that the above argument still holds, but that the potential Fourier components have altered (as previously discussed in section 2.1) by gaining a phase factor. The effective potential for a deformed crystal is then the same as that of the perfect crystal apart from a shift of origin and is given by

$$\begin{aligned} U(\mathbf{r}) &= \frac{2m}{\hbar^2}\sum_{\mathbf{G}} V_{\mathbf{G}}\exp(i\mathbf{G}\cdot\{\mathbf{R}-\Delta\mathbf{r}\}) \\ &= \sum_{\mathbf{G}} U_{\mathbf{G}}\exp(i\mathbf{G}\cdot\{\mathbf{R}-\Delta\mathbf{r}\}). \end{aligned} \tag{2.3.5}$$

In (2.3.4) there is no $z$ dependence and the effective potential varies only with $\mathbf{R}$. Conversely in (2.3.5) the deformation causes the effective potential to become $z$ dependent again, though in the projection approximation the effective potential is assumed to be only slowly varying with depth.

Thus in the case of a deformed crystal the equation governing HEED becomes

$$\left(-\nabla^2_{\mathbf{R}} + U(\mathbf{R}, z)\right)\psi(\mathbf{R}, z) = 2ik\frac{\partial \psi}{\partial z}, \tag{2.3.6}$$

where the effective potential is given by (2.3.5).

It should be noted that if the displacement, $\Delta\mathbf{r}$, is perpendicular to $\mathbf{G}$, ie it has no transverse component, then $\mathbf{G} \cdot \Delta\mathbf{r} = 0$. The perfect crystal potential will then be recovered and any effects of the deformation will not be seen in a diffraction pattern. Thus only the transverse component of the displacement need be considered. From here onwards, unless stated otherwise, we shall only consider the displacement in the transverse direction $\Delta\mathbf{R}$. Hence effects from the displacement of atoms in the $z$ direction, due to a strain field, will not be seen in an electron micrograph. This invisible defect criteria may allow important information about the strain field to be recovered (see for example Humphreys 1979). This does not mean that depth information about the strain field cannot be recovered. The transverse displacement may still vary with depth, $\Delta\mathbf{R}(z)$, and so carry depth information about the strain field. Two such examples are discussed in chapter 4. This also raises the question of uniqueness. Different strain fields with the same transverse displacement, $\mathbf{R}$, may give rise to the same images and thus are not unique. An example of this is discussed in chapter 4, where we look at the effect that tilting a dislocation has upon an electron micrograph. Although a single electron micrograph will not allow a

strain field to be uniquely determined, if 3 electron micrographs are taken from different non-coplanar directions, then a strain field may in principle be uniquely identified (Humphreys 1979).

In the projection approximation the effect of the deformation is to change the dimensionality of the Hamiltonian. In the case of a perfect crystal the Hamiltonian is 2-dimensional depending only upon $\mathbf{R}$, whilst for a deformed crystal the Hamiltonian becomes 3-dimensional through the effective potential $U(\mathbf{r})$. An electron travelling through a perfect crystal sees a potential in which each layer in the $x-y$ plane has the same 2-dimensional form. In the case of a deformed crystal the electron sees a potential which varies with depth. The deformation changes the effective Schrödinger equation from a time independent to a time dependent problem.

## 2.4 THE COLUMN APPROXIMATION.

In the case of a perfect crystal, the Hamiltonian in (2.3.3) depends only upon $\mathbf{R}$ and the Schrödinger equation may be solved to the required accuracy. This may be done by seperating out the $\mathbf{R}$ and $z$ dependence and transforming the problem to be solved into a 2-dimensional partial differential equation and an ordinary differential equation, which may then be solved computationally (eg Bird 1989). However the introduction of a deformation causes the Hamiltonian, through the potential $U(\mathbf{R}, z)$, (2.1.8), to become both $\mathbf{R}$ and $z$ dependent. Now the problem to be solved is a 3-dimensional coupled partial differential equation. This is particularly difficult to solve analytically and although computer programs exist to solve such equations, it may well prove very expensive in computer time. In order to render the problem more managable, both ana-

lytically and computationally, the column approximation is normally made at this stage (Hirsch *et al* 1977).

To analyse the column approximation we here follow the procedure used by Howie and Basinski (1968). We write the wavefunction $\psi(\mathbf{K},\mathbf{r})$ as a plane wave expansion,

$$\psi(\mathbf{K},\mathbf{r}) = \sum_{\mathbf{G}} \psi_{\mathbf{G}}(\mathbf{K},\mathbf{r}) \exp(i\{\mathbf{K}+\mathbf{G}\}\cdot\mathbf{R}). \tag{2.4.1}$$

Upon making the substitutions for the wavefunction and the potential, (2.4.1) and (2.3.5), the Schrödinger equation (2.3.6) becomes

$$\sum_{\mathbf{G}}\Bigg((\mathbf{K}+\mathbf{G})^2\psi_{\mathbf{G}} - 2i(\mathbf{K}+\mathbf{G})\cdot\nabla_{\mathbf{R}}\psi_{\mathbf{G}} - \nabla^2_{\mathbf{R}}\psi_{\mathbf{G}} - 2ik\frac{\partial\psi_{\mathbf{G}}}{\partial z} + \sum_{\mathbf{G}'} U_{\mathbf{G}-\mathbf{G}'}\psi_{\mathbf{G}'}\exp(-i\{\mathbf{G}-\mathbf{G}'\}\cdot\Delta\mathbf{R})\Bigg)\exp(i\{\mathbf{K}+\mathbf{G}\}\cdot\mathbf{R}) = 0. \tag{2.4.2}$$

For a perfect crystal, where $\Delta\mathbf{r} = 0$, the coefficients of the wavefunction are independent of position; ie $\psi_{\mathbf{G}}$ does not depend upon $\mathbf{r}$. Thus the coefficients of the exponential in (2.4.2) (the terms in [ ]) are independent of position. Because (2.4.2) holds at all points in the crystal $\mathbf{r}$ and the coefficients of the exponential are independent of $\mathbf{R}$, the equation can be satisfied only if each coefficient is independently equal to zero (Metherell 1976).

Although we may only truly equate the coefficients of the exponential in (2.4.2) to zero for the perfect crystal, the assumption that we may do so for a deformed crystal is justified within the context of the deformable ion approximation. As long as the deformation is on a scale that is much larger than the unit cell, then each Fourier coefficient esentially remains independent of the others. In this case the effective potential changes slowly and so also will the wavefunction $\psi_{\mathbf{G}}$.

The coefficients of the exponential may then be approximated to zero with little error. Having done this the wavefunctions can be found by solving

$$2ik\frac{\partial\psi_{\mathbf{G}}}{\partial z} = \sum_{\mathbf{G}'}\Big((\mathbf{K}+\mathbf{G})^2\delta_{\mathbf{G},\mathbf{G}'} + U_{\mathbf{G}-\mathbf{G}'}\exp(-i\{\mathbf{G}-\mathbf{G}'\}\cdot\Delta\mathbf{R})\Big)\psi_{\mathbf{G}'} - 2i(\mathbf{K}+\mathbf{G})\cdot\nabla_{\mathbf{R}}\psi_{\mathbf{G}} - \nabla^2_{\mathbf{R}}\psi_{\mathbf{G}}. \quad (2.4.3)$$

In the column approximation it is assumed because $k \gg |\mathbf{K}+\mathbf{G}|$ and $\psi_{\mathbf{G}}$ is a slowly varying function, that the last two terms on the right hand side of (2.4.3) may be ignored, giving

$$2ik\frac{\partial\psi_{\mathbf{G}}}{\partial z} = \sum_{\mathbf{G}'}\Big((\mathbf{K}+\mathbf{G})^2\delta_{\mathbf{G},\mathbf{G}'} + U_{\mathbf{G}-\mathbf{G}'}\exp(-i\{\mathbf{G}-\mathbf{G}'\}\cdot\Delta\mathbf{R})\Big)\psi_{\mathbf{G}'}. \quad (2.4.4)$$

It has therefore been assumed that

$$2ik\frac{\partial\psi_{\mathbf{G}}}{\partial z} \gg (\mathbf{K}+\mathbf{G})\cdot\nabla_{\mathbf{R}}\psi_{\mathbf{G}} \quad (2.4.5a)$$

and

$$2ik\frac{\partial\psi_{\mathbf{G}}}{\partial z} \gg \nabla^2_{\mathbf{R}}\psi_{\mathbf{G}}. \quad (2.4.5b)$$

If we define the scale of the deformation to be $L$ and that of the unit cell to be $a$, where $L \gg a$, then the right hand sides of (2.4.5a) and (2.4.5b) are such that

$$(\mathbf{K}+\mathbf{G})\cdot\nabla_{\mathbf{R}}\psi_{\mathbf{G}} \sim \frac{1}{a}\frac{1}{L}\psi_{\mathbf{G}} \quad (2.4.6a)$$

$$\nabla^2_{\mathbf{R}}\psi_{\mathbf{G}} \sim \frac{1}{L^2}\psi_{\mathbf{G}}. \quad (2.4.6b)$$

Clearly as $L \gg a$, if (2.4.5a) is satisfied then (2.4.5b) will also be satisfied. The slowest variation of $\psi$ will be at the Bragg condition. There $\partial\psi_{\mathbf{G}}/\partial z \sim \psi_{\mathbf{G}}/\xi$ (Howie and Basinski 1968; Hirsch *et al* 1977), where $\xi$ the extinction distance is the periodicity with depth of the amplitude oscillations. Hence from (2.4.5a)

and (2.4.6a), and using $1/a \sim g$, we have that the condition to drop the last two terms in (2.4.3) becomes

$$\frac{1}{\xi} \gg \frac{g/k}{L} = \frac{\theta_B}{L}$$

where $\theta_B$ is the Bragg angle. Now the $\xi$ are typically of order a few hundred Å for a 100 keV incident electron and $\theta_B$ is of order $10^{-2}$ radians (Humphreys 1979), and hence the distance $\xi\theta_B$ is of order a few Å. Thus provided the scale of the deformation $L$ is greater than 10Å we may safely ignore the terms.

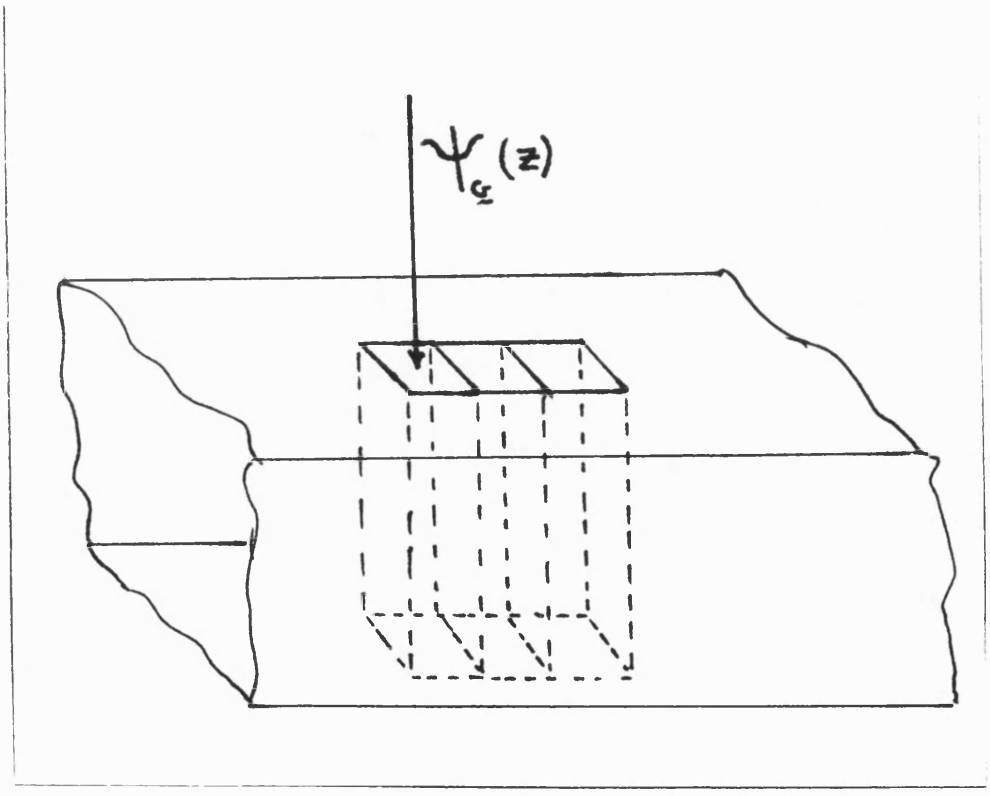


Figure 2.3 In the Column approximation the crystal is imagined to be divided into a number of vertical columns. Within each column the effective potential changes so slowly in the $\mathbf{R}$ plane that the electron wavefunction depends only upon the column it is in and is independent of all other columns.

In effect the column approximation assumes that the wavefunction $\psi_{\mathbf{G}}$ does

not vary greatly in the $x-y$ plane and the crystal may be imagined as being divided into a number of columns, figure 2.3. In each column it is assumed that the electron amplitude at a point inside each particular column arises from the particular column it is in and is independent of all adjacent columns. Then $\mathbf{R}$ is considered to be only a parameter and $z$ considered the only variable. The column approximation has thus reduced the 3-dimensional coupled partial differential problem into a 1-dimensional partial differential coupled problem, (2.4.4), to be solved for each column $\mathbf{R}$ in the $x-y$ plane.

## 2.5 THE TWO BEAM CASE.

We now turn to the most simple case, in which only one diffracted wave is of significance. In the two beam approximation only two waves are considered, the undiffracted wave and one diffracted wave, which correspond to reciprocal lattice vectors $\mathbf{0}$ and $\mathbf{G}$. This approximation is expected to be good when one diffracted beam is much stronger than all of the others and may occur when the crystal has large reciprocal lattice vectors and is composed of light atoms (Humphreys 1979). The two beam case has a number of advantages. It is both simple and allows a valuable insight into the many beam dynamical theory, showing a number of important details and effects.

From (2.4.4) the amplitudes of the undiffracted and the diffracted waves may be found by solving

$$\begin{pmatrix} K^2+U_{\mathbf{0}} & U_{-\mathbf{G}}\exp(i\mathbf{G}\cdot\Delta\mathbf{R}) \\ U_{\mathbf{G}}\exp(-i\mathbf{G}\cdot\Delta\mathbf{R}) & (\mathbf{K}+\mathbf{G})^2+U_{\mathbf{0}} \end{pmatrix} \begin{pmatrix} \psi_{\mathbf{0}} \\ \psi_{\mathbf{G}} \end{pmatrix} = 2ik\frac{d}{dz}\begin{pmatrix} \psi_{\mathbf{0}} \\ \psi_{\mathbf{G}} \end{pmatrix}. \quad (2.5.1)$$

Equations (2.5.1) are one form of the Howie-Whelan equations (Howie and Whelan 1961). They show that in passing through a layer $dz$, both the undiffracted

and the diffracted beam amplitudes will be changed by $d\psi_{\mathbf{0}}$ and $d\psi_{\mathbf{G}}$ respectively. The first term of the first equation represents no scattering, $\mathbf{K} \rightarrow \mathbf{K}$ whilst the second term represents Bragg scattering $\mathbf{K} \rightarrow \mathbf{K} + \mathbf{G}$. The effects of the strain field are felt by off diagonal terms. The term $U_{\mathbf{0}}$ effectively becomes the background potential replacing that of free space.

In order to understand the features of diffraction patterns it is necessary to consider the case of a crystal which is not oriented at the exact Bragg angle. Normally away from the Bragg condition no diffraction is expected, however for thin crystals this rigorous condition may be relaxed, resulting in significant diffraction. This may be represented on the Ewald sphere by extending the reciprocal lattice points in a direction normal to the plane of the specimen (Goodhews and Humphreys 1976). Let $\delta\mathbf{K}$, the small deviation away from the Bragg condition at which significant diffraction still occurs, be defined by

$$\delta\mathbf{K} = \mathbf{K} + \frac{\mathbf{G}}{2}.$$

Hence we define the deviation parameter, $W$, to be

$$W = \delta\mathbf{K} \cdot \mathbf{G} = \mathbf{K} \cdot \mathbf{G} + \frac{G^2}{2} \tag{2.5.2}$$

(Bird and Preston 1988). Using (2.5.2) and making the substitutions

$$\begin{aligned} \psi_{\mathbf{0}} &= \tilde{\psi}_{\mathbf{0}} \exp(-i\{K^2 + U_{\mathbf{0}} + W\}z/2k) \\ \psi_{\mathbf{G}} &= \tilde{\psi}_{\mathbf{G}} \exp(-i\{K^2 + U_{\mathbf{0}} + W\}z/2k) \end{aligned}, \tag{2.5.3}$$

(2.5.1) may be written

$$\begin{pmatrix} W & \tilde{U}\exp(i\mathbf{G}\cdot\Delta\mathbf{R}) \\ \tilde{U}\exp(-i\mathbf{G}\cdot\Delta\mathbf{R}) & -W \end{pmatrix} \begin{pmatrix} \tilde{\psi}_{\mathbf{0}} \\ \tilde{\psi}_{\mathbf{G}} \end{pmatrix} = -2ik\frac{d}{dz}\begin{pmatrix} \tilde{\psi}_{\mathbf{0}} \\ \tilde{\psi}_{\mathbf{G}} \end{pmatrix}. \tag{2.5.4}$$

Here it has been assumed that the crystal is centrosymmetric and thus $U_{\mathbf{G}} = U_{-\mathbf{G}}$, which has been denoted by $-\tilde{U}$ ($-$ve because the potential is attractive).

Note that the substitutions, (2.5.3), involve a change of phase and thus do not change the intensites of the two beams. The effect of the potential term $U_0$ can thus be seen to be a phase factor. This change in phase is due to refraction, in which the incident wavevector in the $z$ direction, $k_z$, becomes $k_z + U_0/2k$ in the crystal (Hirsch *et al* 1977).

The solution of (2.5.4), another form of the Howie-Whelan equations (Bird and Preston 1988), gives a means of finding the intensities of the undiffracted and diffracted beams. The equations are completely general as no mention has been made of either the nature of the strain field, other than it is slowly varying, or the potential, other than it is centrosymmetric and may be described by the deformable ion approximation. Equations (2.5.4) are the fundamental result of this chapter. They will be used later in chapter 4 to form theoretical electron micrographs of LACBED images.

### 2.5.1 2-beam solution to the perfect crystal.

In order to analyse the solutions to the 2-beam Howie-Whelan equations, let us first look at the analytic solution for a perfect crystal where $\Delta\mathbf{r} = 0$. The perfect crystal is chosen because then (2.5.4) may be solved exactly using analytical methods. For a crystal with a general deformation, equation (2.5.4) can not be solved exactly by analytical means, rather the solutions must be approximated, as will be done in chapter 4. From (2.5.4) we have that

$$\dot{\tilde{\psi}}_{\mathbf{0}} = \frac{W}{U}\tilde{\psi}_{\mathbf{G}} - \frac{2ik}{U}\dot{\tilde{\psi}}_{\mathbf{G}} \qquad (2.5.5a)$$

$$\dot{\tilde{\psi}}_{\mathbf{G}} = -\frac{W}{U}\tilde{\psi}_{\mathbf{0}} - \frac{2ik}{U}\dot{\tilde{\psi}}_{\mathbf{0}}. \qquad (2.5.5b)$$

Equations (2.5.5) togther with the boundary conditions at $z = 0$, $I_{\mathbf{0}} = 1$ and $I_{\mathbf{G}} = 0$, may be solved to give the intensities at depth $z$ as (see for example

Reimer 1984)

$$I_0(z) = \cos^2(\sqrt{W^2+U^2}\frac{z}{2k}) + \frac{W^2}{W^2+U^2}\sin^2(\sqrt{W^2+U^2}\frac{z}{2k}) \quad (2.5.6a)$$

$$I_{\mathbf{G}}(z) = \frac{U^2}{W^2+U^2}\sin^2(\sqrt{W^2+U^2}\frac{z}{2k}). \quad (2.5.6b)$$

For all values of $W$, $\tilde{U}$ and $z$ the total intensity is conserved, $I_0 + I_{\mathbf{G}} = 1$. This arises from our choice of potential, which is perfect and non absorbing. There is then an interchange of intensity between the two beams as they travel through the crystal.

## 2.6 THE GENERAL CASE.

The two beam case is contrived, normally a large number of diffracted beams must be included to obtain the correct diffraction pattern. Thus in order to form a more accurate solution the general case is now considered. Here the number of diffracted beams is not limited and the wavefunctions $\psi_{\mathbf{G}}$ are found, from (2.4.4), by solving the general Howie-Whelan equation

$$2ik\frac{\partial\psi_{\mathbf{G}}}{\partial z} = \sum_{\mathbf{G}'} H_{\mathbf{G}\mathbf{G}'}\psi_{\mathbf{G}'} \quad (2.6.1a)$$

$$= \sum_{\mathbf{G}'}\Big((\mathbf{K}+\mathbf{G})^2\delta_{\mathbf{G},\mathbf{G}'} + U_{\mathbf{G}-\mathbf{G}'}\exp(-i\{\mathbf{G}-\mathbf{G}'\}\cdot\Delta\mathbf{R})\Big)\psi_{\mathbf{G}'}, \quad (2.6.1b)$$

where in the column approximation $\Delta\mathbf{R} = \Delta\mathbf{R}(\mathbf{R}_0, z)$. In (2.6.1) the sum over $\mathbf{G}'$ contains an infinite number of beams. In practise an approximate solution which considers a finite number of beams must be used in actual calculations. The equations may be solved to any degree of accuracy required by choosing the appropriate number of beams. For $n$ beams there will be $2n$ complex simultaneous equations to be solved, giving $n$ complex solutions (the undiffracted

beam, $\mathbf{G} = 0$, and $n-1$ diffracted beams). All of the analysis from the 2-beam case may be carried over and so in (2.6.1) the effects of the strain are again felt through the off-diagonal terms, etc ... .

Equations (2.6.1) are the second fundamental result of this chapter and are again completely general, no mention being made of either the strain field, other than it is slowly varying, or the potential, which does not have to be symmetric. They will be used later in chapter 5 to form theoretical micrographs in both STEM and HREM imaging.

### 2.6.1 General solution for the perfect crystal.

In this section we shall investigate the form of the solution to the general n beam HEED equations for a perfect crystal. Solutions for the perfect crystal will again be used later to form the basis for understanding distorted crystals.

The solution to (2.6.1) for a perfect crystal, in which the Hamiltonian $H_{\mathbf{GG'}}$ is no longer dependent upon $z$, is a standard result in electron diffraction (Humphreys 1979; Bird 1989) and is given by

$$\psi_{\mathbf{G}}(\mathbf{K},\mathbf{r}) = \sum_j \epsilon^j(\mathbf{K}) \exp(-is^j(\mathbf{K})z/2k) C^j_{\mathbf{G}}(\mathbf{K}). \qquad (2.6.2)$$

From (2.4.1) the expression for $\psi$, the solution to (2.3.3) for a perfect crystal, is then given by

$$\psi(\mathbf{K},\mathbf{r}) = \sum_j \epsilon^j(\mathbf{K}) \exp(-is^j(\mathbf{K})z/2k) \sum_{\mathbf{G}} C^j_{\mathbf{G}}(\mathbf{K}) \exp(i\{\mathbf{K}+\mathbf{G}\}\cdot\mathbf{R}), \quad (2.6.3)$$

Here the sum over $\mathbf{G}$ has the periodicity of the 2-dimensional potential and hence of the lattice. It is conventional to call the sum over $\mathbf{G}$ a 2-dimensional Bloch state with respective transverse energy $s^j$ (its units are the same as the effective energy $\text{Å}^{-2}$).

These sets of equations indicate that an electron with incident wavevector $k_z$ is split by the crystal potential into a number of Bragg waves, each having different longitudinal wavevectors $k_z^j \simeq k$. From (2.2.3) the longitudinal wavevector of each Bloch wave $j$ inside the crystal is $k_z^j = k - s^j/2k$ (Bird 1989). Because the Bloch waves have different longitudinal wavevectors they have different kinetic energies, and because we are not considering absorption, different potential energies. Physically this is due to different localisation of the Bloch waves within the crystal, $\psi(\mathbf{r})$ (Humphreys 1979).

Although we have the form of the solution to the HEED equations, we still need to be able to find the parameters $C_{\mathbf{G}}^j$, $s^j$ and $\epsilon^j$. The first two terms, $C_{\mathbf{G}}^j$ and $s^j$ can be found by using suitable computer programs to solve (2.6.1), where (2.6.2) has been substituted for $\psi_{\mathbf{G}}$. $\epsilon^j$ may be found from the boundary conditions. These are the standard quantum mechanical boundary conditions for a continuity at an interface, that is both $\psi$ and $\nabla_{\mathbf{r}}\psi$ must be continuous. In effect $\epsilon^j$ is determined by the orientation of the incident beam with respect to the crystal surface (Metherell 1976).

## 2.7 MODIFIED BLOCH WAVE THEORY.

We now apply a transformation to the HEED equations (2.6.1), which produces the so called modified Bloch wave theory, (Wilkens *et al* 1967; Hirsch *et al* 1977; Bird and Preston 1988). First a general transformation is derived and then a particular transformation used within the theory to transform the n-beam equation, (2.6.1), into the standard modified form which allows better approximation schemes to be found.

Let the wavefunction be transformed such that

$$\psi_{\mathbf{G}} = T_{\mathbf{GS}}\ \tilde{\psi}_{\mathbf{S}} \tag{2.7.1}$$

where $T_{\mathbf{GS}}$, a unitary transformation, is to be defined. Applying (2.7.1) to (2.6.1a) gives

$$\sum_{\mathbf{G}'} H_{\mathbf{GG}'}\ T_{\mathbf{G}'\mathbf{S}}\ \tilde{\psi}_{\mathbf{S}} = 2i\dot{T}_{\mathbf{GS}}\ \tilde{\psi}_{\mathbf{S}} + T_{\mathbf{GS}}\ \dot{\tilde{\psi}}_{\mathbf{S}}, \tag{2.7.2}$$

where $H_{\mathbf{GG}'}$ is given through (2.6.1b) and the derivative is with respect to $z$. If we now apply the inverse transformation by multiplying (2.7.2) by $T^{\dagger}_{\mathbf{S}'\mathbf{G}}$ and then sum over first $\mathbf{G}$ and after $\mathbf{S}$, (2.7.2) becomes

$$\sum_{\mathbf{SG}}\Big(\sum_{\mathbf{G}'} T^{\dagger}_{\mathbf{S}'\mathbf{G}}\ H_{\mathbf{GG}'}\ T_{\mathbf{G}'\mathbf{S}} - 2ikT^{\dagger}_{\mathbf{S}'\mathbf{G}}\ \dot{T}_{\mathbf{GS}}\Big)\tilde{\psi}_{\mathbf{S}} = 2ik\sum_{\mathbf{GS}} T^{\dagger}_{\mathbf{S}'\mathbf{G}}\ T_{\mathbf{GS}}\ \dot{\tilde{\psi}}_{\mathbf{S}}. \tag{2.7.3}$$

So far the transformation is general and any unitary transformation $T$ may be used. We now choose a particular matrix, which is defined as

$$T_{\mathbf{GS}} = \exp(-i\{\mathbf{K}+\mathbf{S}\}\cdot\Delta\mathbf{R})\ \delta_{\mathbf{GS}}. \tag{2.7.4}$$

With $T$ given by (2.7.4), the transformation (2.7.1) represents a change in phase and will then not affect the intensity expressions. Substituting (2.7.4) into (2.7.3) gives

$$\sum_{\mathbf{SG}}\Big(\sum_{\mathbf{G}'} H_{\mathbf{GG}'}\exp(i\{\mathbf{G}-\mathbf{S}\}\cdot\Delta\mathbf{R})\delta_{\mathbf{S}'\mathbf{G}}\delta_{\mathbf{G}'\mathbf{S}} - 2k(\mathbf{K}+\mathbf{S})\cdot\Delta\dot{\mathbf{R}}\ \delta_{\mathbf{S}'\mathbf{G}}\delta_{\mathbf{GS}}\Big)\tilde{\psi}_{\mathbf{S}} = 2ik\dot{\tilde{\psi}}_{\mathbf{S}'}.$$

Using the delta functions, this becomes

$$\sum_{\mathbf{S}}\Big(H_{\mathbf{S}'\mathbf{S}}\exp(i\{\mathbf{S}'-\mathbf{S}\}\cdot\Delta\mathbf{R}) - 2k(\mathbf{K}+\mathbf{S})\cdot\Delta\dot{\mathbf{R}}\ \delta_{\mathbf{SS}'}\Big)\tilde{\psi}_{\mathbf{S}} = 2ik\dot{\tilde{\psi}}_{\mathbf{S}'}.$$

Substituting (2.6.1) for $H_{\mathbf{GG}'}$ this can be reduced to

$$\sum_{\mathbf{S}}\Big(\{(\mathbf{K}+\mathbf{S})^2 - 2k(\mathbf{K}+\mathbf{S})\cdot\Delta\dot{\mathbf{R}}\}\delta_{\mathbf{SS}'} + U_{\mathbf{S}'-\mathbf{S}}\Big)\tilde{\psi}_{\mathbf{S}} = 2ik\dot{\tilde{\psi}}_{\mathbf{S}'}. \tag{2.7.5}$$

This represents a new Schrödinger equation for the *modified* wavefunctions, where the new modified Hamiltonian is given by the terms in [ ]. Equation (2.7.5) is similar to (2.6.1) in that the terms $(\mathbf{K}+\mathbf{G})^2 + U_0$ again appear in the diagonal elements of the Hamiltonian. In contrast however the effects of the strain field are now felt by the diagonal terms and through the derivative of the displacement. It should be noted that the modified Hamiltonian is real for centrosymmetric crystals. For a perfect crystal, $\Delta\mathbf{R} = 0$, the modified Hamiltonian is the same as the unmodified, (2.6.1).

We may now ask what advantage has the modified transformation allowed. To answer this let us look at the simplified case of a crystal with straight but tilted columns, figure 2.4.

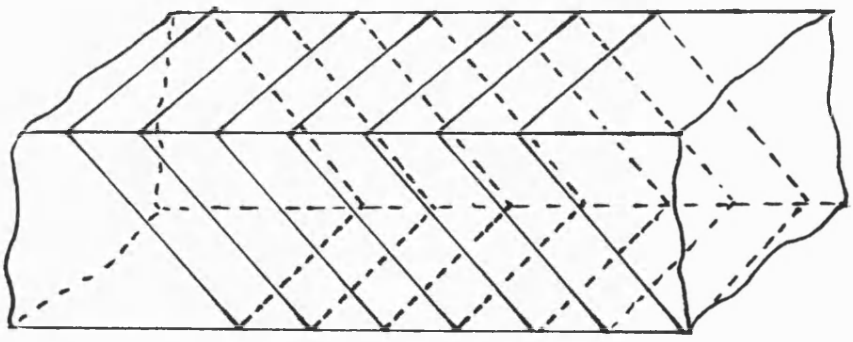

Figure 2.4 Crystal containing parallel tilted columns. The slope of the column is given by $\Delta\dot{\mathbf{R}} = m\hat{\mathbf{R}}$, where $m$ is a constant.

Then the displacement is given by $\Delta\mathbf{R} = (m\hat{\mathbf{R}})z + c$, where $m$ and $c$ are constants. Thus in (2.7.5) $\Delta\dot{\mathbf{R}} = m\hat{\mathbf{R}}$, which is independent of depth $z$ and a constant within each column. Then because, as discussed before in section 2.6.1, the Hamiltonian is independent of depth $z$, we may solve the modified Schrödinger equation exactly by again using a Bloch wave expansion. This is done by proceeding as before in section 2.6.1, by seperating out the wave function into its transverse and longitudinal parts. The solution is then given by

$$\tilde{\psi}(\mathbf{R}) = \sum_{j'} \tilde{\epsilon}^{j'}(\mathbf{K}) \exp(-i\tilde{s}^{j'}(\mathbf{K})z/2k) \sum_{\mathbf{G}} \tilde{C}^{j'}_{\mathbf{G}}(\mathbf{K}) \exp(i\{\mathbf{K}+\mathbf{G}\}\cdot\mathbf{R}). \quad (2.7.6)$$

Similar to the previous section, $\tilde{C}^{j}_{\mathbf{G}}$ and $\tilde{s}^{j}$ are found from equations (2.7.5) and (2.7.6), and $\tilde{\epsilon}^{j}$ from the modified boundary conditions . These boundary conditions are different to those of the previous section, as now we are effectively concerned with the slope of the wavefunction. Using (2.7.1) and (2.7.4) to transform back we find that the original state is given by

$$\psi(\mathbf{R}) = \sum_{j'} \tilde{\epsilon}^{j'}(\mathbf{K}) \exp(-i\tilde{s}^{j'}(\mathbf{K})z/2k) \sum_{\mathbf{G}} \tilde{C}^{j'}_{\mathbf{G}}(\mathbf{K}) \exp(i\{\mathbf{K}+\mathbf{G}\}\cdot\{\mathbf{R}-\Delta\mathbf{R}\}). \quad (2.7.7)$$

With the transformation given by by (2.7.4) the Bloch waves are changed by a phase factor $\Delta\mathbf{R}$, such that they now refer to the local origin of the lattice $\mathbf{R} - \Delta\mathbf{R}$. They then follow the tilt of the columns and the transformation allows an exact solution within the approximations made. Thus the modified transformation allows us to solve exactly the govering Schrödinger equation for a strained crystal where the strain causes the columns to tilt over. For strained crystals with slowly bending columns, where the bending may be approximated by a simple tilting of the columns, the modified transformation will give a good first order approximation to the solution. The modified equations will also be

used later on as the basis for finding better approximate solutions.

### 2.7.1 Modified 2-beam theory.

In the 2-beam case we proceed similar to the general modified transformation (2.7.1) to (2.7.3). However in order to keep the same form as in (2.5.4), and thus allow a general solution to be formed for both the unmodified and the modified cases, we shall instead of (2.7.4) use the unitary transformation

$$T_{\mathbf{S'S}} = \exp(\frac{i}{2}\{\mathbf{S'} - \mathbf{S}\} \cdot \Delta\mathbf{R})\ \delta_{\mathbf{S'S}}; \qquad \mathbf{S'} \neq \mathbf{S}. \tag{2.7.8a}$$

This is the same transformation as that used by Bird and Preston (1988),

$$\begin{pmatrix} \psi_{\mathbf{0}} \\ \psi_{\mathbf{G}} \end{pmatrix} = \begin{pmatrix} \exp(\frac{i}{2}\mathbf{G} \cdot \Delta\mathbf{R}) & 0 \\ 0 & \exp(-\frac{i}{2}\mathbf{G} \cdot \Delta\mathbf{R}) \end{pmatrix} \begin{pmatrix} \tilde{\psi}_{\mathbf{0}} \\ \tilde{\psi}_{\mathbf{G}} \end{pmatrix}. \tag{2.7.8b}$$

This transformation again involve a phase change and does not affect the intensity expressions. Applying the transformation, the 2-beam Howie-Whelan equations, (2.5.4), become

$$\begin{pmatrix} W - k\mathbf{G} \cdot \Delta\dot{\mathbf{R}} & \tilde{U}_{\mathbf{G}} \\ \tilde{U}_{\mathbf{G}} & -W + k\mathbf{G} \cdot \Delta\dot{\mathbf{R}} \end{pmatrix} \begin{pmatrix} \tilde{\psi}_{\mathbf{0}} \\ \tilde{\psi}_{\mathbf{G}} \end{pmatrix} = -2ik\frac{d}{dz} \begin{pmatrix} \tilde{\psi}_{\mathbf{0}} \\ \tilde{\psi}_{\mathbf{G}} \end{pmatrix}. \tag{2.7.9}$$

(2.7.9) shows a change similar to that of the $n$ beam case (2.7.5). The strain effects are felt by the diagonal terms and through the derivative of the displacement field.

Similar to the general case, discussed above, the solution to the modified Howie-Whelan equations, (2.7.9), for a crystal with tilted columns may be solved exactly. Then the solution found in section 2.5.1 may be applied, except now $W \rightarrow W - k\mathbf{G} \cdot \Delta\dot{\mathbf{R}}$, which is a constant. The diffracted intensity is then given by

$$I_{\mathbf{G}} = \frac{\tilde{U}^2}{(W - k\mathbf{G} \cdot \Delta\dot{\mathbf{R}})^2 + \tilde{U}^2} \sin^2(\sqrt{(W - k\mathbf{G} \cdot \Delta\dot{\mathbf{R}})^2 + \tilde{U}^2}\frac{z}{2k}). \tag{2.7.10}$$

Both equations (2.7.5), for the $n$ beam case, and (2.7.9), for the 2-beam case will be used in later chapters to approximate solutions to the HEED equations and to form diffraction patterns.

## 2.8 DISLOCATIONS.

In this section the type and nature of strain field to be used in actual calculations will be introduced. Thus far the type and nature of the strain field has been ignored and the equations are completely general in this respect. In actual calculations however a particular strain field must be used. The type of strain field to be used in this thesis will be that due to a dislocation. However the general results may be carried over to any type of strain field.

In this thesis only the two most simple types of dislocations will be considered, the screw and the edge dislocation. A screw dislocation is shown in figure 2.5a. In this two parts of the crystal are twisted parallel to the line of the dislocation. This in effect converts a stack of parallel atomic columns into a spiral ramp winding through the crystal around the dislocation line. The edge dislocation, figure 2.5b, may be thought of as a perfect crystal lattice which has an extra half columns of atoms. The boundary between the slipped and the unslipped regions is called the dislocation.

Dislocations may be described in terms of their Burgers vector, **b**. As shown in figure 2.6, a Burgers vector is that vector needed in a crystal containing a dislocation to complete the loop. This follows a similar atom to atom sequence to that taken around a closed loop in a perfect crystal. The Burgers vector of a screw dislocation is parallel to the line of the dislocation (figure 2.6), whilst that of an edge dislocation is normal (Hirsch *et al* 1977).

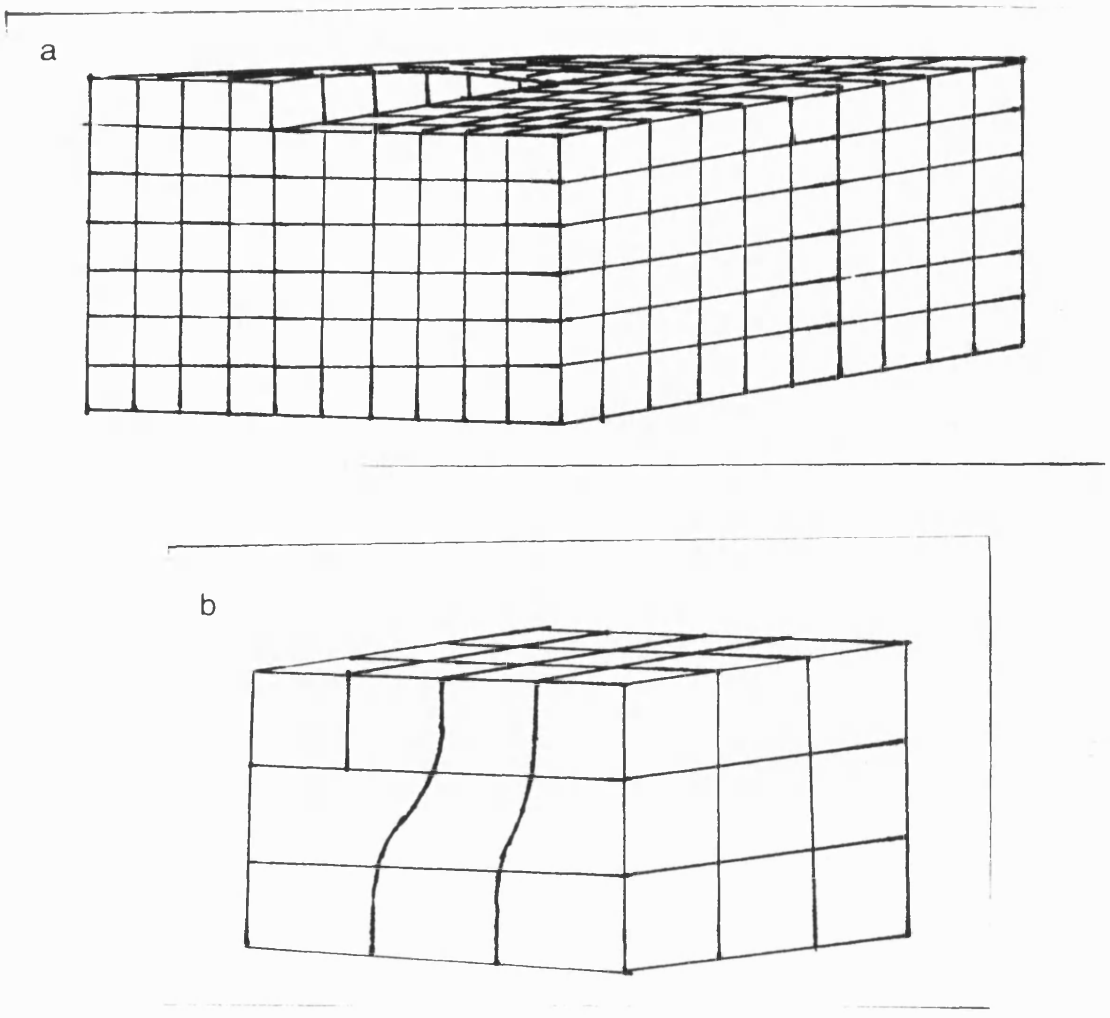


Figure 2.5 A screw and edge dislocation are shown in figures $a$ and $b$ respectively. The effect of the screw dislocation is to cause a displacement of the atoms, such that the atoms on either side of the dislocation line are shifted in opposite directions. In the edge dislocation the two halves of the crystal are compressed in the direction perpendicular to the dislocation line.

The displacement $\Delta\mathbf{r}$ at the point $\mathbf{r}$ due to a screw dislocation which runs parallel to the surface of an infinite isotropic crystalline slab may be written as

$$\Delta\mathbf{r} = \frac{\mathbf{b}}{2\pi}\vartheta \tag{2.8.1}$$

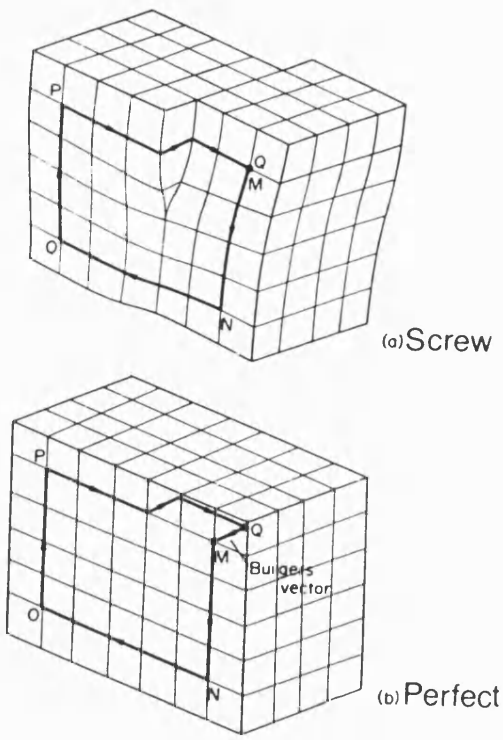


Figure 2.6 The Burgers vector is that vector need to complete an exact circuit around the dislocationi line. For a screw dislocation the Burgers vector $\mathbf{b}$ is parallel to the dislocation line $\mathbf{U}$ (whilst for an egde dislocation it is normal).

where

$$\vartheta = \arctan(\frac{z - z_0}{y}). \tag{2.8.2}$$

(Friedel 1964). In (2.8.2) $z$ is the depth of the point $\mathbf{r}$ in the crystal, $z_0$ is the depth of the dislocation, $y$ is the perpendicular distance from the dislocation to $\mathbf{r}$ and If an edge dislocation gives rise to the displacement and if the slip plane is parallel to the surface then the displacement is given by

$$\Delta\mathbf{r} = \frac{1}{2\pi}\left(\mathbf{b}\vartheta + \mathbf{b}\frac{\sin(\vartheta)}{4(1-\nu)} + (\mathbf{b}\wedge\mathbf{u})\left(\frac{1-2\nu}{2(1-\nu)}\ln(r) + \frac{\cos(2\vartheta)}{4(1-\nu)}\right)\right). \tag{2.8.3}$$

Here $\nu$ is Poisson's ratio, $\mathbf{u}$ is a unit vector in the positive sense of the dislocation and $\vartheta$ is again given by (2.8.2) (Friedel 1964).

# CHAPTER 3

# ADIABATIC ITERATION THEORY.

## 3.1 INTRODUCTION.

Having derived the governing equations of HEED we now in this chapter turn our attention to methods of solving them. A number of techniques exist which may be used to solve or approximate the solution to the HEED equations (see for example the books by Hirsch *et al* 1977; Cowley 1981, Buseck *et al* 1988 or Reimer 1984). Although there are many methods for formulating dynamical diffraction theory (e.g the wave-optical method by Howie and Whelan (1961) or the transmission and reflection method of Berry (1971)) two techniques, multi-slice and Bloch wave, have in one form or another been almost exclusively used.

In the multi-slice method (Cowley and Moodie 1957) an analytical approximation is made by using the concept of transmission through a number of very thin crystal slices. Computationally it has proved very efficient for the calculation of intensities where a large number (several hundred) of beams must be considered. It has also shown useful where the inclusion of absorption, 3-dimensional effects or various types of faults is desired (Goodman and Moodie 1974). However it can not provide the same insights into to the working of electron diffraction as other methods, such as the Bloch wave method (Bird 1989).

In the Bloch wave method (Humphreys 1979; Metherell 1976) diffraction effects are analysed by using the Schrödinger equation to describe the electron wave functions as a superposition of Bloch waves. Though computationally less efficient than the multi-slice method it has shown useful where an understanding

of the underlying diffraction effects is required, particularly where the number of beams needed can be limited or there are special symmetries involved (Bird 1989). Again it may be used to look at the effect of absorption, 3-dimensional effects or faults (Humphreys 1979; Bird 1989). It is of course the method we shall be using in this thesis.

The particular technique we shall be using here to approximate the solutions to the Schrödinger equation in a strained crystal is adiabatic iteration. In section 3.2.1 a general method for approximating the solution to a Schrödinger equation with an $n \times n$ Hamiltonian matrix is discussed. This method is based on the adiabatic iteration approximation developed by Berry (1987). As discussed in section 3.4 Berry's interest in adiabatic iteration was to find an expression for the geometric phase of a system taken adiabatically aound a closed loop (Berry 1984, 1987).

Our interest in using adiabatic iteration derives from the work of Bird and Preston (1988), who have shown for the 2-beam case that provided the lattice planes of a strained crystal are slowly bending adiabatic conditions may be assumed. Their interest was illustrating the connection between Berry's geometric phase (Berry 1984) and the bending of 2-beam fringes as a dislocation was crossed. In particular by using an adiabatic approximation method based on that of Berry (1987) together with modified Bloch wave theory (discussed in section 2.8), as well as demonstrating the geometric phase they have shown that adiabatic approximation provides a simple and useful technique for both calculating and interpretating diffraction intensities in strained crystals. In this thesis and in particular in this chapter we will concern ourselves with extending the work of

Bird and Preston in two ways. First in section 3.2.1 (and later in chapter 5) we extend the theory to include the general $n$-beam HEED equations. Second in section 3.2.2 (and later in chapter 4) further iterations are included, in an attempt to find better approximate solutions.

## 3.2 ADIABATIC ITERATION.

In section 3.2 a procedure for adiabatic iteration, as developed by Berry (1987), will be outlined. In section 3.2.1 a general method for solving a Schrödinger equation with an $n \times n$ hermitian Hamiltonian matrix will be derived and then in 3.2.2 the particular case where the hermitian Hamiltonian is an $2 \times 2$ matrix is looked at in more detail. We shall look at the specific application to HEED later in section 3.3.

Adiabatic changes are those in which the Hamiltonian is slowly varying. We shall return to the question of what slowly varying is, at the end of section 3.2.1. In such cases it is expected, because of the slow change, that the solutions to the Schrödinger equation may be approximated by means of the stationary states of the instantaneous Hamiltonian (Born and Fox 1928). In quantum adiabatic theory a system initally in a stationary state labelled by a certain set of quantum numbers, which undergoes adiabatic change, is expected to remain in a stationary state that is still labelled by the same quantum numbers, even though the environment has changed (Schiff 1968; Messiah 1966). The significance of the theory is that although the quantum states remain in a stationary state labelled by the same quantum numbers, the initial and final environments, and hence the stationary states, can be different. The only condition is that the change occurs slowly, but the total change is not necessarily small. Because the

Hamiltonian is in fact time dependent and in real situations the development must occur in a finite time, the change cannot be truly adiabatic. Adiabatic changes are thus an approximation.

### 3.2.1 The general case.

The case of interest is where the Hamiltonian which governs the development of the system is an $n \times n$ hermitian matrix. If the Hamiltonian evolves slowly, from time $t = 0$ to $T$, then adiabatic approximations may be used to form an approximate solution (Bohm 1951; Schiff 1968). The Schrödinger equation for such a Hamiltonian, where $\hbar = 1$, can be written as

$$\begin{pmatrix} H_{11_0} & H_{12_0} & \cdots & H_{1n_0} \\ H_{21_0} & H_{22_0} & \cdots & H_{2n_0} \\ \vdots & \vdots & \ddots & \vdots \\ H_{n1_0} & H_{n2_0} & \cdots & H_{nn_0} \end{pmatrix} \begin{pmatrix} \psi_{1_0} \\ \psi_{2_0} \\ \vdots \\ \psi_{n_0} \end{pmatrix} = i\frac{d}{dt} \begin{pmatrix} \psi_{1_0} \\ \psi_{2_0} \\ \vdots \\ \psi_{n_0} \end{pmatrix}, \qquad (3.2.1a)$$

or

$$\sum_k H_{lk_0}(t)\psi_{k_0}(t) = i\dot{\psi}_{l_0}, \qquad (3.2.1b)$$

for each coupled row $l$ in the Hamiltonian. The derivative in (3.2.1b), and throughout this section, is with respect to time, $t$. Here we have introduced the subscript notation to be used throughout this thesis. The first lower subscripts refer to the usual matrix notation whilst the second lower subscript refers to the number of iterations. The subscript 0 in (3.2.1) thus infers that this is the zeroth iteration (uniterated). Each element of the Hamiltonian in (3.2.1) is considered to be a function of time, $H_{lk_0} = H_{lk_0}(t)$.

As the time, $T$, in which the Hamiltonian develops is finite, the development is not truly adiabatic. It is assumed that non adiabatic effects are small and may be taken into account by introducing a slowness parameter $\xi$ into the Hamiltonian

in the form $\xi t$ (Berry 1987). In our particular case $\xi$ will be a measure of the strain in a crystal. In the limit that $\xi \rightarrow 0$ the development becomes truly adiabatic. The instantaneous Schrödinger equation of (3.2.1b) can be written in the form

$$\sum_k H_{lk_0}(t) N^j_{k_0}(t) = \lambda^j_0(t) N^j_{l_0}(t), \tag{3.2.2}$$

for each of the coupled rows $l$ in the Hamiltonian. Here the $N^j_{l_0}$ are the instantaneous eigenstates and $\lambda^j_0$ their respective eigenvalues. Because the Hamiltonian is a hermitian $n \times n$ matrix there are $n$ eigenvalue solutions, each labelled by $j$, and the instantaneous eigenstates may be chosen so that they are both orthogonal and normalised (Schiff 1968; Riley 1974), ie

$$\sum_l N^{j^*}_{l_0} N^{j'}_{l_0} = \delta_{j,j'}. \tag{3.2.3}$$

In what follows we assume the instantaneous eigenstates are also non degenerate (we shall discuss the reasons for this later). This defines the instantaneous eigenstates to within a phase factor (because the phases of the eigenstates $\psi_i$ are arbitrary) and they are made unique by the addition of a phase factor $\gamma^j_0$ such that they become parallel transported (Schiff 1968; Berry 1987). A parallel transported vector is one that is moved in a direction which is normal to the direction in which it points; i.e. $\dot{\mathbf{v}} \perp \mathbf{v}$. The instantaneous parallel transported eigenstates then become

$$\tilde{N}^j_{l_0}(t) = N^j_{l_0}(t) \exp(i\gamma^j_0(t)) \tag{3.2.4}$$

and now obey the parallel transport rule, which may be written as

$$\sum_l \tilde{N}^{j^*}_{l_0} \dot{\tilde{N}}^j_{l_0} = 0, \tag{3.2.5}$$

(see for example Berry 1987).

Substituting $\tilde{N}^j_{l_0}$, (3.2.4), into the parallel transport rule, (3.2.5), implies that

$$\gamma^j_0(t) = i\int_0^t dt' \sum_l N^{j^*}_{l_0}(t')\dot{N}^j_{l_0}(t'). \tag{3.2.6}$$

The normalisation condition, (3.2.3), implies that the sum over $l$ in (3.2.6) is imaginary and hence the parallel transported phase is real. This may be seen by differentiating (3.2.3), for $j = j'$, with respect to time. Then

$$\sum_l \dot{N}^{j^*}_{l_0} N^j_{l_0} + \sum_l N^{j^*}_{l_0} \dot{N}^j_{l_0} = 0. \tag{3.2.7}$$

The two terms in (3.2.7) are complex conjugates of each other and to add to zero they must be purely imaginary. Note that if the Hamiltonian is real for all time (as opposed to a general hermitian Hamiltonian) then the instantaneous eigenstates may be chosen to be real (Metherell 1976), and then there is no parallel transported phase, $\gamma^j_0 = 0$. It will be argued later in section 3.4 that the parallel transported phase is the same as Berry's geometric phase, and that (3.2.6) is effectively the same as the expression given by Berry (1984 and 1987).

**The first iteration.**

Here in this thesis we shall use adiabatic iteration to approximate the solutions to (3.2.1). This follows a similar iterative process to that of the adiabatic iterative technique of Berry (1987), but one related to our own particular needs, that is within a matrix formulation. In order to apply adiabatic iteration, we first change to a new state. By analogy with Berry (1987) we form the new state by applying a unitary transformation ($N^{j^*}_{l_0}$ is unitary by (3.2.3)) to the old state, such that each element of the new state becomes

$$\psi_{l_1} = \sum_k \tilde{N}^{l^*}_{k_0}\psi_{k_0}. \tag{3.2.8a}$$

Similarly, the original state can be found in terms of the new state by

$$\psi_{k_0} = \sum_l \tilde{N}^l_{k_0} \psi_{l_1}. \tag{3.2.8b}$$

By comparison with (3.2.1b), the Schrödinger equation for the new state is

$$\sum_k H_{lk_1}(t)\psi_{k_1}(t) = i\dot{\psi}_{l_1}. \tag{3.2.9}$$

In order to proceed further we need an expression for each element of the new Hamiltonian, $H_{lk_1}$. These may be found by using (3.2.8b) to substitute for $\psi_{k_0}$ in (3.2.1b). Then (3.2.1b) becomes

$$\sum_k H_{lk_0} \sum_j \tilde{N}^j_{k_0} \psi_{j_1} = i \sum_j \dot{\tilde{N}}^j_{l_0} \psi_{j_1} + i \sum_j \tilde{N}^j_{l_0} \dot{\psi}_{j_1}. \tag{3.2.10}$$

Rearranging (3.2.10) gives

$$\sum_j \left\{ \sum_k H_{lk_0} \tilde{N}^j_{k_0} - i\dot{\tilde{N}}^j_{l_0} \right\} \psi_{j_1} = i \sum_j \tilde{N}^j_{l_0} \dot{\psi}_{j_1}. \tag{3.2.11}$$

From (3.2.2) the sum over $k$ in (3.2.11) is equal to $\lambda^j_0 \tilde{N}^j_{l_0}$. Using this, multiplying (3.2.11) by $\tilde{N}^{j'^*}_{l_0}$ and summing over $l$ gives

$$\sum_j \left\{ \lambda^j_0 \sum_l \tilde{N}^{j'^*}_{l_0} \tilde{N}^j_{l_0} - i \sum_l \tilde{N}^{j'^*}_{l_0} \dot{\tilde{N}}^j_{l_0} \right\} \psi_{j_1} = i \sum_j \sum_l \tilde{N}^{j'^*}_{l_0} \tilde{N}^j_{l_0} \dot{\psi}_{j_1}. \tag{3.2.12}$$

Using conditions (3.2.3) and (3.2.5) this becomes

$$\sum_j \left\{ \lambda^j_0 \delta_{jj'} - i \sum_l \tilde{N}^{j'^*}_{l_0} \dot{\tilde{N}}^j_{l_0} (1 - \delta_{jj'}) \right\} \psi_{j_1} = i\dot{\psi}_{j'_1}. \tag{3.2.13}$$

Comparing (3.2.13) with (3.2.9), the elements of the new Hamiltonian can be seen to be given by the terms in { },

$$H_{j'j_1} = \lambda^j_0 \delta_{jj'} - i \sum_l \tilde{N}^{j'^*}_{l_0} \dot{\tilde{N}}^j_{l_0} (1 - \delta_{jj'}). \tag{3.2.14}$$

The new Hamilonian matrix may then be though of as being composed of two parts. The diagonal elements, which represent transitions to the same state $j \rightarrow j$ and the off-diagonal elements, which represent transitions to other states $j \rightarrow j'$ and are proportional to the slowness parameter $\xi$. This may be seen by differentiating (3.2.2) (having substituted $\tilde{N}$ for $N$) with respect to time. Then

$$\sum_k \left( \dot{H}_{lk_0} \tilde{N}^j_{k_0} + H_{lk_0} \dot{\tilde{N}}^j_{k_0} \right) = \dot{\lambda}^j_0 \tilde{N}^j_{l_0} + \lambda^j_0 \dot{\tilde{N}}^j_{l_0}. \tag{3.2.15}$$

We now multiply (3.2.15) by $N^{j'^*}_{l_0}$ where $j' \neq j$, and sum over $l$,

$$\sum_{lk} \left( \tilde{N}^{j'^*}_{l_0} \dot{H}_{lk_0} \tilde{N}^j_{k_0} + \tilde{N}^{j'^*}_{l_0} H_{lk_0} \dot{\tilde{N}}^j_{k_0} \right) = \sum_l \left( \dot{\lambda}^j_0 \tilde{N}^{j'^*}_{l_0} \tilde{N}^j_{l_0} + \lambda^j_0 \tilde{N}^{j'^*}_{l_0} \dot{\tilde{N}}^j_{l_0} \right). \tag{3.2.16}$$

From the orthonormalisation condition, (3.2.3), the first term on the right hand side of (3.2.16) is zero because we have defined $j \neq j'$. Also because the elements of the Hamiltonian $H_{lk_0}$ are hermitian, for the second term on the left hand side of (3.2.16) we may operate on $\tilde{N}^{j'^*}_{l_0}$ instead of $\dot{\tilde{N}}^j_{l_0}$ (Schiff 1968), giving

$$\begin{aligned} \sum_{lk} \tilde{N}^{j'^*}_{l_0} H_{lk_0} \dot{\tilde{N}}^j_{k_0} &= \sum_{kl} \dot{\tilde{N}}^j{}_{k_0} H^*_{kl_0} \tilde{N}^{j'^*}_{l_0} \\ &= \lambda^{j'^*}_0 \sum_k \dot{\tilde{N}}^j{}_{k_0} \tilde{N}^{j'^*}_{k_0}. \end{aligned} \tag{3.2.17}$$

But for a hermitian Hamiltonian the eigenvalues are real, that is $\lambda^{j'^*}_0 = \lambda^{j'}_0$. Thus the expression for the off-diagonal terms may be written as

$$\sum_l \tilde{N}^{j'^*}_{l_0} \dot{\tilde{N}}^j_{l_0} = \frac{\sum_{lk} \tilde{N}^{j'^*}_{l_0} \dot{H}_{lk_0} \tilde{N}^j_{k_0}}{\lambda^j_0 - \lambda^{j'}_0}; \qquad j' \neq j. \tag{3.2.18}$$

As discussed before $H_{lk_0} = H_{lk_0}(\xi t)$ and thus $\dot{H}_{lk_0}$ is of order $\xi$. Hence the off-diagonal terms in (3.2.14) may be written as (3.2.18), and are of order $\xi$. In the limit that $\xi \rightarrow 0$, the off-diagonal elements become zero, there are no transitions to other states and the development becomes truly adiabatic.

**Adiabatic approximation.**

Thus far everything is exact. Although we have approached the problem slightly differently from conventional adiabatic approximation, by transforming to a new state, the basic equations are effectively the same (see for example Schiff 1968 or Messiah 1966).

The adiabatic iteration approximation involves assuming that the off-diagonal terms in the new Hamiltonian $H_1$ may be ignored (set to zero) on the grounds that they are of order $\xi$, which is assumed to be small. The approximation thus involves ignoring transitions to other states and assumes that the development may be approximated as being truly adiabatic. As will be discussed later improvements are made by retransforming to a second new state, in a manner similar to that of before. It is hoped that each iteration will pull down a further term $\xi$ onto the off-diagonals and that the error in ignoring these terms will then be smaller by a factor $\xi$. Making the first approximation each row of the new Schrödinger equation, (3.2.9), becomes

$$\lambda_0^j(t)\psi_{j_1}(t) = i\dot{\psi}_{j_1}. \tag{3.2.19}$$

The solutions of (3.2.19) for each row integration are

$$\psi_{j_1}(t) = A_1^j \exp(-i\int_0^t \lambda_0^j(t')\,dt'), \tag{3.2.20}$$

where there are $n$ values of $j$. In (3.2.20) $A_1^j$ is a constant of integration and can be found from the boundary conditions at $t = 0$. From (3.2.20) and (3.2.8a) at $t = 0$ the constant $A_1^j$ is given by

$$A_1^j = \psi_{j_1}(0) = \sum_k \tilde{N}_{k_0}^{j^*}(0)\psi_{k_0}(0). \tag{3.2.21}$$

Then substituting (3.2.20) and (3.2.21) into (3.2.8b) the approximate solution to the Schrödinger equation (3.2.1) is given by

$$\psi_{l_0}(t) = \sum_j \tilde{N}^j_{l_0}(t) \exp(-i \int_0^t \lambda_0^j(t')\, dt') \sum_k \tilde{N}^{j^*}_{k_0}(0) \psi_{k_0}(0), \qquad (3.2.22)$$

Provided adiabatic conditions apply, (3.2.22) gives the first iteration approximate solution to the Schrödinger equation (3.2.1). The approximate wavefunction is described as a linear combination of the instantaneous eigenstates, each of which has a different eigenvalue. The amplitude $A^j$ of each eigenstate is assumed to be constant (i.e. time-independent) and changes to the eigenstates are felt through the time-dependent instantaneous eigenstates and their respective time-dependent eigenvalues.

**Estimation of the error.**

In making the adiabatic iteration an approximation has been made. As has been discussed this approximation assumes that scattering from a state $j$ into a different state $j'$ is small and may be ignored. There is then no transfer of amplitude from one state into another different state. This is only true when the Hamiltonian varies infinitely slowly in time. Because the development of the Hamiltonian occurs in time $T$ it cannot be truly adiabatic and an error has been introduced.

An estimation of the error in making the approximation can be found letting the probability amplitude vary slowly with time, $A_1^j = A_1^j(t)$. To first order we may write

$$A_1^j(t) = A_1^j + \delta A_1^j(t), \qquad (3.2.23)$$

where $\delta A_1^j(t)$ is small compared to $A_1^j$. Whenever the total change in $A_1^j(t)$ is

small, it is expected that the approximation will be good, but becomes increasingly bad as the total change becomes large. The first order changes to the new state (3.2.20) are

$$\delta\psi_{j_1}(t) = \delta A_1^j(t)\exp(-i\int_0^t \lambda_0^j(t')\,dt'). \tag{3.2.24}$$

The total change in $\delta A_1^j(T)$ can be estimated by substituting the new state $\psi_{j_1} + \delta\psi_{j_1}$ into the governing Schrödinger (3.2.9). This becomes

$$\sum_{j'}(H_{jj_1'} + \delta H_{jj_1'})(\psi_{j_1'} + \delta\psi_{j_1'}) = i\dot{\psi}_{j_1} + i\delta\dot{\psi}_{j_1}, \tag{3.2.25}$$

where $H_{jj_1'}$ and $\delta H_{jj_1'}$ are the respective on- and off-diagonal Hamiltonians. By making use of the previous work for the on-diagonal Hamiltonian and its solution (3.2.20), and by also ignoring all higher order terms, (3.2.25) may be simplified to

$$\sum_{j'\neq j} \delta H_{jj_1'}\ \psi_{j_1'} + \lambda_0^j\ \delta\psi_{j_1} = i\ \delta\dot{\psi}_{j_1}. \tag{3.2.26}$$

Making use of (3.2.24) and (3.2.20), (3.2.26) then becomes

$$\begin{aligned}\sum_{j'\neq j} \delta H_{jj'_1}\ A_1^{j'}\exp(-i\int_0^t \lambda_0^{j'}\,dt') + \lambda_0^j\ \delta A_1^j\exp(-i\int_0^t \lambda_0^j\,dt') \\ = \lambda_0^j\ \delta A_1^j\exp(-i\int_0^t \lambda_0^j\,dt') + i\ \delta\dot{A}_1^j\exp(-i\int_0^t \lambda_0^j\,dt').\end{aligned} \tag{3.2.27}$$

Cancelling and rearranging, then gives

$$\int_0^T \delta\dot{A}_1^j\,dt = -i\sum_{j'\neq j} A_1^{j'}\int_0^T dt\ \delta H_{jj'_1}\exp(-i\int_0^t\{\lambda_0^{j'} - \lambda_0^j\}dt'), \tag{3.2.28}$$

and by use of (3.2.14), to first order, the change in the amplitudes is

$$\int_0^T \delta\dot{A}_1^j\,dt = -\sum_{j'\neq j} A_1^{j'}\int_0^T dt\exp(-i\int_0^t\{\lambda_0^{j'} - \lambda_0^j\}dt')\sum_l \tilde{N}_{l_0}^{j^*}\dot{\tilde{N}}_{l_0}^{j'}. \tag{3.2.29}$$

Equation (3.2.29) describes how the amplitude of the $j$ state is transfered to and from other states. It may be solved using computational methods to the required accuracy. Whenever the total change is small, there is little exchange of amplitude between states and it is expected that the adiabatic approximation will be good. The total change is from (3.2.18), through the sum over $l$, proportional to $\xi$.

This also allows us to ask the question, when do adiabatic conditions apply? From (3.2.29) together with (3.2.18) we see that a condition for the approximation to be good may be written as

$$\frac{1}{\lambda_0^j - \lambda_0^{j'}} \sum_{lk} N_{l_0}^j \dot{H}_{lk_0} N_{l_0}^{j'} \ll 1. \tag{3.2.30}$$

This tells us that provided the change in the Hamiltonian as the system evolves from $t = 0$ to $t = T$ is small compared to the energy differences, adiabatic conditions will apply (Bohm 1951), and the adiabatic iteration technique may be applied (we also see from (3.2.29) that if the exponential term varies fast enough then $\delta A_1^j$ will be even smaller).

We may now also return to the question of degeneracy. Thus far we have assumed that the instantaneous eigenstates are non degenerate. The reason for this is, were they to be degenerate, there may be some $j' \neq j$ for which the eigenvalues would be such that $\lambda_0^j \simeq \lambda_0^{j'}$ and their respective off-diagonal terms may from (3.2.18) become very large. There could then be a large transfer of amplitude between states $j$ and $j'$ and adiabatic theory would no longer apply. Hence in order to ensure that adiabatic conditions apply we must have non degenerate instantaneous eigenstates.

**Further iterations.**

Further improvements to the approximation may be made by not ignoring the off-diagonal terms in (3.2.14). Instead the process is repeated by regarding the new Hamiltonian $H_1$ as having instantaneous eigenstates $N^j_{l_1}$ and respective eigenvectors $\lambda^j_1$. We then proceed as exactly as before. The iteration process may of couse be repeated again and again. Then equations (3.2.1) to (3.2.29) are repeated but with a change of subscript, $m \rightarrow (m+1)$ and $(m+1) \rightarrow (m+2)$, for $m = 0, 1, 2, \ldots$ .

In general if we have made $m+1$ iterations then by analogy with (3.2.8) the $(m+1)^{th}$ state will be

$$\psi_{l_{m+1}} = \sum_k \tilde{N}^{l^*}_{k_m} \psi_{k_m}, \tag{3.2.31a}$$

and transforming back to the $m^{th}$ state

$$\psi_{k_m} = \sum_l \tilde{N}^l_{k_m} \psi_{l_{m+1}}. \tag{3.2.31b}$$

The development of the new state $\psi_{l_{m+1}}$ is governed by the Schrödinger equation

$$\sum_k H_{lk_{m+1}}(t)\psi_{k_{m+1}}(t) = i\dot{\psi}_{l_{m+1}}. \tag{3.2.32}$$

The instantaneous Schrödinger equation for the $m^{th}$ iteration is

$$\sum_k H_{lk_m}(t)N^j_{k_m}(t) = \lambda^j_m(t)N^j_{l_m}(t), \tag{3.2.33}$$

and by comparison with (3.2.14) the elements of the $(m+1)^{th}$ Hamiltonian are

$$H_{lk_{m+1}} = \lambda^k_m \delta_{lk} - i\sum_j \tilde{N}^{l^*}_{j_m}\dot{\tilde{N}}^k_{j_m}(1-\delta_{lk}). \tag{3.2.34}$$

As was done in the first iteration the off-diagonals of (3.2.34) are now ignored. For the $(m+1)^{th}$ iteration they are of order $\xi^{m+1}$ (Berry 1987).

Having droped the off-diagonal terms in (3.2.34), the approximate solution to the Schrödinger equation (3.2.32) is

$$\psi_{k_{m+1}} = A^j_{m+1} \exp(-i \int_0^t \lambda^j_m dt'). \tag{3.2.35}$$

Using (3.2.31b) to transform back to the original state, the approximation to the solution of the initial Schrödinger equation (3.2.1) is given by

$$\psi_{k_0} = \sum_l \tilde{N}^l_{k_0} \sum_{l'} \tilde{N}^{l'}_{l_1} \cdots \sum_{l^{(m)}} \tilde{N}^{l^{(m)}}_{l^{(m-1)}_m} A^{l^{(m)}}_{m+1} \exp(-i \int_0^t \lambda^{l^{(m)}}_m dt') \tag{3.2.36}$$

where from (3.2.31b) and (3.2.21) at $t = 0$ the probability amplitude $A^{l^{(m)}}_{m+1}$ is given by

$$A^{l^{(m)}}_{m+1} = \sum_j \tilde{N}^{l^{(m)}*}_{j_m}(0) \sum_{j'} \tilde{N}^{j^*}_{j'_{m-1}}(0) \cdots \sum_{j^{(m)}} \tilde{N}^{j^{(m-1)}*}_{j^{(m)}_0}(0) \psi_{j^{(m)}_0}(0). \tag{3.2.37}$$

Similar to the derivation of (3.2.29) an estimation of the total change in the $(m+1)^{th}$ probability amplitude is given by

$$\int_0^T \delta \dot{A}^{j'}_{m+1}\, dt = -\sum_{j \neq j'} A^j_{m+1} \int_0^T dt\ \exp(-i \int_0^t \{\lambda^j_m - \lambda^{j'}_m\} dt') \sum_l \tilde{N}^{j'*}_{l_m} \dot{\tilde{N}}^j_{l_m}. \tag{3.2.38}$$

The error in the $(m+1)^{th}$ iteration is then through the sum over $l$ proportional to $\xi^{m+1}$.

Provided adiabatic conditions apply (3.2.36) then gives the $(m+1)^{th}$ approximate solution to the Schrödinger equation (3.2.1). The instantaneous eigenstates and eigenvalues can be found from (3.2.33), which may be solved using computational methods, and the parallel transported phase is given by (3.2.6). An estimation of the error in the approximation can be found from (3.2.38). These two results, (3.2.36) and (3.2.38), are the fundamental results of this section.

As pointed out by Berry (1987) the iteration scheme must eventually fail for all but the most simple cases (an example where it does not fail is discussed in chapter 5). This failure is due to the breakdown of adiabatic conditions. As we transform to moving frames in an attempt to follow the evolving state ever more closely, the path taken by the Hamiltonian becomes ever more rapidly varying and at some stage the path taken is no longer adiabatic. Adiabatic iteration then becomes a worse approximation.

### 3.2.2 The 2-beam case.

One of the cases in which we are interested is the Howie-Whelan equations (2.5.4), where the Hamiltonian is a $2 \times 2$ matrix. In this section we shall use the analytical iteration technique derived in the previous section to approximate the solutions of a Schrödinger equation with a general $2 \times 2$ hermitian Hamiltonian matrix. The advantage of the simple 2-beam case is that the solution to the Schrödinger equation may be easily approximated using just analytic methods, and so allow further insight into adiabatic iteration. The 2-beam case also brings out many of the most important aspects of the adiabatic iteration technique which are not easily shown by the general n-beam case.

Let a general Hermitian Hamiltonian be written as

$$H_0(t) = \begin{pmatrix} z_0 & r_0 \exp(i\varphi_0) \\ r_0 \exp(-i\varphi_0) & -z_0 \end{pmatrix}, \tag{3.2.39}$$

where $z_0$, $r_0$ and $\varphi_0$ are all functions of $t$. We also define $r_0$ to be a smooth continuous functions which does not change sign as the Hamiltonian evolves. If $r_0$ does change sign then the sign dependence may be taken into the exponential by rewriting $r_0$ as $|r_0| \exp(i\pi W(t))$, where $W(t)$ is the appropriate step

function. The reason for this, as discussed further in section 4.7, is to make the equation more manageable. From (3.2.1a) the Schrödinger equation governing the development of $H_0$, with $\hbar = 1$, may be written in the form

$$\begin{pmatrix} z_0 & r_0 \exp(i\varphi_0) \\ r_0 \exp(-i\varphi_0) & -z_0 \end{pmatrix} \begin{pmatrix} \psi_{1_0} \\ \psi_{2_0} \end{pmatrix} = -i\frac{d}{dt} \begin{pmatrix} \psi_{1_0} \\ \psi_{2_0} \end{pmatrix}. \tag{3.2.40}$$

The $-ve$ sign is inserted to make the equations equivalent to the Howie-Whelan equations (and hence of those of Bird and Preston 1988). This change makes only a slight alteration to the adiabatic theory derived and is pointed out where necessary.

The Hamiltonian is again assumed to evolve slowly in time $T$ such that adiabatic conditions apply. As discussed in section 3.2.1 small non adiabatic effect are taken into account by introducing the slowness parameter $\xi$ into $H_0$, and hence into $z_0$, $r_0$ and $\varphi_0$, in the combination $\xi t$. As shown in appendix A, the instantaneous eigenstates of (3.2.39), for $j = 1, 2$, are

$$\begin{pmatrix} \tilde{N}^j_{1_0} \\ \tilde{N}^j_{2_0} \end{pmatrix} = \frac{\exp(i\gamma^j_0)}{\sqrt{2}} \begin{pmatrix} \exp(i\varphi_0/2)(1 + \frac{z_0}{\lambda^j_0})^{1/2} \\ \pm \exp(-i\varphi_0/2)(1 - \frac{z_0}{\lambda^j_0})^{1/2} \end{pmatrix}, \tag{3.2.41}$$

where the $+ve$ sign is for $j = 1$ and the $-ve$ sign for $j = 2$. The respective eigenvalues of (3.2.41) are given by

$$\lambda^1_0 = -\lambda^2_0 = \sqrt{z_0^2 + r_0^2}. \tag{3.2.42}$$

The instantaneous eigenstates are defined up to a time dependent phase, $\gamma^j_0$, and are made unique by insisting that they are parallel transported, obeying (3.2.5). The parallel transported phase $\gamma^j_0$ (again shown in appendix A) is then given by

$$\gamma^j_0(t) = -\frac{1}{2}\int_0^t \frac{z_0}{\lambda^j_0}\dot{\varphi}_0 dt'. \tag{3.2.43}$$

As with the eigenvalues, the parallel transported phases of states 1 and 2 are equal and opposite. Note that the phase $\gamma_0^j$ must be real because $z_0$, $\lambda_0$ and $\varphi_0$ are all real functions. Also if $\varphi_0$ is constant or if $z_0 = 0$ for all time, then there is no parallel transported phase.

In order to approximate the solution to the Schrödinger equation we now use the adiabatic iteration theory developed in the section 3.2.1. We again form a new evolving state by applying a unitary transformation to the old state such that each element of the new state is given by (3.2.8a). From (3.2.9) the corresponding Schrödinger equation for the new state is

$$H_1 \begin{pmatrix} \psi_{1_1} \\ \psi_{2_1} \end{pmatrix} = -i\frac{d}{dt} \begin{pmatrix} \psi_{1_1} \\ \psi_{2_1} \end{pmatrix}, \tag{3.2.44}$$

where again a $-ve$ sign is inserted to keep the original form of (3.2.39). The expression for the new Hamiltonian $H_1$ is, from (3.2.14), given by

$$H_1 = \begin{pmatrix} \lambda_0^1 & i\sum_l \tilde{N}_{l_0}^{1^*} \dot{\tilde{N}}_{l_0}^2 \\ i\sum_l \tilde{N}_{l_0}^{2^*} \dot{\tilde{N}}_{l_0}^1 & \lambda_0^2 \end{pmatrix}. \tag{3.2.45}$$

In the simplest adiabatic approximation the off-diagonal terms are ignored on the grounds that they are of order $\xi$. As shown in appendix B the off-diagonal terms ($j \neq j'$) can be written as

$$i\sum_l \tilde{N}_{l_0}^{j'^*} \dot{\tilde{N}}_{l_0}^j = \frac{i}{|\lambda_0^{j'}|} \left( \frac{ir_0\dot{\varphi}_0}{2} - \frac{(r_0\dot{z}_0 - \dot{r}_0 z_0)}{2\lambda_0^{j'}} \right) \exp(-2i\gamma_0^{j'}). \tag{3.2.46}$$

Thus the off-diagonal terms are through $\dot{\varphi}$, $\dot{z}_0$ and $\dot{r}_0$, proportional to the slowness parameter $\xi$.

The solution to (3.2.44), where we have dropped the off-diagonal terms, is given by

$$\psi_{j_1}(t) = \exp(i\int_0^t \lambda_0^j(t')\,dt') \sum_k \tilde{N}_{k_0}^{j^*}(0)\psi_{k_0}(0). \tag{3.2.47}$$

Then upon transforming back to the initial state, the first order adiabatic approximate solution to (3.2.39) is

$$\psi_{l_0}(t) = \sum_j \tilde{N}^j_{l_0}(t) \exp(i \int_0^t \lambda^j_0(t')\, dt') \sum_k \tilde{N}^{j^*}_{k_0}(0)\psi_{k_0}(0), \qquad (3.2.48)$$

The only effect of the change of sign in (3.2.39) (and (3.2.44)) is to change the sign in the exponential, $\lambda^j \to -\lambda^j$. Apart from this, (3.2.48) is equivalent to (3.2.22) and the interpretation there may be carried across.

As discussed in the previous section, by using (3.2.29) and (3.2.46), together with the change of sign $\lambda^j \to -\lambda^j$, the first adiabatic approximation is expected to be good whenever

$$\left| \int_0^T \left[ \frac{i r_0 \dot{\varphi}_0}{2\lambda^{j'}_0} - \frac{(r_0 \dot{z}_0 - \dot{r}_0 z_0)}{2(\lambda^{j'}_0)^2} \right] \exp(-2i\gamma^{j'}_0 - 2i \int_0^t \lambda^{j'}_0\, dt') dt \right| \ll 1. \qquad (3.2.49)$$

From (3.2.49) the error is proportional to $\xi$ through the terms $\dot{z}_0$, $\dot{r}_0$ and $\dot{\varphi}_0$. Note that if none of these three terms vary with time then there is no error and the approximation is exact. This is the trivial case in which the Hamiltonian is constant in time.

Provided adiabatic conditions apply (3.2.48) gives the first order approximate solution to a Schrödinger equation with a $2 \times 2$ matrix Hamiltonian. It is completely general and therefore may be used to approximate the solutions to either the unmodified or the modified 2-beam Howie-Whelan equations, (2.5.4) or (2.7.9). An estimation of the error in the approximation can be found from (3.2.49). These equations, (3.2.48) (together with equations (3.2.41) to (3.2.43)) and (3.2.49), are the fundamental result of this section. The process may of course be iterated, as discussed in section 3.2.1, and higher order approximate solutions found.

## 3.3 ADIABATIC ITERATION AND HEED

Now let us return to the problem of HEED. We are interested in finding an analytical solution, or approximation to the solution, of the HEED equations (2.6.1a). Here the Hamiltonian may be written as an $n \times n$ matrix, where the elements of the Hamiltonian are given by (2.6.1b). We see upon comparing (2.6.1) with (3.2.1), as was discussed before in section 2.2, that the only difference in form between the two is that the variable depth ($z$) has replaced that of time ($t$). Thus provided adiabatic conditions apply we may use the theory derived in the previous section to analytically solve or approximate the HEED equations.

Previously adiabatic conditions apply when the Hamiltonian does not vary greatly in time, thus in HEED adiabatic conditions will apply provided the Hamiltonian does not vary greatly with depth. Because the HEED equations have been constructed by using the column approximation, within each column the 2-dimensional layers are periodic in the $\mathbf{R}$ direction but may be shifted by $\Delta\mathbf{R}(z)$ in the $x-y$ direction, as shown in figure 3.1. The bending of the columns is described by the shift of the 2-dimensional layers, $\Delta\mathbf{R}$, hence the condition we need to satisfy in order to use adiabatic iteration is that $\Delta\mathbf{R}$ is slowly varying with depth. Non adiabatic effects may then be taken into account by introducing the slowness parameter into $\Delta\mathbf{R}(\mathbf{R}, \xi z)$.

In order to get a better understanding of what the adiabatic approximate solution to the HEED equations will look like, let us first look at the case of an undeformed crystal, where the Hamiltonian does not vary with depth. Then, as already stated in section 3.2.1, both the instantaneous eigenstates, $\tilde{N}^j_{l_0}$, and the eigenvalues, $\lambda^j_0$, are also independent of depth, there is no parallel transported

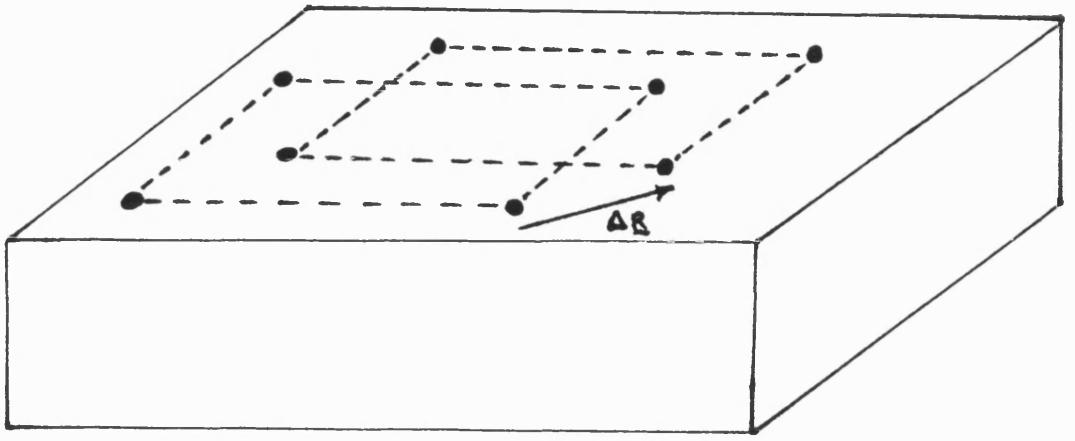


Figure 3·1. The periodic nature of the atomic layers in the 2-d $\mathbf{R}$ plane is unaltered by the strain field. The strain field instead, shifts each $\mathbf{R}$ plane by an amount $\Delta\mathbf{R}$, which is a function of depth only. Provided $\Delta\mathbf{R}$ varies slowly with depth, adiabatic conditions will be satisfied and the adiabatic iteration scheme may be used.

phase, $\gamma_0^j = 0$, and the probability amplitudes, $A_0^j$, are constant. Comparing the exact solution to the HEED equations (2.6.2) derived in section 2.6.1, with the adiabatic solution (3.2.22) derived in the previous section, we can see that the two solutions are the same. It can be seen that the instantaneous eigenstates are the 2-dimensional Bloch wave coefficients, the eigenvalues are their respective transverse energies and the probability amplitudes are the excitation amplitudes.

Now let us look at what happens when we introduce a strain into the crystal.

It is assumed that the crystal lattice columns are varying sufficiently slowly that adiabatic conditions apply. The introduction of a strain field causes the Bloch wave coefficients and their transverse energies to become $z$ dependent, (3.2.2). This arises from the separation of the wavefunction in to its transverse and longitudinal components. For the unmodified HEED equations (2.6.1), the first iteration approximation then assumes that scattering of amplitude between states is small and may be ignored. The error in assuming this is, from (3.2.18), proportional to $\dot{H}$. But, as discussed, $z$ enters $H$ in the form $\Delta\mathbf{R}(z)$ and thus the error in making the first approximation is proportional to $\Delta\dot{\mathbf{R}}$. The first iteration thus assumes that the columns which are in fact bending may be approximated by the undeformed solution which has gained an extra phase factor (the geometric phase), and makes an error which is proportional to the first derivative of the column bending (the slope). Similarly the second iteration of the unmodified equations (or the first iteration of the modified equations) assumes that the column bending may be approximated by including the first derivative (the slope) and the error is then proportional to the second derivative of the column bending (the curvature).

In general the $n^{th}$ iteration of the unmodified HEED equations includes the $(n-1)^{th}$ derivative of the bending but ignores all higher derivatives. For the modified HEED equations however, the hamiltonian is proportional to $\Delta\dot{\mathbf{R}}$ and thus the $n^{th}$ iteration approximation includes the $n^{th}$ derivative of the bending but ignores all higher derivatives. It is thus expected that the $n^{th}$ iteration of the modified HEED equations will form a better approximate solution than that of the $n^{th}$ iteration of the unmodified HEED equations.

Adiabatic approximation has a number of advantages in HEED. Far away from a strain field core it is a good approximation and to first order gives the intensity in terms of phase contrast (due to the geometric phase). The Bloch wave interpretation of the undeformed crystal can be carried across to that for a strained crystal. The technique also allows the whole process to be iterated and thus a better approximation found. It also allows a simple insight into the important phenonema in HEED of electron channelling. Adiabatic iteration lets us look at the questions, *how well do electrons follow column bending in a strained crystal and what effects does this have on diffraction patterns.* The reason that adiabatic iteration illuminates this is because each iteration looks at the importance and effects of including the next derivative in the bending. The adiabatic iteration technique derived is general and may be used to approximate solutions to either the unmodified HEED equations (2.6.1) or the modified HEED equations (2.7.5).

As we have seen, though, there are a number of disadvantages. After the first few iterations the mathematics involved can become quite involved (for example see section 4.7). Each iteration depends upon the previous and so leads to greater computer running time and more computer memory needed (i.e. for $m$ iterations the instantaneous Schrödinger equation must be solved $m+1$ times). Although each iteration may provide a better approximation, their relative improvement is only proportional to the slowness parameter and so each iteration will produce less and less improvement. Also for all but the most simple strain fields the technique will eventually fail and will begin to form worse approximations (Berry 1987). The technique is then not able to look at a number of interesting problems

in HEED, such what happens at dislocation core or interfaces.

## 3.4 THE GEOMETRIC PHASE.

As has been mentioned, the parallel transported phase used in adiabatic iteration is a geometric phase. In this section we shall try to justify this claim. However whether or not it is true, the adiabatic iteration process already derived is in no way changed and is still valid. The present section may thus be read as an aside which complements rather than adds to adiabatic iteration theory.

As discussed by Berry (1984), a quantal system which is adiabatically taken around a closed loop in some parameter space $\mathbf{R}$, will upon returning to its starting point have gained an extra phase. As the system is taken around the cycle, the environment through which the system travels causes a change in the phase of the wavefunction. Upon returning to the initial starting point a comparison of the initial and the final wavefunctions gives the relative change in the phase. A dynamical phase is generated by the time it takes to complete the cycle and a geometric phase by the geometry of the path taken. To show this, let a hermitian Hamiltonian $H$ be taken adiabatically around a closed circuit $C$ in some parameter space $\mathbf{R}$ in time $t = T$, where $T$ is large enough so that adiabatic conditions apply. The Schrödinger equation, with $\hbar = 1$, which describes the development of the state $|\psi\rangle$ may be written as

$$H(\mathbf{R}(t))|\psi(t)\rangle = i|\dot{\psi}(t)\rangle. \tag{3.4.1}$$

Now because the development is adiabatic, at each instance of time the instantaneous eigenstates $|n(\mathbf{R})\rangle$ with energies $E_n(\mathbf{R})$ satisfy

$$H(\mathbf{R})|n(\mathbf{R})\rangle = E_n(\mathbf{R})|n(\mathbf{R})\rangle. \tag{3.4.2}$$

A system which is initially in the instantaneous eigenstate $|n(\mathbf{R}(0))\rangle$ will evolve adiabatically through $H(t)$ into the instantaneous eigenstate $|n(\mathbf{R}(t))\rangle$. Then $|\psi\rangle$ may be written as

$$|\psi\rangle = \exp(-i\int_0^t E_n(\mathbf{R}(t'))\,dt')\exp(i\gamma_n(t))|n(\mathbf{R}(t))\rangle \tag{3.4.3}$$

(Schiff 1968; Berry 1984). The first exponential term in (3.4.3) is the dynamical phase, whilst the second exponential term is the geometrical phase of interest. By substituting (3.4.3) into (3.4.1), making use of (3.4.2) and multipling by $\langle\psi^*|$ the equation for the geometric phase becomes

$$\begin{aligned}\dot{\gamma}_n(t) =& i\langle n(\mathbf{R}(t))|\dot{n}(\mathbf{R}(t))\rangle \\ =& \langle n(\mathbf{R}(t))|\nabla_{\mathbf{R}} n(\mathbf{R}(t))\rangle \cdot \dot{\mathbf{R}}(t).\end{aligned} \tag{3.4.4}$$

Then integrating both sides of (3.4.4) from $t = 0$ to $t = T$, ie over the closed circuit $C$, gives

$$\gamma_n(C) = i\int_C \langle n(\mathbf{R})|\nabla_{\mathbf{R}} n(\mathbf{R})\rangle \cdot d\mathbf{R}. \tag{3.4.5}$$

The geometric phase depends only on the geometry of the path taken and the initial state of the system and not on the time taken, provided adiabatic conditions apply (Berry 1984, 1987).

Comparing (3.4.5) with (3.2.6), it can be seen that the extra phase used in the adiabatic iteration scheme is an effective geometric phase, the only difference being the paths taken. In fact the path need not be closed to generate a geometric phase. A closed loop is needed when the geometric phase is found by comparison of the wave function with itself at the same position and at times $t = 0$ and $t = T$. We are dealing with a superposition of Bloch waves, each propagating with different phases. Because we are dealing with relative phases,

it is not necessary for the path to be closed in order to generate a geometric phase (Bird and Preston 1988).

Because the geometric phase in adiabatic iteration has been generated in a somewhat artificial manner, by adding an extra phase to the instantaneous eigenstates so they become parallel transported, equation (3.2.4), it might be thought that they will have no actual effect, simply disappearing when the intensities, $I = |\psi|^2$, are considered. In fact this need not be so. They may have a real effect when the wavefunctions are a linear combination of waves. For example, in the case of interest, a beam of electrons incident upon a perfect crystal will be split by the potential into a number of Bloch waves, each Bloch wave having a different wavevector (or phase). The different paths taken by each Bloch wave as they travel through the crystal give rise to different geometric phases. Then interference between Bloch waves having differing phases can give rise to real effects, as will be seen in chapters 4 and 5.

# CHAPTER 4

## LARGE ANGLE CONVERGENT BEAM ELECTRON DIFFRACTION.

In this and the following chapter we will be concerned with exploiting the adiabatic iteration theory developed in chapter 3 to approximate the solutions to the HEED equations. First in this chapter Large Angle Convergent Beam Electron Diffraction (LACBED) will be analysed using 2 beam theory, and then in chapter 5 Scanning Transmission Electron Microscopy (STEM) will be analysed using the general $n$ beam theory. To this end a brief introduction to LACBED, and the effects of a strain field upon it, are discussed in sections 4.1 and 4.2. In the next section 4.3, in order to make them more manageable, the governing 2 beam Howie-Whelan equations are made dimensionless. In section 4.4 the exact solutions are found using computational methods for a number of cases. Then in the following five sections, 4.5 to 4.9, both adiabatic iteration and modified theories are used to find approximate solutions for a number of differing situations. In the last section, 4.10, an explanation of the fringe following rule (Bird and Preston 1988) is given.

## 4.1 LARGE ANGLE CBED.

In CBED the incident beam is a convergent cone of high energy electrons. As shown in figure 4.1, the cone is narrow, of order one degree or less, and is focussed onto the top surface of a crystal specimen. The area illuminated is of order 100Å in width. It is usual (eg Bird 1989) to assume that the probe consists of a set of independent plane waves $\exp(i\mathbf{k}\cdot\mathbf{r})$. In truth though, the waves cannot truly be independent, or it would not be possible to form a focussed probe.

However provided the probe size does not become as small as the unit cell size of the specimen, the probe may be treated as being composed of independent waves (Carpenter and Spence 1984). The principle effect of the crystal specimen is to Bragg diffract the incident plane waves by reciprocal lattice vectors **g**. Since each of the incident wavevectors **k** is effectively independent of the others, a CBED pattern consists of a set of discs. Each disc represents a map of the diffracted intensity as a function of the incident wavevector **k** for the reciprocal lattice vector **g**.

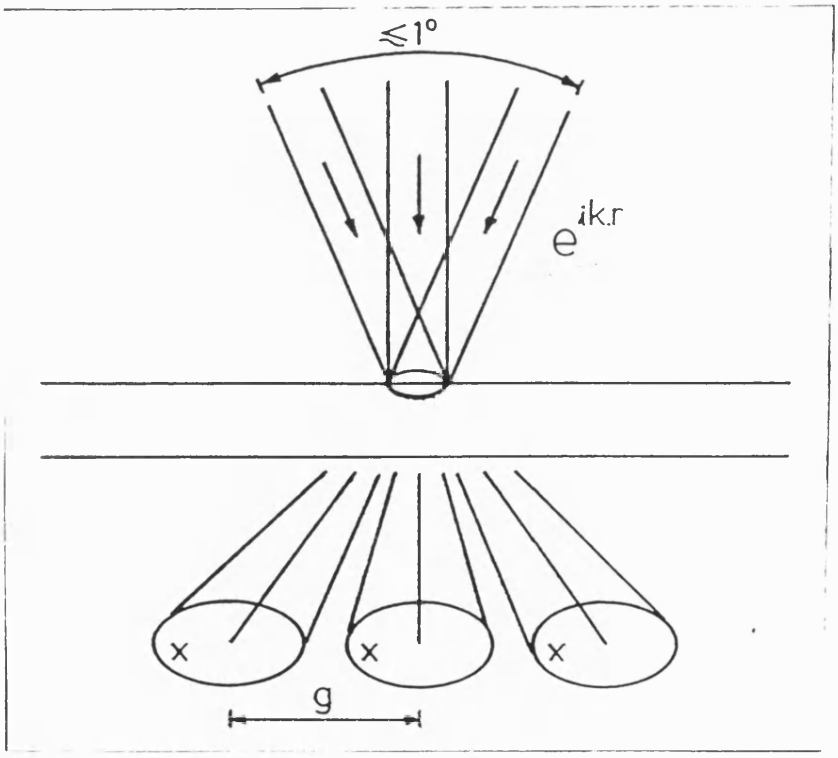


Figure 4.1 A convergent beam of independent plane waves, of angular spread less than $1^{\circ}$, combining to form an incident probe.

A number of the successes of electron diffraction in crystallography have been

achieved using CBED techniques. Examples of these include the determination of crystal point and space groups (Buxton *et al* 1976), local lattice strain measurements (Jones, Rackham and Steeds 1977; Vincent, Preston and King 1988) and the determination of one or two crystal structures (Vincent, Bird and Steeds 1984a,b). A review of the many uses of CBED is given in the article by Steeds in Hren *et al* (1979); as well as in the papers by Bird (1989); Cherns and Preston (1989); Eaglesham (1989); Tanaka (1989) and Vincent (1989) (see also the other papers contained within these two journals).

One of the limitations of CBED is that the angular field of view is limited by the Bragg angle of the nearest reflection. In order that the Bragg discs do not overlap, and thus overcomplicate the interpretation, it is necessary to limit the beam angle convergence to less than the Bragg angle. This difficulty may be overcome by using LACBED. In LACBED, the cone of incident plane waves is focussed under or over the specimen and the angle of incidence is much greater, of order a few degrees wide (Tanaka *et al* 1980). The cone may again be imagined to be an ensemble of plane wave sections, each section passes through a different part of the crystal, as shown in figure 4.2. The area illuminated by each individual section is still of order 100Å in width, but the total area illuminated by the probe is now of order $1\mu$m. This again leads to the disc diffraction pattern as in conventional CBED, each disc being a superposition from all the individual sections of the incident beam. The resulting diffraction discs are separated out and each disc, related to reciprocal lattice vector $\mathbf{g}$, can be looked at in turn in the microscope.

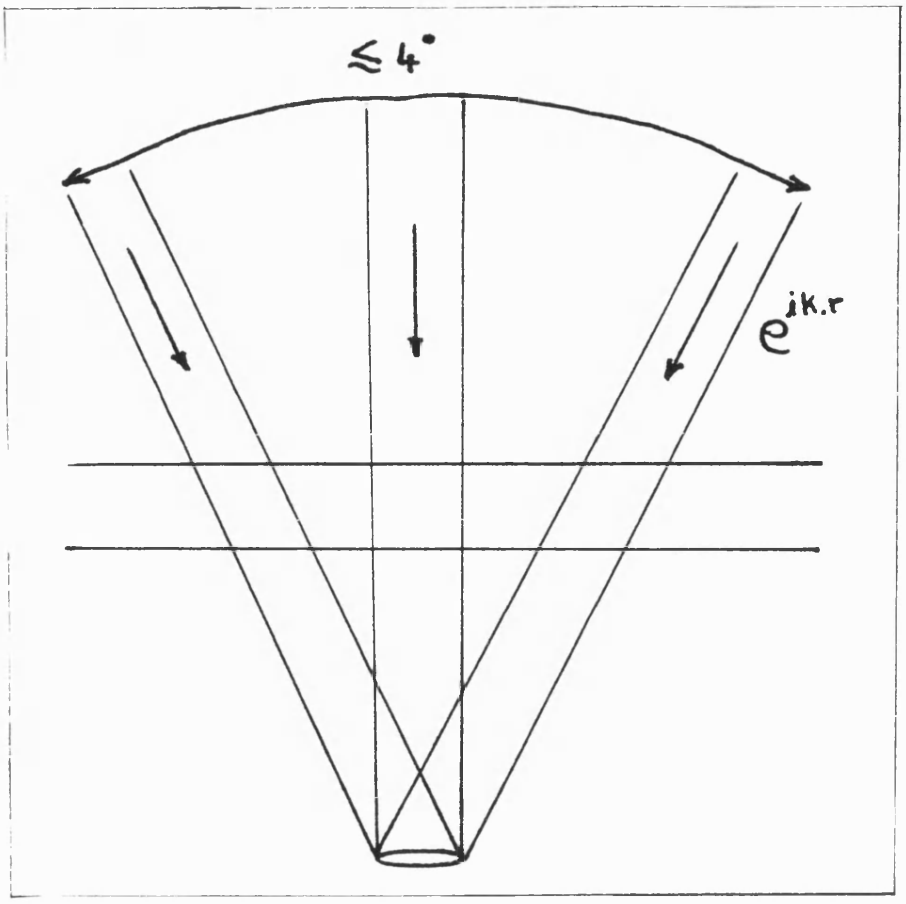


Figure 4.2 In LACBED each independent convergent beam passes through a different crystal column. The angular width of the beam is now of order a few degrees, and the total area illuminated of order $1\mu$m.

We may now ask the question *What does a LACBED pattern look like ?* The intensity at the bottom of an crystal column is a function of the position of the column ($\mathbf{r}$) and of the wavevector ($\mathbf{k}$) of the electrons incident upon that column. The resultant LACBED pattern is thus a map through both real and reciprocal space. It is because LACBED patterns contains both real space and reciprocal space information that they are particularly suited to studying defects in crystals (Cherns and Preston 1989). We shall now look at the construction of a 2-beam LACBED pattern (because we will only be concerning ourselves with 2-beam theory in this chapter and because 2-beam suits LACBED particularly well as

real and reciprocal information are completely seperated). Figure 4.3 shows the image superimposed on a diffraction pattern for a perfect crystal. Each dot represents a position at the bottom surface of the crystal and the arrows represent the respective wavevectors passing through that particular part of the crystal (length representing magnitude, and direction representing angle of incidence). The diffracting reciprocal lattice vector is represented by the arrow labelled **G**.

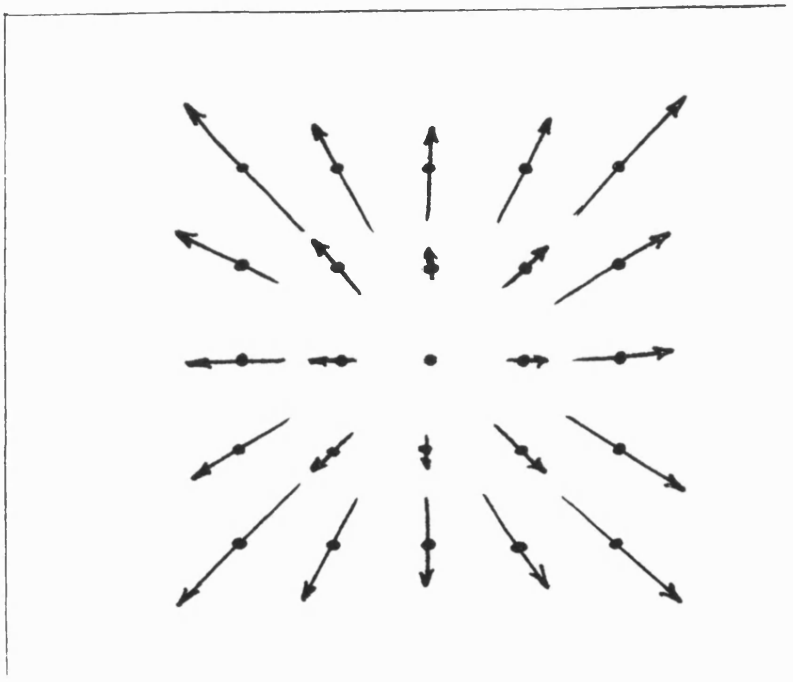

Figure 4.3 The superposition of real and reciprocal information on an LACBED image. Each dot represents an atomic column (real space) and the arrows represent the respective electron wavevectors (reciprocal space) at that position.

Now significant constructive interference will occur whenever the Bragg condition is (approximately) satisfied. Hence we need only consider that part of the wavevector **k** which lies parallel to the diffracting reciprocal lattice vector **G**. But due to the radial symmetry of the probe, all wavevectors which lie on the

same line perpendicular to $\mathbf{G}$ will have the same value of $\mathbf{K} \cdot \mathbf{G}$. A 2-beam LACBED pattern for a perfect crystal is thus composed of a series of straight lines of constant intensity, running the length of the pattern, perpendicular to $\mathbf{G}$. All those wavevectors $\mathbf{K}$ which lie on the line $\mathbf{K} = -\mathbf{G}/2$ will satisfy the Bragg condition, $2\mathbf{K}.\mathbf{G} + G^2 = 0$, and thus may give constructive interference.

## 4.2 LACBED AND STRAIN EFFECTS.

During the past decade there has been a growing interest in using CBED techniques to study strained crystals. Carpenter and Spence (1982) and Fung (1985) have studied the splitting of HOLZ lines and distortion of the ZOLZ induced by dislocations using CBED. They have shown that the splitting of the HOLZ lines can be used to determine the Burgers vector of the dislocation when the condition $\mathbf{g} \cdot \mathbf{b} = 0$ is satisfied. However the main difficulties involved in using CBED are the overlapping diffraction patterns and in knowing the exact position of the probe relative to the dislocation. By using LACBED these difficulties can in principle be overcome. Using LACBED techniques, Cherns and Preston (1986) have proposed that the direction and magnitude of a dislocation's Burgers vector may be found using the splitting of the diffraction lines in a LACBED pattern. This method can be used not only at $\mathbf{g} \cdot \mathbf{b} = 0$, but also when $\mathbf{g} \cdot \mathbf{b} = n$, where $n$ is any integer. Since then Cherns, Kiely and Preston (1988) have shown that LACBED techniques can be used to detect distortions due to misfit strains in bicrystals and in principle to measure strains in multilayers. In an extensive and detailed study Tanaka, Terauchi and Kanayama (1988) have examined the influence of dislocations on both ZOLZ and HOLZ diffraction lines. They have shown for a large number of cases that the effect of crossing the dislocation

line is to split the diffraction line into a number of subsidiary lines. As was proposed by Cherns and Preston (1986), Tanaka *et al* (1988) have shown that, *when Kinematic theory applies*, the number, $n$, of subsidiary lines crossed is such that

$$|\mathbf{g} \cdot \mathbf{b}| = n + 1. \tag{4.2.1}$$

Cherns and Preston (1989) have studied the effects of dislocations on the HOLZ lines of LACBED patterns. They have found that the effect of a dislocation is to both displace and to split the HOLZ lines which cross the dislocation into a number of subsidiary fringes. These subsidiary fringes can then be used to find the dislocation's Burgers vector. The sign of the Burgers vector can be identified from the deviation of the susidiary fringes upon crossing the dislocation line and the value of $|\mathbf{g} \cdot \mathbf{b}|$ can be obtained from the number of subsidiary fringes $n$ between the main HOLZ lines, according to (4.2.1).

The effects of dislocations on ZOLZ LACBED patterns in Si have been studied experimentally by Wen *et al* (1989) and using computer simulations by Lu *et al* (1990). They have found a similar shift of ZOLZ lines and demonstated that the sense and the direction of the dislocation's Burgers vector can be found from these shifts. The effect of a screw dislocation is to shift one half of the crystal columns in the direction of the Burgers vector, so that in a LACBED pattern the lines of constant intensity bend as they approach and then cross the dislocation line. An edge dislocation, which lies parallel to the surface, will cause the crystal columns to be tilted in the direction of the Burgers vector and perpendicular to the dislocation line. This produces a shift in an LACBED pattern such that the lines of constant intensity are either compressed or elongated in the direcction

of the Burgers vector.

## 4.3 THE DIMENSIONLESS HOWIE-WHELAN EQUATIONS.

In order to solve the 2-beam Howie-Whelan equations for both the unmodified case, (2.5.4), and for the modified equations, (2.7.8), we shall follow the method used by Bird and Preston (1988). This involves making the Howie-Whelan equations dimensionless. We need then not worry about the various units involved. The transformation is made by using the substitutions

$$x = \frac{Wt}{2k},\ y = \frac{2R}{t},\ \beta = \frac{\tilde{U}t}{2k},\ \theta = \frac{2z}{t}. \tag{4.3.1}$$

Here $x$, $y$ and $\beta$ are all dimensionless parameters and $\theta$ a dimensionless variable. The particular choice of scaling factors arises from the decision to make the only variable in the equations, $z$, both dimensionless and run from $-1$ to $+1$. The other directions in the crystal, $\mathbf{R}$, are then scaled by the same factor, $2/t$, and the two other parameters follow from these choices. Effectively $x$ represents the deviation away from the exact Bragg condition and thus represents a parameter in reciprocal space. $y$ represents the distance from the strain field core to the column, and is thus a parameter in real space. If there is no strain field core, $\mathbf{R}$ must be defined from some other point (an example is discussed later). $\beta$ represents the potential (here $\tilde{U} = |U|$) and in terms of the extinction distance ($\xi$) is given by $\beta = \pi t/\xi$. $\theta$ is the depth in the crystal which runs from $\theta = -1$ to $+1$. The only variable is written as

$$\phi = \mathbf{G} \cdot \mathbf{\Delta R} \tag{4.3.2}$$

and so $\phi = \phi(y, \theta)$. Using substitutions (4.3.1) and (4.3.2) the unmodified 2-

beam Howie-Whelan equations (2.5.4) become

$$\frac{1}{2}\begin{pmatrix} x & \beta\exp(i\phi) \\ \beta\exp(-i\phi) & -x \end{pmatrix}\begin{pmatrix} \psi_{\mathbf{0}} \\ \psi_{\mathbf{G}} \end{pmatrix} = -i\frac{d}{d\theta}\begin{pmatrix} \psi_{\mathbf{0}} \\ \psi_{\mathbf{G}} \end{pmatrix}, \tag{4.3.3}$$

where we have dropped the hat notation. The boundary conditions at $\theta = -1$ remain $\psi_{\mathbf{0}}(-1) = 1$ and $\psi_{\mathbf{G}}(-1) = 0$. In comparison with the work in chapter 3, equation (3.2.40), the only "time" dependent variable is $\phi$. We may attempt to solve equations (4.3.3) together with its boundary conditions using either computational or analytical methods.

## 4.4 COMPUTATIONAL SOLUTIONS.

By noting that the Howie-Whelan equations are complex, we should expect that the wave function solutions are also complex. Writing the wavefunctions in terms of their real ($\Re$) and their imaginary ($\Im$) parts, $\psi_{\mathbf{0}} = \psi_{\mathbf{0}}(\Re) + i\psi_{\mathbf{0}}(\Im)$ and $\psi_{\mathbf{G}} = \psi_{\mathbf{G}}(\Re) + i\psi_{\mathbf{G}}(\Im)$, we may rewrite equations (4.3.3) as four coupled first order differential equations,

$$\begin{aligned}
x\psi_{\mathbf{0}}(\Re) + \beta\cos(\phi)\psi_{\mathbf{G}}(\Re) - \beta\sin(\phi)\psi_{\mathbf{G}}(\Im) &= \;\; 2\dot{\psi}_{\mathbf{0}}(\Im) \\
x\psi_{\mathbf{0}}(\Im) + \beta\sin(\phi)\psi_{\mathbf{G}}(\Re) + \beta\cos(\phi)\psi_{\mathbf{G}}(\Im) &= -2\dot{\psi}_{\mathbf{0}}(\Re) \\
\beta\cos(\phi)\psi_{\mathbf{0}}(\Re) + \beta\sin(\phi)\psi_{\mathbf{0}}(\Im) - x\psi_{\mathbf{G}}(\Re) &= \;\; 2\dot{\psi}_{\mathbf{G}}(\Im) \\
\beta\cos(\phi)\psi_{\mathbf{0}}(\Im) - \beta\sin(\phi)\psi_{\mathbf{0}}(\Re) - x\psi_{\mathbf{G}}(\Im) &= -2\dot{\psi}_{\mathbf{G}}(\Re).
\end{aligned} \tag{4.4.1}$$

The boundary conditions at $\theta = -1$ are given by $\psi_{\mathbf{0}}(\Re) = 1$, $\psi_{\mathbf{0}}(\Im) = 0$, $\psi_{\mathbf{G}}(\Re) = 0$ and $\psi_{\mathbf{G}}(\Im) = 0$.

A number of library subroutines exist to solve these particular types of coupled first order differential equations. It is thus possible, given the boundary conditions and the values for $x$, $\beta$ and $\phi(\theta)$, to solve equations (4.4.1) to within some small and negligible computational error. The intensity of the diffracted beam

$I_G$ at the lower side of the specimen, $\theta = 1$, may then be found and by taking a scan through both real ($y$) and reciprocal ($x$) space a LACBED pattern formed.

Figures 4.4 to 4.15 show the computed LACBED patterns for a number of different cases. Each was made using Numerical Algorithm Group (NAG) library subroutine d02baf to solve (4.4.1). The patterns consist of a 64 by 64 square grid in which each square is shaded according to the same scaled intensity at that point. The greatest intensity (scaled 1) is represented by a completely white square and the least intensity (scaled 0) by a completely dark square. In all the patterns the real space parameter runs from $y = -4$ to $y = 4$, the reciprocal space parameter from $x = -25$ to $x = 25$ and the potential parameter $\beta = 2.85$ (Bird and Preston 1988). As we shall see, with this value of $\beta$ the scattering is dynamical. Kinematic theory, and so equation (4.2.1), is then almost certainly failing.

Figure 4.4 shows the LACBED pattern for the case of a perfect undeformed crystal. The pattern consists of a number of fringes of constant intensity running in straight parallel lines in the real space, $y$, direction. The fringes closest to the line $x = 0$ are most intense, and become less intense further away. There are two most intense lines and a symmetry about the line $x = 0$. All of these features can be understood from the solution for the intensity of an undeformed crystal (2.5.6b), which using substitutions (4.3.1) can be written as

$$I_G(1) = \frac{\beta^2}{x^2 + \beta^2} \sin^2(\sqrt{x^2 + \beta^2}). \tag{4.4.2}$$

In (4.4.2) there is no dependence upon the real space parameter $y$, the intensity is symmetric about the reciprocal space point $x = 0$ and is expected to vary as

a sine function, which due to the factor $1/(x^2 + \beta^2)$ loses amplitude rapidly as $x$ increases.

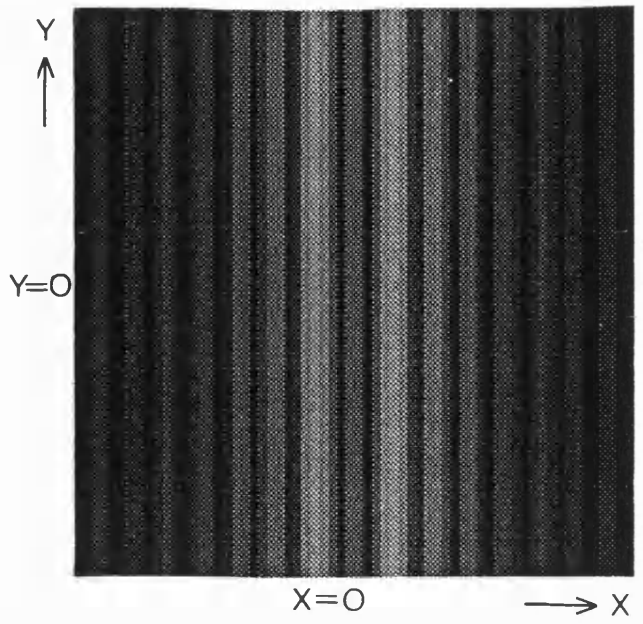


Figure 4.4 LACBED pattern for an undeformed crystal.

Figures 4.5a, 4.6a and 4.7a show the LACBED patterns for a crystal containg a screw dislocation, with $\Delta\mathbf{R}$ given by (2.8.1). The dislocation lies in the plane of the crystal at the centre (i.e. at depth $\theta_0 = 0$). The dislocation's Burgers vector $\mathbf{b}$ is such that it lies parallel to $\mathbf{G}$, with values $\mathbf{G} \cdot \mathbf{b}/2\pi$=1, 2 and 3 respectively. As with the unstrained case, figure 4.4, in each of the strained cases there are the same number of fringes running parallel to one another, throughout the length of the pattern from $y = -4$ to $y = +4$, and far away from the dislocation line the fringes run in straight parallel lines. In contrast, as the dislocation line is approached the fringes bend and appear to join up with another fringe upon crossing the dislocation line (seen most clearly away from the Bragg condition, $x = 0$).

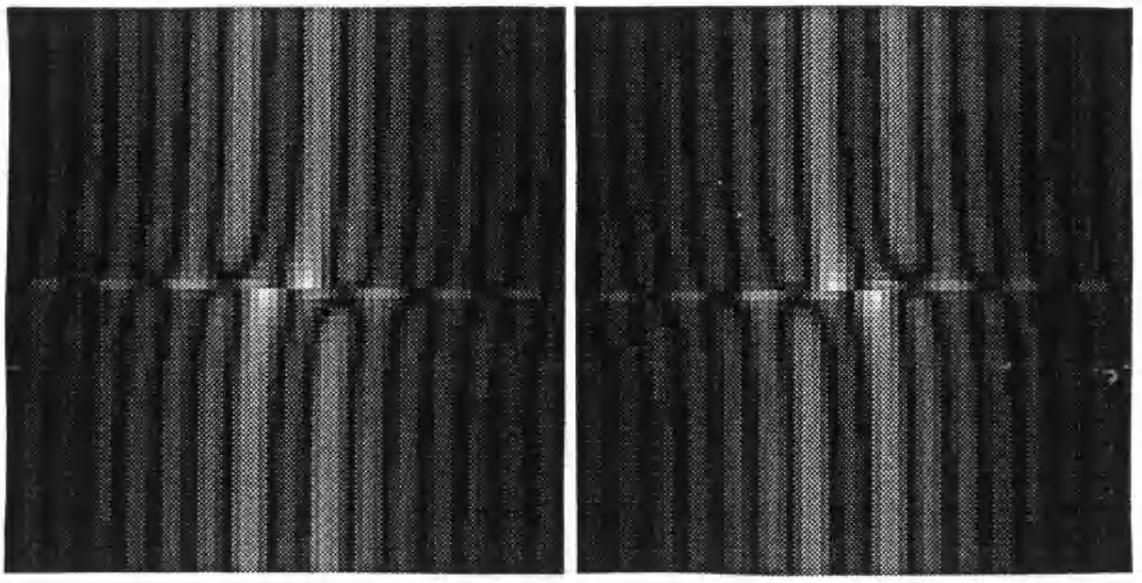

Figures 4.5a&b LACBED pattern for a crystal containing a central screw dislocation.

Figure a (left) with $\mathbf{G} \cdot \mathbf{b}/2\pi = 1$ and figure b (right) with $\mathbf{G} \cdot \mathbf{b}/2\pi = -1$.

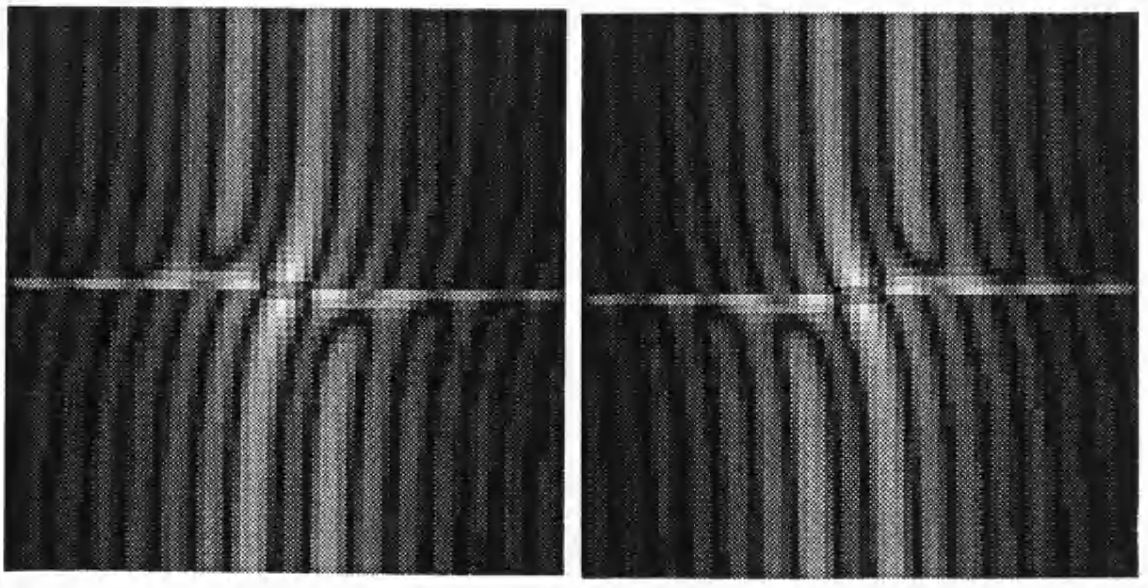

Figures 4.6a&b LACBED pattern for a crystal containing a central screw dislocation.

Figure a (left) with $\mathbf{G} \cdot \mathbf{b}/2\pi = 2$ and figure b (right) with $\mathbf{G} \cdot \mathbf{b}/2\pi = -2$.

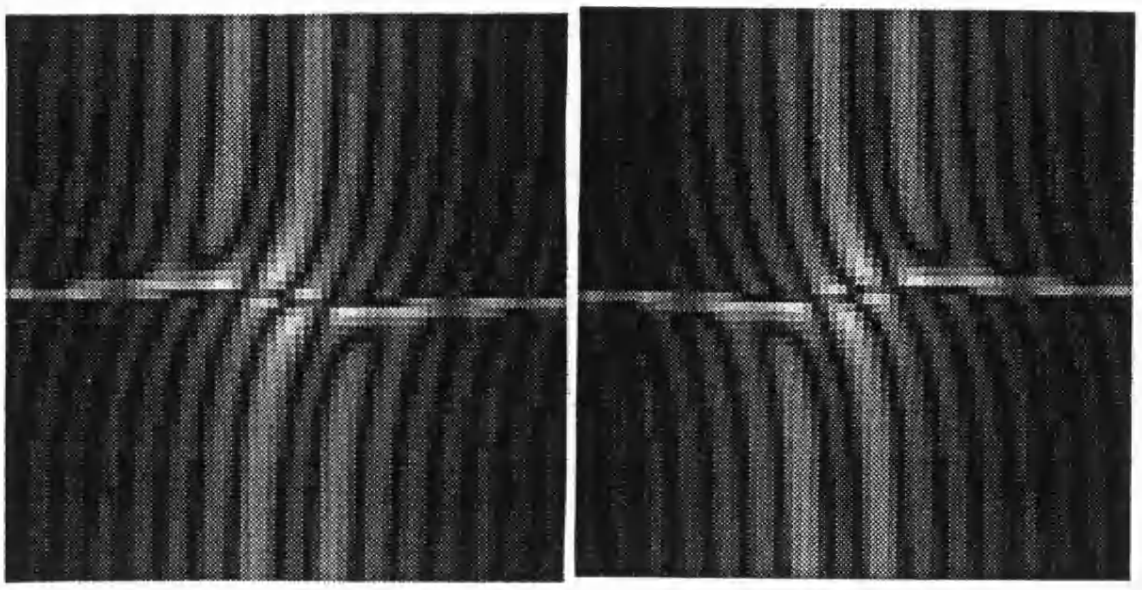

Figures 4.7a&b LACBED pattern for a crystal containing a central screw dislocation.

Figure a (left) with $\mathbf{G} \cdot \mathbf{b}/2\pi = 3$ and figure b (right) with $\mathbf{G} \cdot \mathbf{b}/2\pi = -3$.

At the dislocation core these fringes appear to join up giving the appearence of a line running over the dislocation; c.f. the weak beam method (e.g. Ray and Cockayne 1971 or Carter and Hirsch 1977) where the image of the dislocation is due to the lattice planes close to the dislocation core being locally tilted into the Bragg condition.

Figures 4.5b, 4.6b and 4.7b show LACBED patterns for a crystal again containing a centrally located screw dislocation. Now however the direction of the dislocation line is in the opposite direction. The Burgers vectors is again parallel to $\mathbf{G}$, but with with values $\mathbf{G} \cdot \mathbf{b}/2\pi = -1$, $-2$ and $-3$ respectively. In comparing the respective figures, parts a and b, we see that the only effect of

changing the sign of the Burgers vector is to change the direction in which the fringes bend. Hence by studying the direction of the fringe bending, relative to a known reciprocal lattice vector, the direction of $\mathbf{b}$ for a screw dislocation may be found.

The dynamical fringe following rule (Bird and Preston 1988) suggests that, in a LACBED pattern of a crystal containing a dislocation, the number and direction of "shifted fringes" is given by the expression $\mathbf{G}\cdot\mathbf{b}/2\pi$. For example in the case $\mathbf{G}\cdot\mathbf{b}/2\pi = 2$, figure 4.6a, the right hand most dark fringe before the dislocation, $y < 0$, appears to join up with the left hand most dark fringe upon crossing the dislocation, $y > 0$. In doing so it shifts by 2 fringes away from the right hand most dark fringe in the direction of the Burgers vector, and jumps over 1 subsidiary fringe (c.f. the kinematic rule (4.2.1)). Note, though, that (4.2.1) was based upon kinematic diffraction (valid close to the Bragg condition) whereas the more general dynamical fringe following rule works best away from the bragg condition, $x = 0$ (see figures 4.5 to 4.15). Also similar to (4.2.1) the dynamical fringe following rule allows us to find the magnitude of the dislocation's Burgers vector in the direction of the diffracting reciprocal lattice vector, though it says nothing of its magnitude in perpendicular directions. We shall return to the question of why this rule arises in section 4.10.

Figures 4.8 and 4.9, parts (a) and (b), show the LACBED patterns for a crystal containing an edge dislocation, with $\Delta\mathbf{R}$ given by (2.8.3). The dislocation's Burgers vector $\mathbf{b}$ is such that it lies parallel to $\mathbf{G}$ and with values for patterns (a) of $\mathbf{G}\cdot\mathbf{b}/2\pi$=2 and 3 respectively. The values of Poisson's ratio is taken to be $\nu = 0$. The figures show almost identical results to those for a screw dislocation.

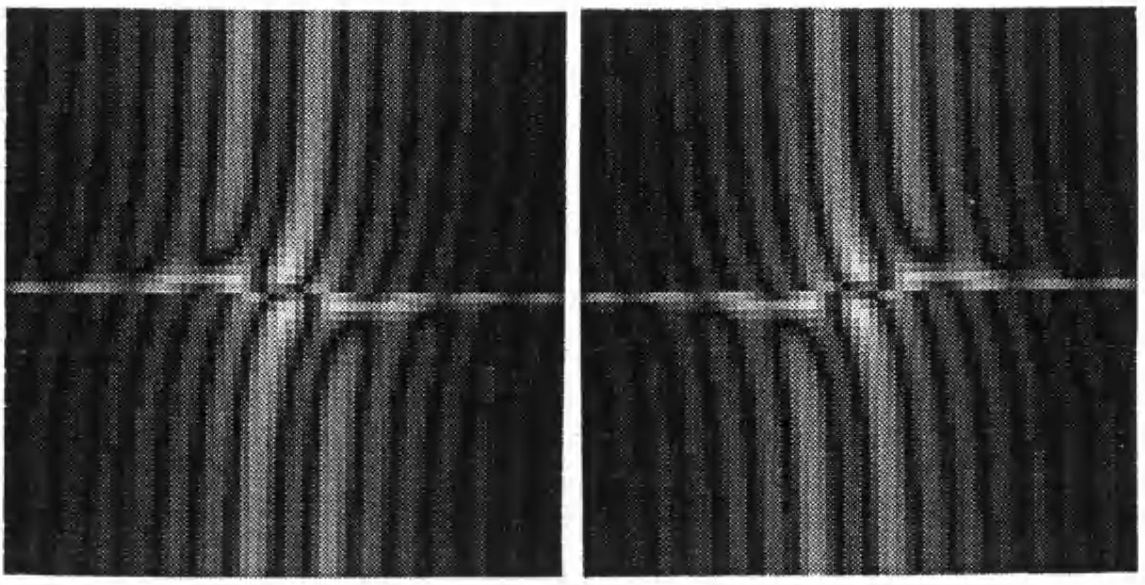

Figures 4.8a&b LACBED pattern for a crystal containing a central edge dislocation, with $\nu = 0$. Figure a (left) with $\mathbf{G} \cdot \mathbf{b}/2\pi = 2$ and figure b (right) with $\mathbf{G} \cdot \mathbf{b}/2\pi = -2$.

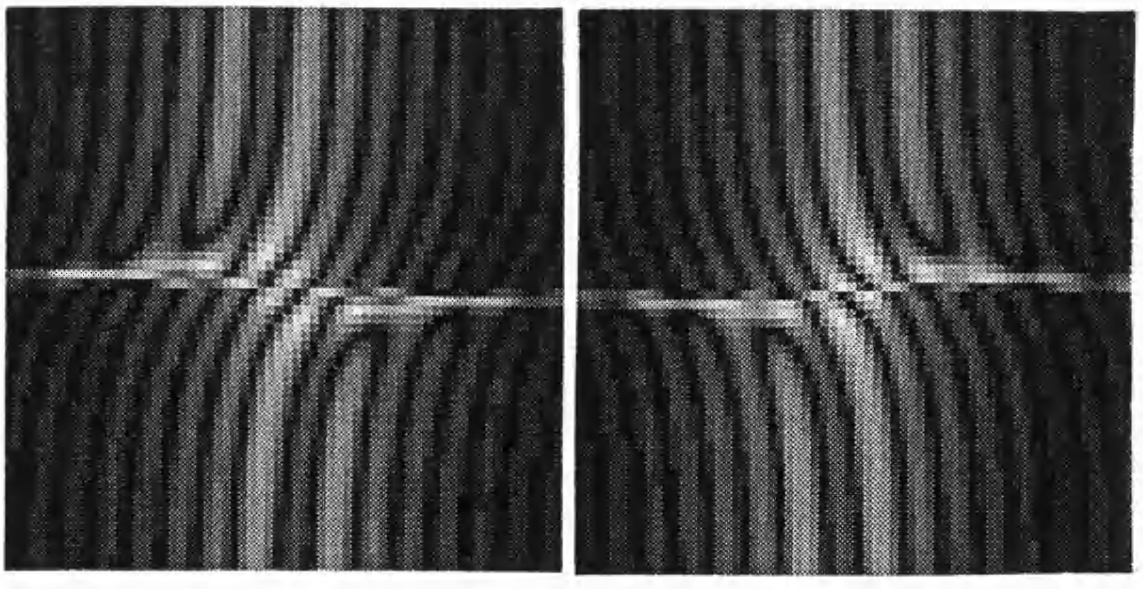

Figures 4.9a&b LACBED pattern for a crystal containing a central edge dislocation, with $\nu = 0$. Figure a (left) with $\mathbf{G} \cdot \mathbf{b}/2\pi = 3$ and figure b (right) with $\mathbf{G} \cdot \mathbf{b}/2\pi = -3$.

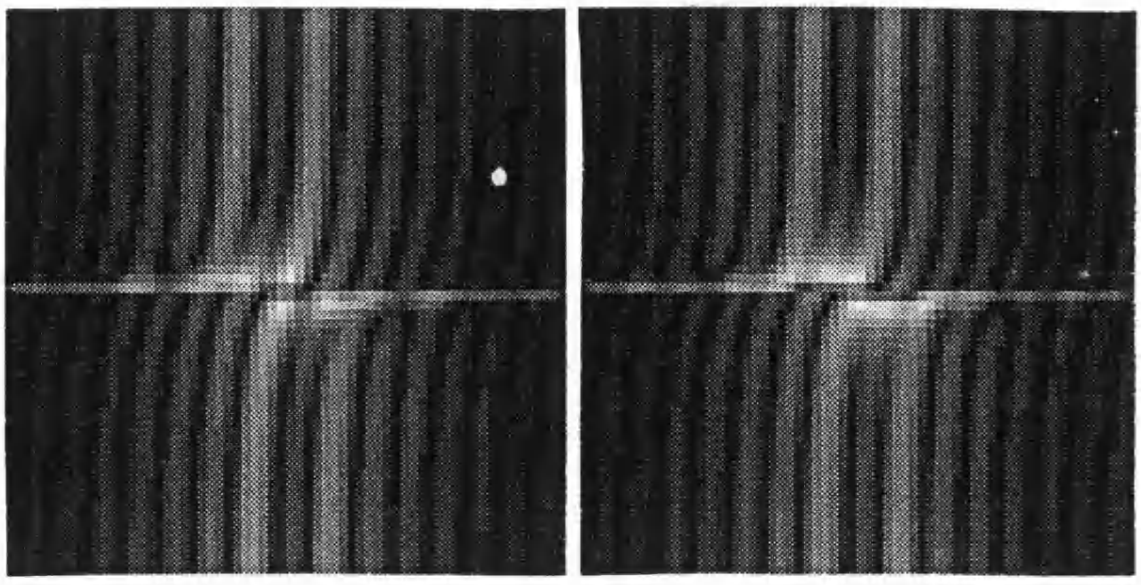

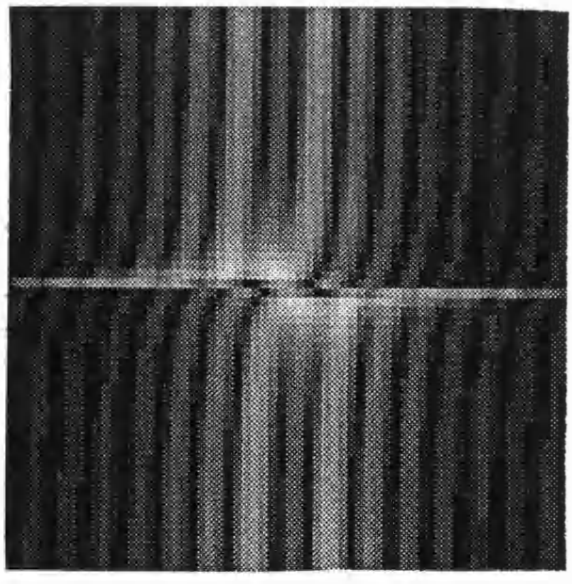

Figures 4.12, 4.13 & 4.14 LACBED pattern for a crystal containing a non-central screw dislocation with $\mathbf{G} \cdot \mathbf{b}/2\pi = 2$. In figure 4.12 (top left) the dislocation is at depth $\theta_0 = 0.25$, in figure 4.13 (top right) $\theta_0 = 0.5$, whilst in figure 4.14 (bottom) $\theta_0 = 0.75$.

This suggests that careful analysis is required when examining the fringe shift of an edge dislocation. This is particularly true close to the Bragg condition where the dynamic fringe following rule does not work so well.

Figures 4.12 to 4.14 show computed diffraction patterns for a non-central screw dislocation located at depths $\theta_0 = 0.25$, 0.5 and 0.75 respectively, and with $\mathbf{G} \cdot \mathbf{b}/2\pi = 2$. All three figures appear much the same as figure 4.6a, the central case, with the same number of fringes, fringe bending and general pattern. However, as the dislocation line is situated further and further away from the centre of the crystal, the figures show a blurring of detail close to the dislocation core. This is because the fringes have less room in which to bend. Thus we should expect away from the extreme cases (very close to the surfaces) that the depth of the dislocation has little influence and the same general diffraction pattern is observed as for a centrally situated dislocation line.

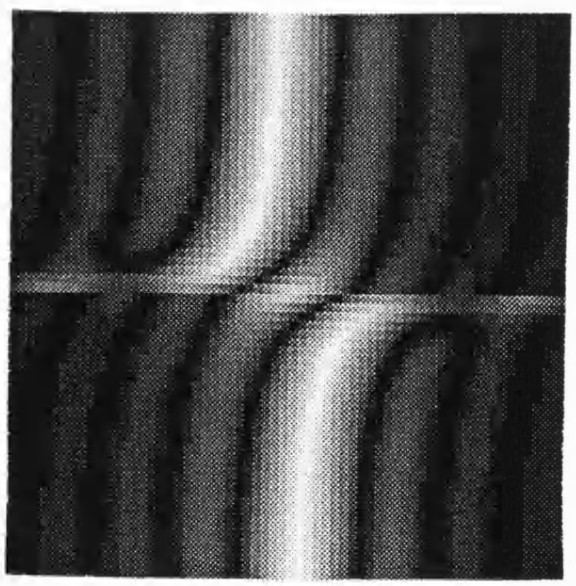

Figure 4.15 LACBED pattern for a crystal containing a central screw dislocation, with $\beta = 1.42$.

As mentioned above, as $\beta$ becomes smaller the influence of the potential weakens and the kinematic approximation becomes increasingly justified. Figure 4.15 shows the computed diffraction pattern for a screw dislocation with $\beta = 1.42$, with other values, ranges and scaling as previously for figure 4.6a. It clearly shows the splitting of the diffraction fringes under kinematic conditions and satisfies the kinematic rule (4.2.1).

Figures 4.16 and 4.17 show the experimental micrographs for diamond with $\mathbf{G} \cdot \mathbf{b}/2\pi = 1$, and for graphite with $\mathbf{G} \cdot \mathbf{b}/2\pi = 2$. Both crystals contain a screw dislocation. The micrographs show a similar form to the computed patterns, having a number of fringes running the length of the pattern, with 2 bright fringes and similar symmetry of pattern. Although they are somewhat blurred in detail, their respective fringe shifts indicate good agreement with the dynamical fringe following rule.

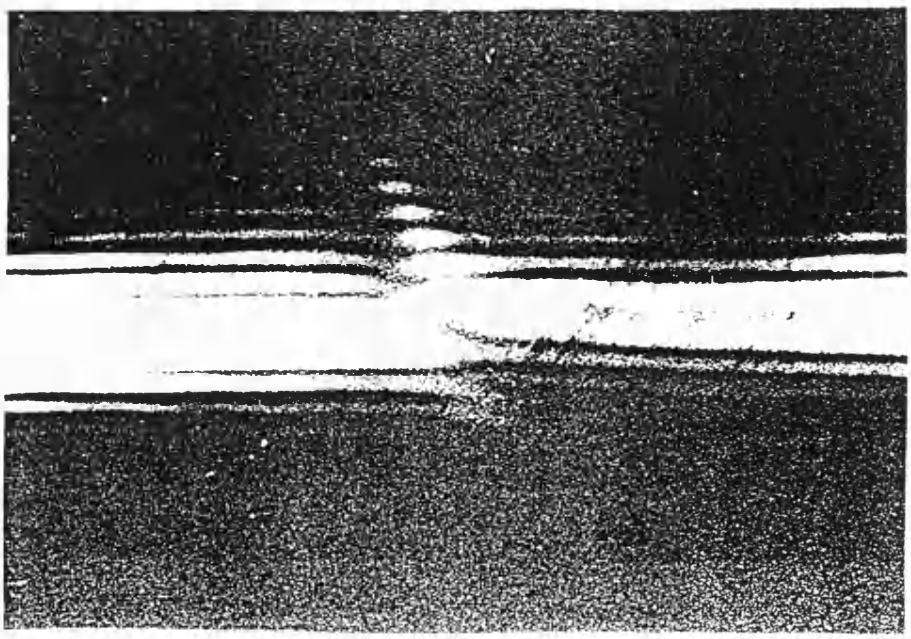

Figure 4.16 Experimental micrograph of a diamond crystal containing a screw dislocation (courtesy of A Preston).

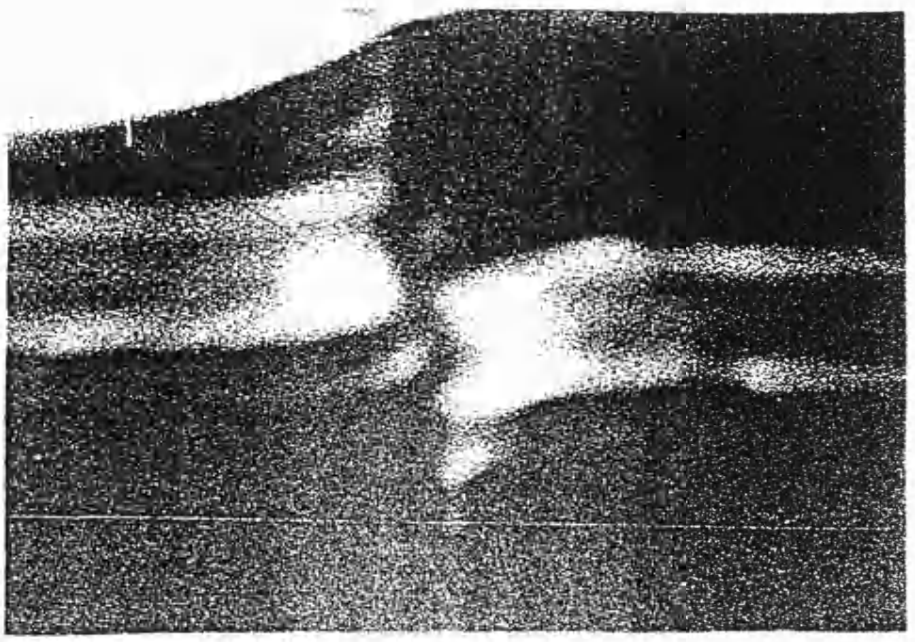

Figure 4.17 Experimental micrograph of a graphite crystal containing a screw dislocation (courtesy of A Preston).

## 4.5 THE ZEROTH ORDER ADIABATIC APPROXIMATION.

In this and the following two sections we shall be concerned with approximating the solutions to the two beam Howie-Whelan equations by using the adiabatic iteration scheme derived in chapter 3. These approximations will then be used to form LACBED patterns, which may then be compared to the exact computational patterns. It is thus hoped to be able to see where the adiabatic approximations are both good and valid, and what improvements further iterations might bring.

To this end we shall here use the first adiabatic iteration to find the lowest order approximate solution to the dimensionless Howie-Whelan equations (4.3.3). From (3.2.40) and (3.2.41) the parallel transported instantaneous eigenstates

(Bloch waves) of (4.3.3) are

$$\begin{pmatrix} C^j_{\mathbf{0}_0} \\ C^j_{\mathbf{G}_0} \end{pmatrix} = \frac{\exp(i\gamma^j_0)}{\sqrt{2}} \begin{pmatrix} \exp(i\phi/2)(1+\frac{x}{2s^j_0})^{1/2} \\ \pm\exp(-i\phi/2)(1-\frac{x}{2s^j_0})^{1/2} \end{pmatrix}, \tag{4.5.1}$$

where for the $\pm$ sign, the $+ve$ sign is for $j = 1$ and the $-ve$ sign for $j = 2$. In conparison with (3.2.42) and (3.2.43) the corresponding eigenvalues of (4.5.1) are

$$s^1_0 = -s^2_0 = \frac{1}{2}\sqrt{x^2+\beta^2}. \tag{4.5.2}$$

and the geometric phase, $\gamma^j_0$, is given by

$$\begin{aligned} \gamma^j_0(\theta) =& \frac{(-1)^j}{2}\frac{x}{\sqrt{x^2+\beta^2}}\int_{-1}^{\theta}\dot{\phi}\,d\theta, \\ =& \frac{(-1)^j}{2}\frac{x}{\sqrt{x^2+\beta^2}}(\phi(\theta)-\phi(-1)) \end{aligned} \tag{4.5.3}$$

where $\phi = \mathbf{G}\cdot\Delta\mathbf{R}$. The geometric phase arises directly from the strain field and is proportional to the change in displacement caused by the strain field in travelling through the crystal. As discussed in chapter 3, we see that if $\phi$ is a constant, the perfect crystal form is recovered and there is no parallel transported phase. Also at the Bragg condition $x = 0$ the eigenstates are naturally parallel transported and $\gamma = 0$.

Substituting (4.5.1), (4.5.2) and (4.5.3) into (3.2.48) gives the diffracted wavefunction at $\theta = 1$ as

$$\psi_{\mathbf{G}_0}(1) = i\frac{\beta\sin(\sqrt{x^2+\beta^2}+\gamma^1_0(1))}{\sqrt{x^2+\beta^2}}\exp(-\frac{i}{2}(\phi(1)-\phi(-1)). \tag{4.5.4}$$

The diffracted intensity at the exit surface $\theta = 1$ is then

$$I_{\mathbf{G}}(1) = \frac{\beta^2\sin^2(\sqrt{x^2+\beta^2}+\gamma^1_0(1))}{x^2+\beta^2}. \tag{4.5.5}$$

The zeroth order approximation for a deformed crystal is the same as the exact solution for the perfect crystal except that the geometric phase has been added

to the dynamical phase. The displacement field $\Delta\mathbf{R}$, and hence the slowness parameter, enters the intensity expression only through the geometric phase and is given via (4.5.3). As discussed in section 3.2, the zeroth approximation assumes that interbranch scattering is small and may be ignored. The zeroth order adiabatic approximation thus assumes that the only effect that a strain field has on the intensity is through changes in the phase of the Bloch waves. From (4.5.3) this change, $\gamma^1(1)$, depends only on the total change of $\Delta\mathbf{R}$ (i.e. $\phi$) in going through the crystal and not on the details of $\Delta\mathbf{R}$.

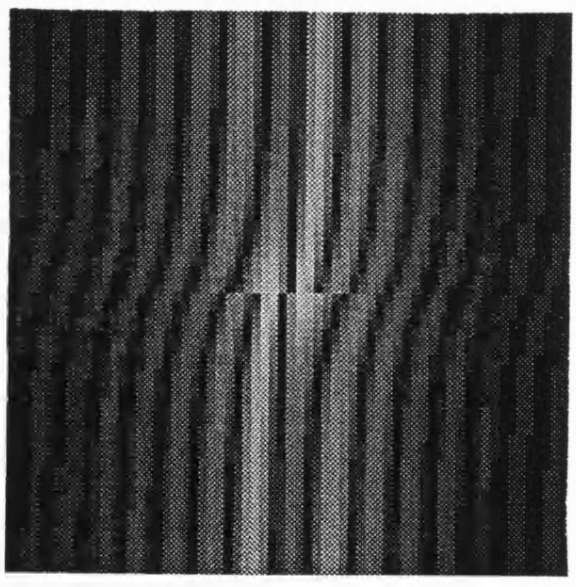

Figure 4.18 Zeroth order adiabatic approximation of a crystal containing a central screw dislocation.

Figure 4.18 shows the LACBED pattern for the diffracted beam, with the intensity given by (4.5.5), for a centrally situated screw dislocation. The same values, ranges and scaling are used as for the exact LACBED pattern, figure 4.6a. As we might expect, in comparing the two figures, 4.6a and 4.18, we can see that

far away from the dislocation line, $y = 0$, they are in good agreement with each other. However the zeroth order adiabatic approximation fails to agree with the exact computational pattern as we approach the dislocation line (in particular near to the Bragg condition, $x = 0$, where there is strong diffraction). This is because close to the dislocation line the strain field is varying so rapidly that the intensity cannot follow the bending of the planes. There is then significant interbranch scattering and in order to form a more realistic approximation we need to include the effects of changes of the relative amplitudes.

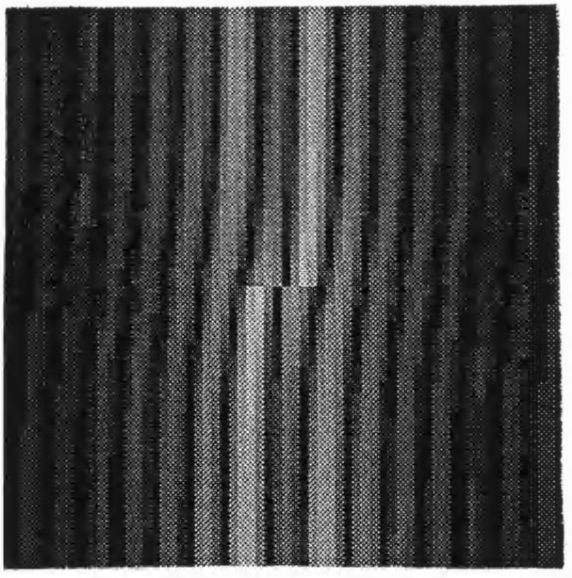

Figure 4.19 Zeroth order adiabatic approximation of a crystal containing a central edge dislocation.

Figure 4.19 shows the LACBED pattern for the diffracted beam, with the intensity given by (4.5.5), for a centrally situated edge dislocation. The same values, ranges and scaling are used as for the exact LACBED pattern, figure

4.9a. Similar results to that for a screw dislocation are found. Far away from the dislocation core the two patterns are in good agreement, but increasingly differ as it is approached.

Figure 4.20 shows the LACBED pattern for the diffracted beam, with the intensity given by (4.5.5), for a noncentrally situated screw dislocation, with $\theta_0 = 0.5$. It shows no real change from that of the central case, figure 4.18. This is because the effect of the strain is to change the argument of the sine in (4.5.5) only by a small amount. The zeroth order approximation is relatively insensitive to the depth of the dislocation line.

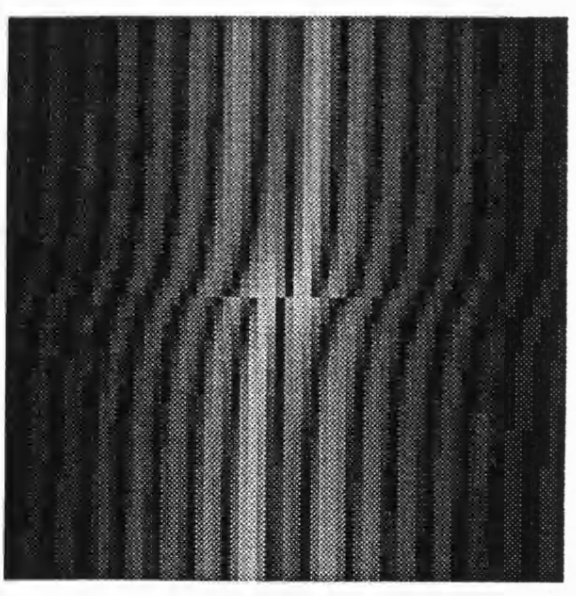

Figure 4.20 Zeroth order adiabatic approximation of a crystal containing a non-central screw dislocation, with $\theta_0 = 0.5$.

From equation (3.2.49) with $z_0 = \frac{1}{2}x$, $r_0 = \frac{1}{2}\beta$ and $\varphi = \phi$ we should expect

(4.5.5) to be a good approximation whenever

$$\left| \frac{\beta}{2(x^2+\beta^2)^{1/2}} \int_{-1}^{1} \dot{\phi} \exp(-2i\gamma_0^1 - i\sqrt{x^2+\beta^2}\ \theta)\ d\theta \right| \ll 1. \qquad (4.5.6)$$

From (4.5.6) we see that, away from the Bragg condition $x = 0$, as $\beta$ becomes smaller the approximation becomes better, that is a weak potential has a smaller influence on diffraction than a strong one. Also as $x$ becomes large the approximation gets better, as observed in figures 4.18 to 4.20

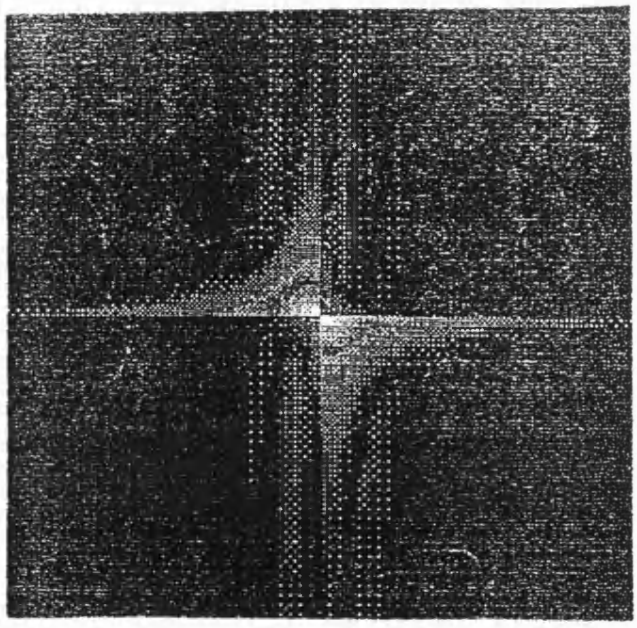

Figure 4.21 Map of the dropped (first order and higher) off-diagonal terms for a crystal containing a central screw dislocation.

The corresponding map of (4.5.6) for a centrally situated screw dislocation with $\mathbf{G} \cdot \mathbf{b}/2\pi = 2$ is shown in figure 4.21. The same values and ranges are used as in previous patterns, but the scaling factor is now 2.571, with the largest value (the greatest error) show most bright. It confirms the results that the approximation is good away from the exact Bragg condition and the dislocation line, and becomes increasingly worse as we approach either.

## 4.6 THE FIRST ORDER ADIABATIC APPROXIMATION.

As discussed in sections 2.7 and 3.3 modified Bloch wave theory is expected to give a better approximation than the unmodified case (Bird and Preston 1988). In this section we shall use adiabatic iteration and modified Bloch wave theory to try to form a better approximation to the Howie-Whelan equations for a deformed crystal.

By using the substitutions (4.3.1), the modified Howie-Whelan equations (2.7.9) may be written as

$$\frac{1}{2}\begin{pmatrix} x-\dot{\phi} & \beta \\ \beta & -x+\dot{\phi} \end{pmatrix}\begin{pmatrix} \tilde{\psi}_0 \\ \tilde{\psi}_G \end{pmatrix} = -i\frac{d}{d\theta}\begin{pmatrix} \tilde{\psi}_0 \\ \tilde{\psi}_G \end{pmatrix}. \tag{4.6.1}$$

The boundary conditions at $\theta = -1$ are now

$$\begin{aligned} \tilde{\psi}_0(-1) &= \exp(-i\phi(-1)/2) \\ \tilde{\psi}_G(-1) &= 0. \end{aligned} \tag{4.6.2}$$

Although this is not an adiabatic iteration, the only variable, $\theta$, now enters in the form $\dot{\phi}$, and we should expect upon using the first adiabatic iteration, the errors will now be of order $\ddot{\phi}$.

Proceeding as in chapter 3, from (3.2.41) the instantaneous parallel transported eigenstates of (4.6.1) are

$$\begin{pmatrix} \tilde{C}^j_{0_0} \\ \tilde{C}^j_{G_0} \end{pmatrix} = \frac{1}{\sqrt{2}}\begin{pmatrix} (1+\frac{(x-\dot{\phi})}{2\tilde{s}^j_0})^{1/2} \\ \pm(1-\frac{(x-\dot{\phi})}{2\tilde{s}^j_0})^{1/2} \end{pmatrix}, \tag{4.6.3}$$

where again the $+ve$ sign refers to $j = 1$, and the $-ve$ sign to $j = 2$. The corresponding eigenvalues, given by (3.2.42), are

$$\tilde{s}^1_0 = -\tilde{s}^2_0 = \frac{1}{2}\sqrt{(x-\dot{\phi})^2+\beta^2}. \tag{4.6.4}$$

As discussed in chapter 3, because the Hamiltonian is real, there is no geometric phase, $\tilde{\gamma}_0^j = 0$. Thus the phase is now entirely dynamical. In the first order adiabatic approximation, (3.2.48), the diffracted amplitude at $\theta = 1$ is

$$\tilde{\psi}_{\mathbf{G}_0}(1) = \frac{1}{2}\exp(i\int_{-1}^{1}\tilde{s}_0^1\,d\theta)\left(1-\frac{x-\dot{\phi}(1)}{2\tilde{s}_0^1(1)}\right)^{\frac{1}{2}}\left(1+\frac{x-\dot{\phi}(-1)}{2\tilde{s}_0^1(-1)}\right)^{\frac{1}{2}} - \frac{1}{2}\exp(i\int_{-1}^{1}\tilde{s}_0^2\,d\theta)\left(1-\frac{x-\dot{\phi}(1)}{2\tilde{s}_0^2(1)}\right)^{\frac{1}{2}}\left(1+\frac{x-\dot{\phi}(-1)}{2\tilde{s}_0^2(-1)}\right)^{\frac{1}{2}}. \tag{4.6.5}$$

The diffracted intensity at $\theta = 1$ is then

$$I_{\mathbf{G}}(1) = \frac{1}{2}\left(1-\frac{(x-\dot{\phi}(1))(x-\dot{\phi}(-1))+\beta^2\cos(2\int_{-1}^{1}\tilde{s}_0^1\,d\theta)}{4\tilde{s}_0^1(1)\tilde{s}_0^1(-1)}\right). \tag{4.6.6a}$$

From (4.6.6a) the modified diffracted intensity for a crystal containing a symmetric displacement field $\left(\dot{\phi}(\theta)=\dot{\phi}(-\theta)\right)$ is

$$I_{\mathbf{G}}(1) = \frac{\beta^2\sin^2(\frac{1}{2}\int_{-1}^{1}\sqrt{(x-\dot{\phi})^2+\beta^2}\,d\theta)}{(x-\dot{\phi})^2+\beta^2}. \tag{4.6.6b}$$

Expanding the sine argument in (4.6.6b) gives

$$\begin{aligned}\int_{-1}^{1}\tilde{s}_0^1\,d\theta &= \frac{1}{2}\sqrt{x^2+\beta^2}\int_{-1}^{1}d\theta\,\left(1-\frac{2x\dot{\phi}-\dot{\phi}^2}{x^2+\beta^2}\right)^{\frac{1}{2}}\\ &= \sqrt{x^2+\beta^2}-\frac{x}{2\sqrt{x^2+\beta^2}}\int_{-1}^{1}\dot{\phi}\,d\theta+O(\dot{\phi}^2)+\cdots\end{aligned}$$

which to lowest order is the sine argument for the zeroth order adiabatic approximation (4.5.5). Thus where the rate of change of displacement, $\Delta\dot{\mathbf{R}}$, (and so $\dot{\phi}$) is small and slowly varying it is expected that the two approximations should agree with each other. In contrast when it becomes large then the effects of $\dot{\phi}$ become important, we see that the strain field introduces both a change in the phase and in the amplitude. Physically this is due to the strain field modifying the deviation from the Bragg condition. The first order aproximation

includes the first order effects of interbranch scattering, which are caused by the bending of the lattice planes. As discussed in section 3.3 the displacement field now enters (4.6.6a,b) in the form $\Delta\dot{\mathbf{R}}$, and so errors will be of order $\Delta\ddot{\mathbf{R}}$; i.e. the curvature.

Figure 4.22 shows the LACBED pattern for a centrally situated screw dislocation where the intensity is approximated by (4.6.6b). The same values, ranges and scaling is used as for figure 4.6a. Far away from the dislocation line, where $\dot{\phi}$ is small the first order approximation, figure 4.22, appears to be identical to the zeroth order solution, figure 4.18. However as we approach the dislocation line the modified approximation shows a significant improvement over the zeroth order approximation when compared to the exact computational solution, figure 4.6a.

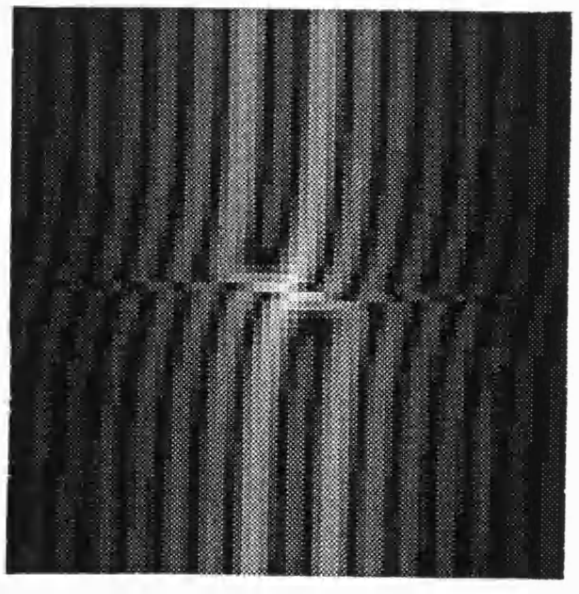

Figure 4.22 First order adiabatic approximation of a LACBED pattern of a crystal containing a central screw dislocation.

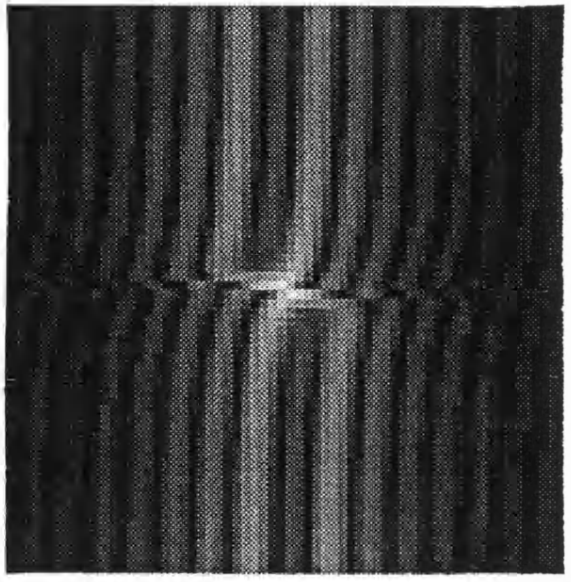

Figure 4.23 First order adiabatic approximation of a LACBED pattern of a crystal containing a screw dislocation at depth $\theta_0 = 0.5$.

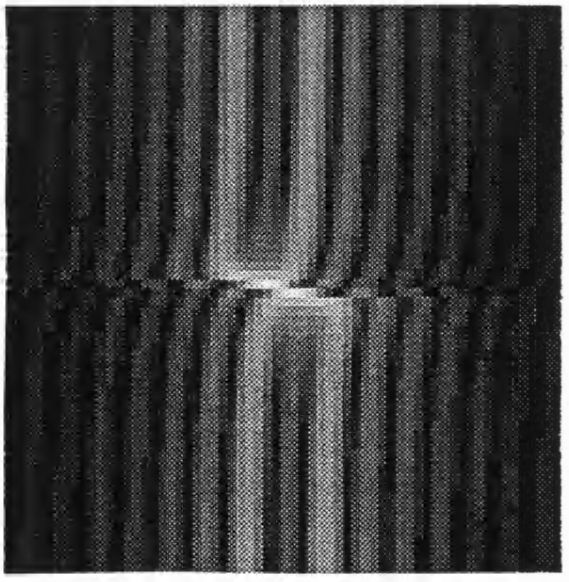

Figure 4.24 First order adiabatic approximation of a LACBED pattern of a crystal containing a screw dislocation at depth $\theta_0 = 0.75$.

Using equation (4.4.6a) figures 4.23 and 4.24 show the LACBED pattern for a screw dislocation which is at depths $\theta = 0.5$ and 0.75 respectively. Although the patterns show a slight blurring of detail at the dislocation core (not as great as for the exact solutions but more than the zeroth order), essentially the patterns are the same as that for a central dislocation and show little dependence upon depth.

From (3.2.49), with $z_0 = \frac{1}{2}(x - \dot{\phi})$, $r_0 = \frac{1}{2}\beta$ and $\varphi = 0$, the modified adiabatic approximation is expected to be a good approximation whenever

$$\left| \frac{\beta}{2} \int_{-1}^{1} \frac{\ddot{\phi} \exp(i \int_{-1}^{\theta} \sqrt{(x - \dot{\phi})^2 + \beta^2}\, d\theta')\, d\theta}{(x - \dot{\phi})^2 + \beta^2} \right| \ll 1. \qquad (4.6.7)$$

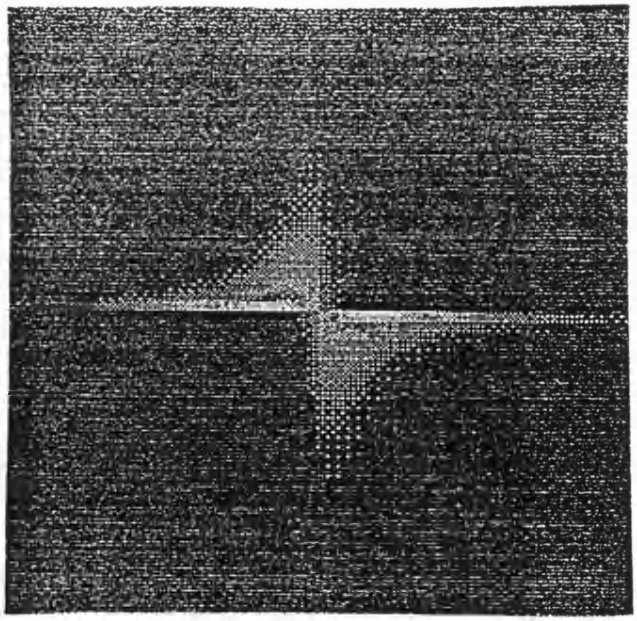

Figure 4.25 Map of the dropped (second order and higher) off-diagonal terms for a crystal containing a central screw dislocation.

Figure 4.25 shows the corresponding map for figure 4.21 of the dropped off-diagonal terms. The same values, ranges and scaling is used as for figure 4.21.

In comparison, the dropped off-diagonal terms for the modified solution are significant only very close to the dislocation line itself. If we compare the two expressions for the dropped terms, equations (4.5.6) and (4.6.7), we see that in the unmodified case they are proportional to $\dot{\phi}$, whilst for the modified case they are now proportional to $\ddot{\phi}$. In the case of a screw dislocation this becomes proportional to $1/y$, and $(1/y)^2$ respectively. In other words the first order approximation is better than the zeroth order approximation by a factor $1/y$, which is simply the adiabatic slowness parameter of chapter 3.

## 4.7 THE SECOND ORDER ADIABATIC APPROXIMATION.

We have seen in the previous section that the modified first order iteration approximation has resulted in significant improvement. We may now ask will further iterations also produce such improvements. In other words, *will further iterations produce enough improvement over the first order iteration, to justify the work in making them ?* In order to answer this question we shall look at the next iteration. As was discussed in section 3.2, a better approximation to the dimensionless Howie-Whelan equations may be formed by including the dropped off-diagonal term. This is done by transforming to a new state. From (3.2.8a) the elements of the new state are

$$\tilde{\psi}_{j_1} = \sum_l \tilde{C}^{l^*}_{j_0} \tilde{\psi}_{l_0} \tag{4.7.1}$$

From (3.2.45), (3.2.46), (4.6.1) and (4.6.4) the Hamiltonian of the new state is then

$$\tilde{H}_1 = \frac{1}{2} \begin{pmatrix} \sqrt{(x-\dot{\phi})^2+\beta^2} & \frac{-i\beta\ddot{\phi}}{(x-\dot{\phi})^2+\beta^2} \\ \frac{i\beta\ddot{\phi}}{(x-\dot{\phi})^2+\beta^2} & -\sqrt{(x-\dot{\phi})^2+\beta^2} \end{pmatrix}. \tag{4.7.2}$$

As expected (4.7.2) shows that the on-diagonal terms of the new Hamiltonian $H_1$ are equal to the first order eigenstates $\tilde{s}_0^j$ and hence proportional to $\dot{\phi}$, while the off-diagonal terms of $\tilde{H}_1$ are of order $\ddot{\phi}$. As discussed in section 3.2.2, where $\ddot{\phi}$ changes sign with depth we shall write $i\ddot{\phi} = |\ddot{\phi}| \exp(i\pi W)$, where $W$ is the appropriate step function. With this choice we need only approximate one solution, not two (i.e. $\pm\ddot{\phi}$). This allows a general approximation to be formed (thus both echoing and allowing comparison with previous work). In this thesis the only type of strain field we shall be concerned with is that due to a dislocation. For a screw dislocation, with $\Delta\mathbf{R}$ given by (2.8.1) and the dislocation at depth $\theta_0$, $W$ is given by

$$W(\theta) = \begin{cases} -\frac{1}{2} & \theta < \theta_0 \\ \frac{1}{2} & \theta > \theta_0. \end{cases} \tag{4.7.3}$$

For cases where $\ddot{\phi}$ does not change sign, then $W$ is constant and equal to $\pm 1/2$ (dependent upon initial sign of $\ddot{\phi}$).

The parallel transported instantaneous eigenstates of $\tilde{H}_1$ are from (3.2.41) then given by

$$\begin{pmatrix} \tilde{C}^j_{0_1} \\ \tilde{C}^j_{G_1} \end{pmatrix} = \frac{\exp(i\tilde{\gamma}_1^j)}{\sqrt{2}} \begin{pmatrix} \exp(\frac{i\pi}{2}W)\left(1 + \frac{\sqrt{(x-\dot{\phi})^2+\beta^2}}{2\tilde{s}_1^j}\right)^{\frac{1}{2}} \\ \pm\exp(-\frac{i\pi}{2}W)\left(1 - \frac{\sqrt{(x-\dot{\phi})^2+\beta^2}}{2\tilde{s}_1^j}\right)^{\frac{1}{2}} \end{pmatrix}. \tag{4.7.4}$$

From (3.2.42) the respective eigenvalues of (4.7.2) are

$$\tilde{s}_1^1 = -\tilde{s}_1^2 = \frac{1}{2}\frac{\sqrt{[(x-\dot{\phi})^2+\beta^2]^3 + \beta^2\ddot{\phi}^2}}{(x-\dot{\phi})^2+\beta^2}. \tag{4.7.5}$$

As in the last section we may rewrite the eigenvalues as

$$\tilde{s}_1^1 = -\tilde{s}_1^2 = \frac{1}{2}\sqrt{(x-\dot{\phi})^2+\beta^2}\left(1 + \frac{\beta^2\ddot{\phi}^2}{[(x-\dot{\phi})^2+\beta^2]^3}\right)^{\frac{1}{2}}$$

$$\simeq \frac{1}{2}\sqrt{(x-\dot{\phi})^2+\beta^2} + \frac{\beta^2\ddot{\phi}^2}{4[(x-\dot{\phi})^2+\beta^2]^{\frac{5}{2}}} \tag{4.7.5a}$$

Now in the second order adiabatic approximation we shall be ignoring third order and higher terms. Hence if we ignore the second term in (4.7.5a) we return to the initial eigenvalue $\tilde{s}_0^j$. Substituting (4.7.5a) into (4.7.4) and ignoring all third order and higher terms, the eigenstates can be rewriten as

$$\begin{pmatrix} \tilde{C}^1_{\mathbf{0}_1} \\ \\ \tilde{C}^1_{\mathbf{G}_1} \end{pmatrix} = \exp(i\tilde{\gamma}_1^1) \begin{pmatrix} \exp(\frac{i\pi}{2}W) \\ \\ \frac{\beta|\ddot{\phi}|\exp(-\frac{i\pi}{2}W)}{2[(x-\dot{\phi})^2+\beta^2]^{\frac{3}{2}}} \end{pmatrix} \tag{4.7.6a}$$

and

$$\begin{pmatrix} \tilde{C}^2_{\mathbf{0}_1} \\ \\ \tilde{C}^2_{\mathbf{G}_1} \end{pmatrix} = \exp(i\tilde{\gamma}_1^2) \begin{pmatrix} \frac{\beta|\ddot{\phi}|\exp(\frac{i\pi}{2}W)}{2[(x-\dot{\phi})^2+\beta^2]^{\frac{3}{2}}} \\ \\ -\exp(-\frac{i\pi}{2}W) \end{pmatrix}. \tag{4.7.6b}$$

From (3.2.43) the geometric phase is

$$\tilde{\gamma}_1^j(\theta) = -\frac{\pi}{2}\int_{-1}^{\theta} \frac{\frac{1}{2}\sqrt{(x-\dot{\phi})^2+\beta^2}}{\tilde{s}_1^j}\delta(\theta-\theta_0)\,d\theta. \tag{4.7.7a}$$

If $W$ is constant, the $\delta$ function is always zero and there will be no geometric phase, i.e. $\gamma = 0$ unless $\ddot{\phi}$ changes sign. For a screw dislocation $\ddot{\phi}(\theta_0) = 0$ and so from (4.7.5) and (4.7.7a) its geometric phase is

$$\tilde{\gamma}_1^j(\theta) = \begin{cases} 0 & \theta < \theta_0. \\ (-1)^j\frac{\pi}{2} & \theta > \theta_0. \end{cases} \tag{4.7.7b}$$

Equation (4.7.7b) implies that before the dislocation there is no geometric phase, whilst after it is crossed the geometric phase is constant and equal to $\pm\pi/2$ (i.e. it simply changes the instantaneous eigenstates by a factor $\pm i$). Thus as in section 4.4 the dislocation again gives rise directly to the geometric phase.

From (3.2.36) and (3.2.37) the second order adiabatic approximation gives the wavefunction at $\theta = 1$ as

$$\tilde{\psi}_{\mathbf{G}_0}(1) = \sum_j \tilde{C}^j_{\mathbf{G}_0}(1)\sum_{j'}\tilde{C}^{j'}_{j_1}(1)\exp(i\int_{-1}^{1}\tilde{s}_1^{j'}\,d\theta)\sum_k \tilde{C}^{j'^*}_{k_1}(-1)$$
$$\sum_{k'}\tilde{C}^{k^*}_{k'_0}(-1)\tilde{\psi}_{k'_0}(-1). \tag{4.7.8}$$

The diffracted intensity at the bottom surface can then be written as

$$I_{\mathrm{G}}(1) = \left| \chi\omega \exp(i \int_{-1}^{1} s_1^1 \, d\theta) - \eta\mu \exp(i \int_{-1}^{1} s_1^2 \, d\theta) \right|^2 , \qquad (4.7.9a)$$

where

$$\begin{aligned} \chi =& \tilde{C}^1_{G_0}(1)\tilde{C}^1_{0_1}(1) + \tilde{C}^2_{G_0}(1)\tilde{C}^1_{G_1}(1) \\ \omega =& C^{1^*}_{0_1}(-1)\tilde{C}^{1^*}_{0_0}(-1) + \tilde{C}^{1^*}_{G_1}(-1)\tilde{C}^{2_*}_{0_0}(-1) \\ \eta =& \tilde{C}^1_{G_0}(1)\tilde{C}^2_{0_1}(1) + \tilde{C}^2_{G_0}(1)\tilde{C}^2_{G_1}(1) \\ \mu =& \tilde{C}^{2^*}_{0_1}(-1)\tilde{C}^{1^*}_{0_0}(-1) + \tilde{C}^{2^*}_{G_1}(-1)\tilde{C}^{2^*}_{0_0}(-1). \end{aligned} \qquad (4.7.9b)$$

Equation (4.7.9) may be significantly simplified if we look at the symmetric case, in which $\dot{\phi}(\theta) = \dot{\phi}(-\theta)$. Then, as shown in appendix C, (4.7.9) reduces to

$$I_{\mathrm{G}}(1) = \frac{\beta^2 \sin^2(\int_{-1}^{1} \tilde{s}_0^1 \, d\theta)}{(x - \dot{\phi})^2 + \beta^2} + \frac{2\beta^2 x |\ddot{\phi}| \sin(\int_{-1}^{1} \tilde{s}_0^1 \, d\theta) \cos(\int_{-1}^{1} \tilde{s}_0^1 \, d\theta)}{((x - \dot{\phi})^2 + \beta^2)^4}. \qquad (4.7.10)$$

In making the second order adiabatic approximation we have ignored all third order and higher terms on the off-diagonals and so (4.7.10) is accurate to second order terms. Comparing equations (4.7.10) and (4.6.6b) we see that if we ignore $\ddot{\phi}$ then they are identical to one another. They thus agree to first order. The effect of the second order terms in (4.7.10) is to cause a small change.

Figure 4.26 shows the LACBED pattern for a centrally located screw dislocation with the intensity given by (4.7.10). The values, ranges and scaling are as used previously, figures 4.6a, 4.18 and 4.22. Comparing the patterns for the second order approximation, figure 4.26, and the first order approximation, figure 4.22, with the computed pattern, figure 4.6a, we can see that the second order approximation only produces any improvement over the first order approximation very close to the dislocation core. In comparison to the significant improvement that the first order approximation made over the zeroth order approximation (figure 4.18), there appears to be little improvement.

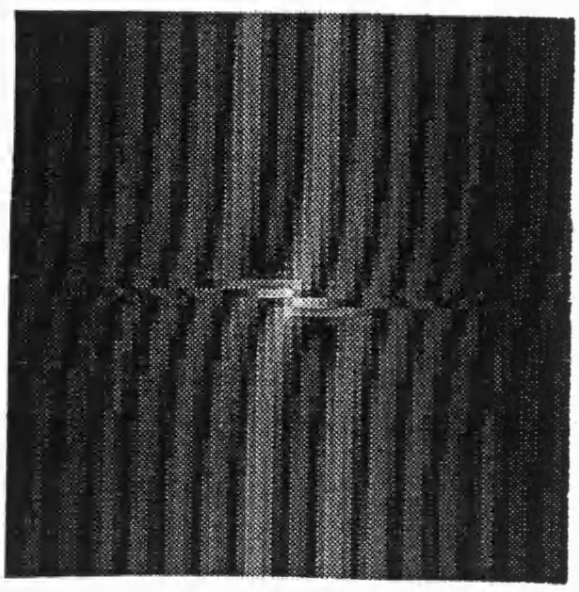

Figure 4.26 Second order adiabatic approximation of a LACBED pattern of a crystal containing a central screw dislocation.

Figure 4.27 and 4.28 show blown up regions of figures 4.22 and 4.26. The ranges are now $-1 < y < 1$ and $-6.25 < x < 6.25$. The two figures are still amost identical to each other and imply that further iteration will not produce enough significant improvement to justify the work in making them.

From (3.2.46) with $z_0 = \frac{1}{2}\sqrt{(x-\dot{\phi})^2+\beta^2}$, $r_0 = \frac{1}{2}\frac{\beta|\ddot{\phi}|}{(x-\dot{\phi})^2+\beta^2}$ and $\varphi = \pi W$ (where $W$ is given through (4.7.3)) the off-diagonal terms are

$$\sum_G \tilde{C}^{2^*}_{G_1}\dot{\tilde{C}}^{1}_{G_1} = \frac{\beta}{2}\frac{\sqrt{(x-\dot{\phi})^2+\beta^2}\left(3\ddot{\phi}^2(x-\dot{\phi})+\dddot{\phi}((x-\dot{\phi})^2+\beta^2)\right)}{[(x-\dot{\phi})^2+\beta^2]^3+\beta^2\ddot{\phi}^2}\exp(-2i\tilde{\gamma}^1_1). \tag{4.7.11}$$

Using (3.2.49) and (4.7.11), to lowest order it is expected that (4.7.10) will be a

good approximation whenever

$$\left|\frac{\beta}{2}\int_{-1}^{1}\frac{\dddot{\phi}}{[(x-\dot{\phi})^2+\beta^2]^{\frac{3}{2}}}\exp(-2i\tilde{\gamma}_1^1(\theta)-i\int_{-1}^{\theta}\sqrt{(x-\dot{\phi})^2+\beta^2}d\theta')\,d\theta\right|\ll 1. \tag{4.7.12}$$

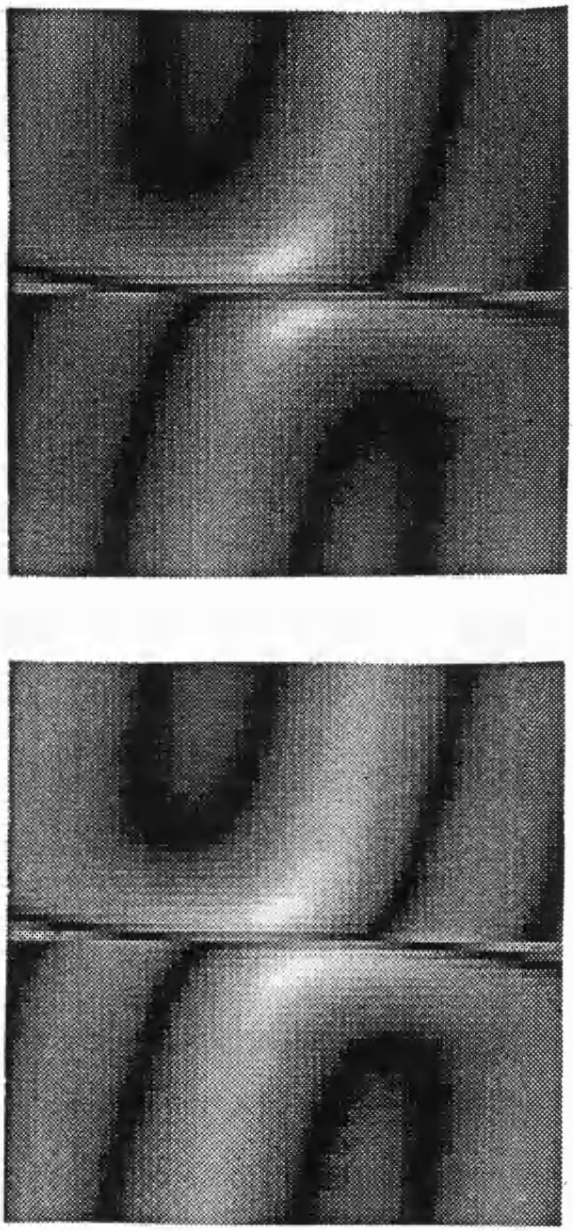

Figure 4.27 (top) shows an enlarged picture of the first order approximation, figure 4.22. Figure 4.28 (bottom) shows an enlarged picture of the second order approximation, figure 4.26. The ranges for both figures are $-1 < y < 1$ and $-6.25 < x < 6.25$.

From (4.7.12) we can see that as expected the error in making the adiabatic approximation is of third order ($\dddot{\phi}$) or higher, thus the error is now proportional to $\Delta\ddot{\mathbf{R}}$ and should be better than the previous approximation. We are thus including factor proportional to $\Delta\ddot{\mathbf{R}}$,which were previously ignored. Using (4.7.12) figure 4.29 shows the corresponding map of the error for a screw dislocation. The same values, ranges and scaling are used as for the zeroth order and the first order maps of the dropped off-diagonal terms, figures 4.21 and 4.25. Comparing the two figures we can see that they appears to be significant improvement only very close to the dislocation line.

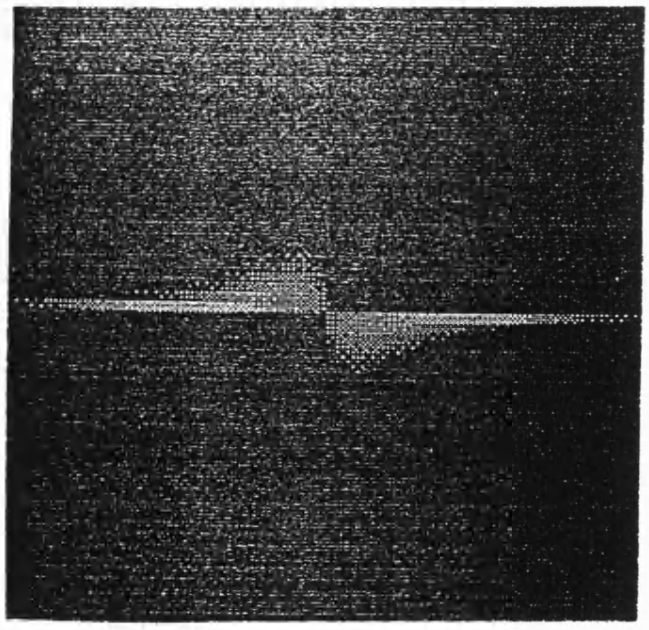

Figure 4.29 Map of the dropped (third order and higher) off-diagonal terms for a crystal containing a central screw dislocation.

**Summary**

Thus far in this chapter we have shown that adiabatic iteration may be used to approximate the exact solution to the 2-beam Howie–Whelan equations and in particular to form LACBED patterns of deformed crystals. Although the exact (to within some negligble error) solution to the general 2-beam equations for a deformed crystal may be made using computers, an exact analytical solution is only possible for perfect crystals. In order to have an analytical expression for the the case of deformed crystals approximation techniques must be used.

We have seen that the zeroth order adiabatic iteration to the 2-beam unmodified Howie–Whelan equations is extremely good far away from any strain field core. HEED provides a clear demonstration of the geometric phase through the bending of fringes in electron diffraction patterns. Later in section 4.10 we shall demonstrate how this simple interpretation for determining $\mathbf{b}$ in terms of the geometric phase may be used to explain the fringe following rule. By use of the modified Bloch wave theory together with adiabatic iteration, significant improvements over the unmodified case were made. These were made at little extra mathematical cost.

A further iteration, however, greatly increased the necessary algebra without, for a screw dislocation, producing any significant improvement. These results suggest there is little advantage to be gained by making a large number of iterations. This is due to the rapidly increasing complexity of mathematics involved and its difficulty in interpretation, and because each successive iteration is expected to produce smaller improvements over its predecessor.

As further iterations do not justify the work in making them, we shall in the

remainder of this thesis make use of the first order adiabatic approximation. In section 4.8 and 4.9 the modified result will be used to examine the affects of a tilted strain field and of absorption upon 2-beam LACBED patterns, whilst in section 4.10 we shall make use of the unmodified result.

## 4.8 ADIABATIC ITERATION APPROXIMATION FOR A SLOPED DISLOCATION.

We now look at the case where the dislocation line is not in the same plane as the reciprocal lattice vector **G**, but rather slopes. As shown in figure 4.30 the dislocation line cuts the top surface of the crystal at $T$ and the bottom surface at $B$. The angle made by the dislocation line and the bottom surface is given by

$$\vartheta = \arctan(\frac{t}{T-B}). \tag{4.8.1}$$

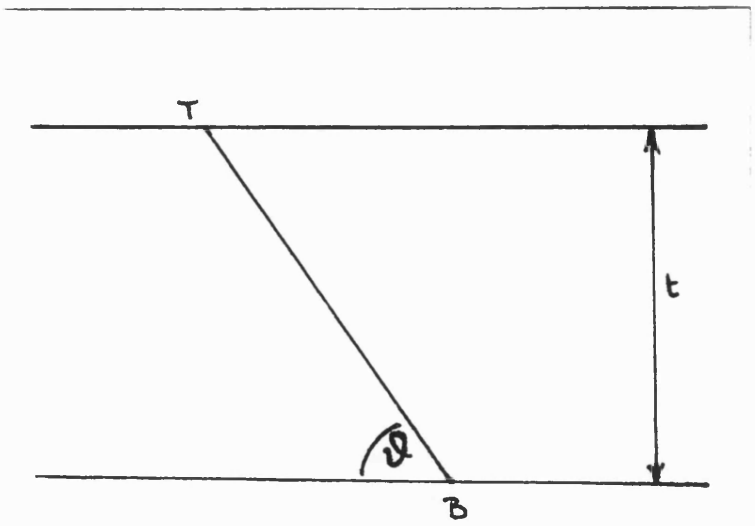


Figure 4.30 Geometry of a crystal containing a tilted dislocation.

We shall assume that the displacement at a point **r** in the crystal is a function of the perpendicular distance from the dislocation line, extended outside the crystal if necessary, to the point **r** (see figure 4.30). The perpendicular distance $R$ is

$$R = \left[ y^2 + \left( (x - \frac{T+B}{2}) \sin\vartheta - z\cos\vartheta \right)^2 \right]^{1/2}. \qquad (4.8.2)$$

As before the $x$ axis is defined to be in the same direction as the reciprocal lattice vector **G**. The $y$ axis is defined to lie perpendicular to the $x$-axis, where again the line $y = 0$ is defined to be along the line of the dislocation.

In this particular case the modified Howie-Whelan equations may again be written as

$$\frac{1}{2}\begin{pmatrix} W - k\mathbf{G}\cdot\Delta\dot{\mathbf{R}} & \tilde{U} \\ \tilde{U} & -W + k\mathbf{G}\cdot\Delta\dot{\mathbf{R}} \end{pmatrix}\begin{pmatrix} \psi_{\mathbf{0}} \\ \psi_{\mathbf{G}} \end{pmatrix} = -2ik\frac{d}{dz}\begin{pmatrix} \psi_{\mathbf{0}} \\ \psi_{\mathbf{G}} \end{pmatrix}. \qquad (4.8.3)$$

The difference is that the dislocation line is not infinite in extent. A second difference is that the displacement is now a function of $x$, $y$ and $z$. Previously it was only a function of $y$ and $z$. Because of this we need to define a scale between $W$, the parameter which describes the small deviation away from the Bragg condition at which significant diffraction occurs, and the length of the dislocation line (see figure 4.31). In order to include this we shall multiply $W$ by a dimensionless scaling factor $\lambda$. In effect $\lambda$ is a measure of the number of fringes which cross the finite dislocation. As was done previously in section 4.3 we now make the equations dimensionless, by using the substitutions (4.3.1) and (4.3.2). Equation (4.8.3) becomes

$$\frac{1}{2}\begin{pmatrix} \lambda x - \dot{\phi} & \beta \\ \beta & -\lambda x + \dot{\phi} \end{pmatrix}\begin{pmatrix} \psi_{\mathbf{0}} \\ \psi_{\mathbf{G}} \end{pmatrix} = -i\frac{d}{d\theta}\begin{pmatrix} \psi_{\mathbf{0}} \\ \psi_{\mathbf{G}} \end{pmatrix}. \qquad (4.8.4)$$

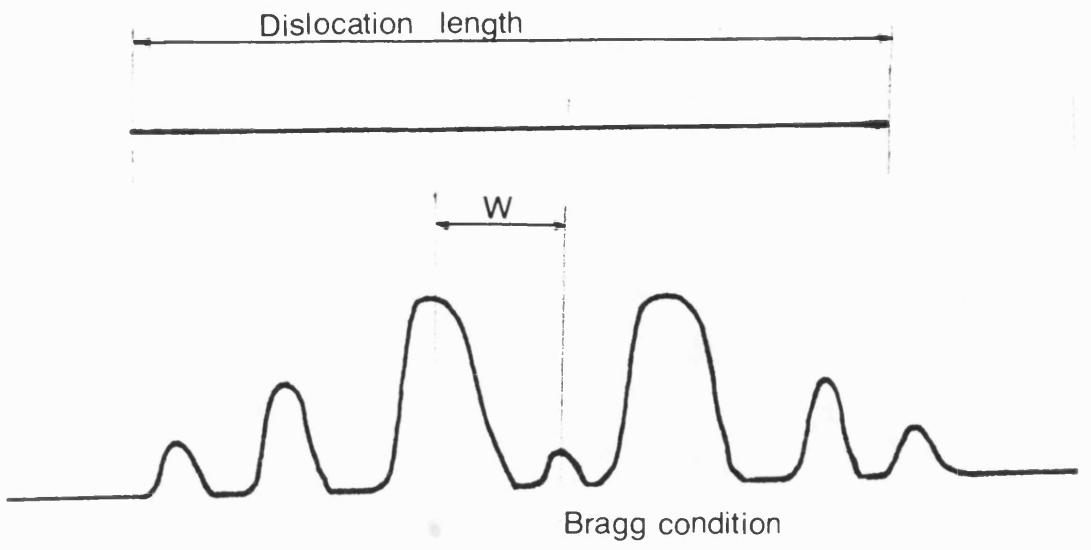


Figure 4.31 Scaling parameter $W$: which describes the deviation away from the Bragg condition at which significant diffraction occurs, relative to the dislocation line length.

The solution to (4.8.4) may again be approximated by using the adiabatic technique developed in chapter 3. Similar to the derivation in section 4.5, the first order diffracted intensity at the bottom surface is

$$I_{\mathbf{G}}(1) = \frac{1}{2}\left(1 - \frac{(\lambda x - \dot{\phi}(1))(\lambda x - \dot{\phi}(-1)) + \beta^2 \cos(2\int_{-1}^{1} \tilde{s}_0^1 \, d\theta)}{4\tilde{s}_0^1(1)\tilde{s}_0^1(-1)}\right), \qquad (4.8.5)$$

where

$$\tilde{s}_0^1(\theta) = \frac{1}{2}\sqrt{(\lambda x - \dot{\phi}(\theta))^2 + \beta^2}. \qquad (4.8.6)$$

Figures 4.32 to 4.37 shows the LACBED pattern for a sloped screw dislocation. Figures *a* are the exact computed patterns and figures *b* the first order modified approximations, with the diffracted intensity given by (4.8.5). The same values,

ranges and scaling is used as for previous patterns. In all of the different cases the dynamical fringe following rule is obeyed and the total number of fringes is conserved. For a sloped screw dislocation, the displacement in the **R** plane is given by

$$\Delta \mathbf{R} = \frac{\mathbf{b}}{2\pi} \arctan\left(\frac{(R^2 - y^2)^{\frac{1}{2}}}{y}\right). \tag{4.8.7}$$

Figures 4.32*a* and *b* are taken with the values $\lambda = 1$, $T = 40$ and $B = -40$. Both figures as expected show identical results to those from respective previous patterns, figures 4.6a and 4.22. The two figures are almost identical to those of the unsloped patterns differing only very close to the dislocation line itself.

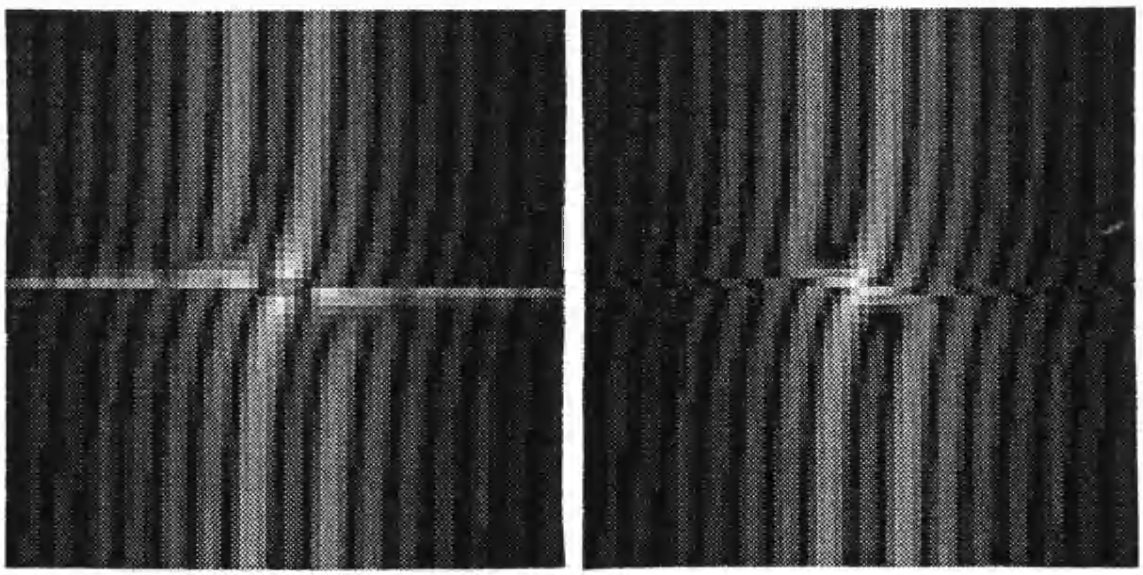

Figure 4.32a&b Figure a (left) exact and figure b (right) first order approximation for a crystal containing a tilted screw dislocation with values $\lambda = 1$, $T = 40$ and $B = -40$.

Figures 4.33*a* and *b* are taken with the values $\lambda = 1$, $T = 40$ and $B = 0$. The

figure shows the splitting of the figure into three regions. The left hand side, $x < 0$, shows the fringes to be little affected by the dislocation and are only slightly bent as we approach the dislocation. The right hand side, $x > 0$, shows the fringes bending as they approach the dislocation line and a fringe shift of 2 upon crossing it. In the centre the fringes, $x \sim 0$, try to join up, such that all the fringes are continuous. All three regions are in good agreement with the

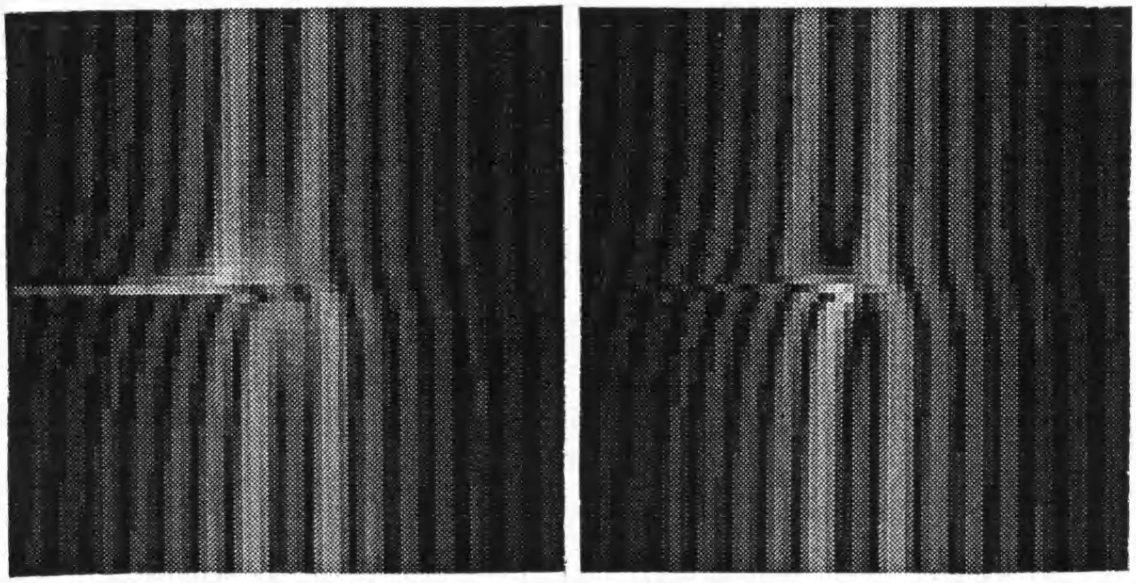

Figure 4.33a&b Figure a (left) exact and figure b (right) first order approximation for a crystal containing a tilted screw dislocation with values $\lambda = 1$, $T = 40$ and $B = 0$.

dynamical fringe following rule. The dislocation line runs from $x = 0$ to $x = 40$, hence on the left hand side $x < 0$ there is no displacement of the fringes, on the right hand side $x > 0$ the fringe shift is by 2 fringes and at the centre $x \approx 0$ the number of fringes is conserved. LACBED patterns were also taken with the values $\lambda = 1$, $T = 0$ and $B = 40$, figures 4.34. In other words the slope is

simply tilted in the opposite direction. No changes from those of figures 4.33$a$ and $b$ were found. Thus the direction of tilting cannot be distinguished from the pattern!

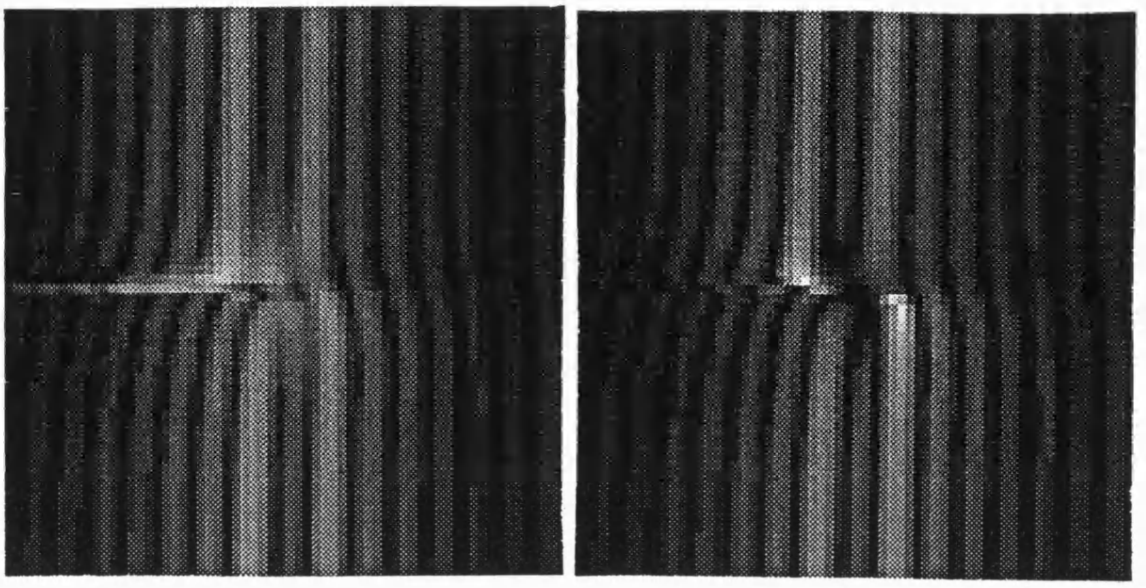

Figure 4.34a&b Figure a (left) exact and figure b (right) first order approximation for a crystal containing a tilted screw dislocation with values $\lambda = 1$, $T = 0$ and $B = 40$.

Figures 4.35$a$ and $b$ are taken with the values $\lambda = 1$, $T = 15$ and $B = -15$. Similar results to those of figures 4.33a and b are found. The figure shows the splitting of the figure into three regions. The left hand side, $x < -15$, and the right hand side, $x > 15$ show the fringes to be unaffected by the dislocation and as in the perfect case are straight and parallel. In the centre region the fringes bend as they approach the dislocation line and a fringe shift of 2 is made upon crossing it. At $x \sim -15$ and $x \sim 15$ the fringes bend such that they appear to

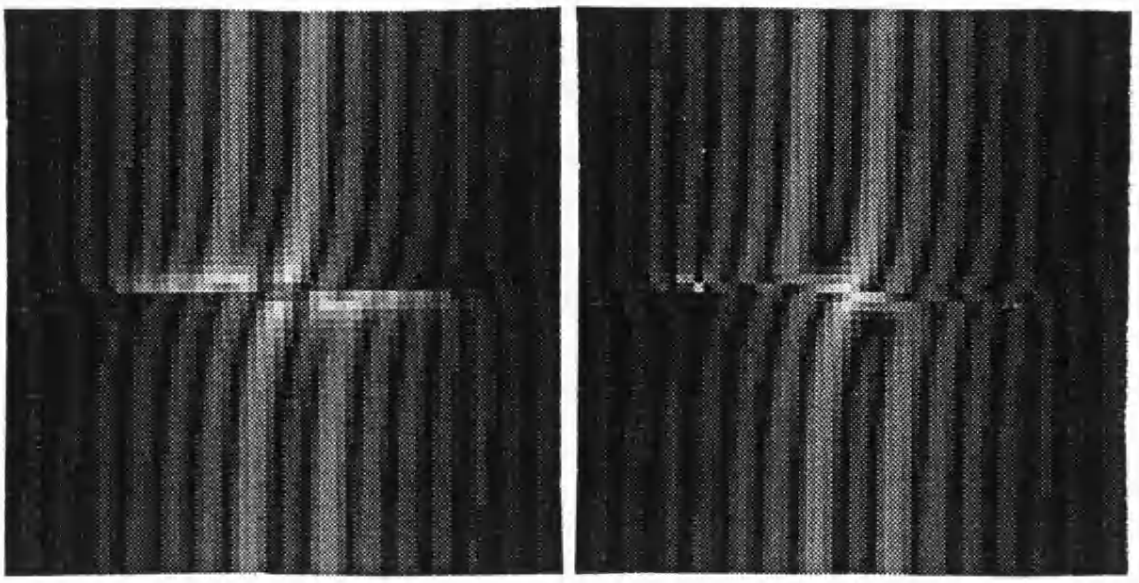

Figure 4.35a&b Figure a (left) exact and figure b (right) first order approximation for a crystal with a tilted screw dislocation, where $\lambda = 1$, $T = 15$ and $B = -15$.

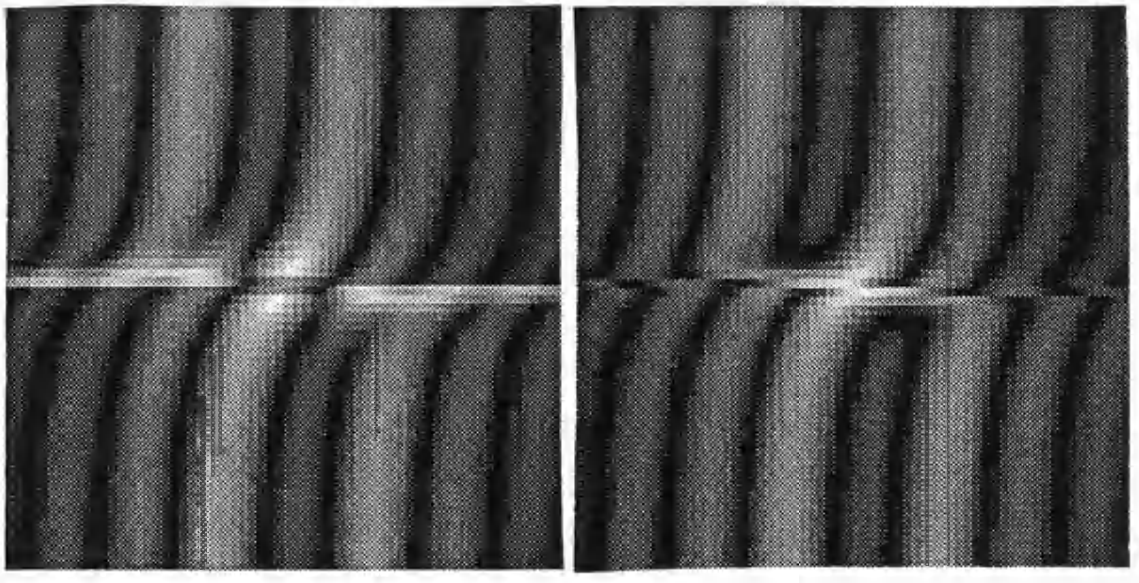

Figure 4.36a&b Figure a (left) exact and figure b (right) first order approximation for a crystal with a tilted screw dislocation, where $\lambda = 0.5$, $T = 40$ and $B = -40$.

be continuous and such that the total number of fringes is consevered.

Figures 4.36a and b are calculated with the values $\lambda = 0.5$, $T = 40$ and $B = -40$ and figures 4.37a and b have the values $\lambda = 0.5$, $T = 40$ and $B = 0$. Both sets of figure shows the splitting of the figure into three regions. The only differences from their respective $\lambda = 1$ figures (4.32 and 4.33) are that the fringes have become thicker.

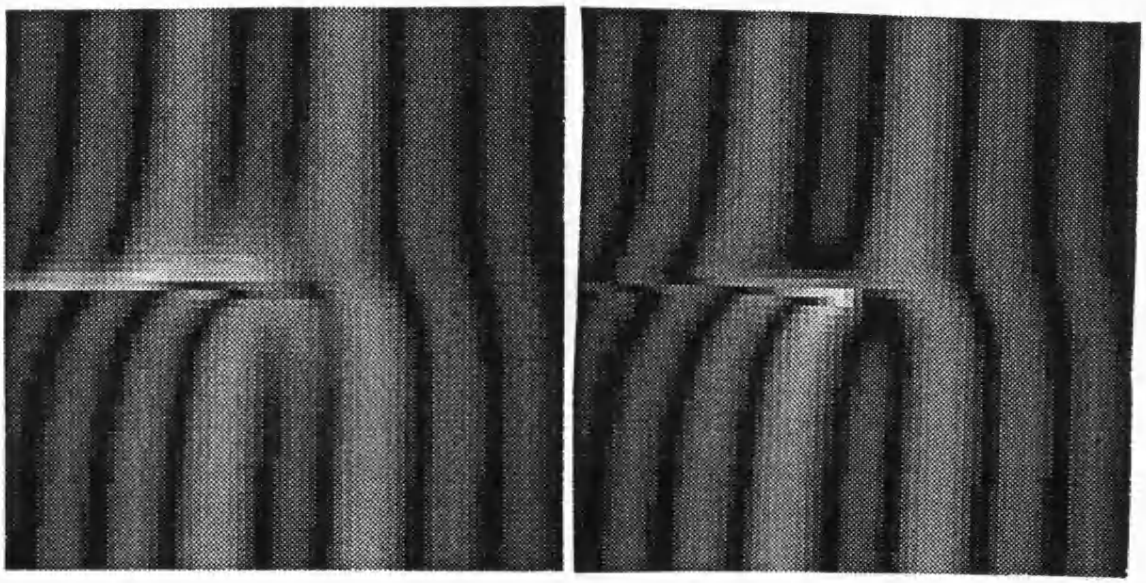

Figure 4.37a&b Figure a (left) exact and figure b (right) first order approximation for a crystal containing a tilted screw dislocation with values $\lambda = 0.5$, $T = 40$ and $B = 0$.

These sets of figures suggest that an LACBED pattern will still obey the dynamical fringe following rule when the dislocation is sloped. Both the direction and the magnitude of the Burgers vector relative to the diffracting reciprocal vector can be still found. Figures 4.32 indicate that unless the dislocation cuts

the surface inside the area of interest, the LACBED pattern will not be affected and it will not be possible to identify any tilting of the dislocation and hence the value of the Burgers vector in the $z$-direction. Thus computationally (as discussed by Humble in Hren *et al* (1979) for the conventional EM case) the 3-dimensional problem, (4.8.7), effectively reduces to a 2-dimensional problem, (4.8.1). However because the area illuminated is of order 10000Å, whilst the crystal is only a few 100Å thick, the angle the dislocation line makes with the surface is very small. For example for a 200Å thick crystal it must be less than 1.2 degrees (and for any such small angle, (4.8.7) to first order reduces to (2.8.1)). Where the dislocation does not cut the surface the Burgers vector will be almost parallel to the diffracting reciprocal lattice vector. Thus for thin crystals LACBED patterns are expected to be relatively insensitive to the sloping of a screw dislocation until its slope becomes of order a few degrees.

## 4.9 ABSORPTION.

In this section we shall attempt to include, in a simplified manner, the affects of absorption into our calculations. As discussed in section 2.1 this may be done by introducing an extra term into potential, such that

$$\beta \rightarrow \beta + i\beta'.$$

Here $\beta$ represents the potential due to elastic scattering and $\beta'$ that due to inelastic and diffuse scattering (Humphreys 1979). The absorbing potential $\beta'$ is assumed to be much smaller than the perfect potential $\beta$.

Again following the proceedure used in section 2.5, the 2-beam Howie-Whelan

Hamiltonian which includes absorption is

$$H(\theta) = \frac{1}{2}\begin{pmatrix} x & \beta\exp(i\phi) + i\beta'\exp(i\phi') \\ \beta\exp(-i\phi) + i\beta'\exp(-i\phi') & -x \end{pmatrix}. \quad (4.9.1)$$

We shall for simplicity assume that the phases, $\phi$ and $\phi'$, of the dimensionless potential parameters are the same (though this is not necessarily true; Bird and King 1990). They are then both equal to $\mathbf{G}\cdot\Delta\mathbf{R}$. The dimensionless modified 2-beam Howie-Whelan Hamiltonian including absorption is then

$$H = \frac{1}{2}\begin{pmatrix} x - \dot{\phi} & \beta + i\beta' \\ \beta + i\beta' & -x + \dot{\phi} \end{pmatrix}. \quad (4.9.2)$$

As before we may approximate the solutions to (4.9.2) using adiabatic iteration, but because we are now dealing with a non-hermitian Hamiltonian the analysis is slightly different. Now in order to find the diffracted intensity $I_{\mathbf{G}}$ we need to find expressions for both the left and the right hand eigenstates. This is because for the non-hermitian case, the left and right hand eigenstates are not conjugates of one another (e.g. Dederichs (1972)).

The right hand instantaneous eigenstates of the non-hermitian Hamiltonian of (4.9.2) are given by the solutions of

$$\frac{1}{2}\begin{pmatrix} x - \dot{\phi} & \beta + i\beta' \\ \beta + i\beta' & -x + \dot{\phi} \end{pmatrix}\begin{pmatrix} C_{\mathbf{0}}^{j} \\ C_{\mathbf{G}}^{j} \end{pmatrix} = s^{j}\begin{pmatrix} C_{\mathbf{0}}^{j} \\ C_{\mathbf{G}}^{j} \end{pmatrix}. \quad (4.9.3)$$

Similar to the derivation in section 4.6 the right hand eigenstates of (4.9.3) are

$$\begin{pmatrix} C_{\mathbf{0}}^{j} \\ C_{\mathbf{G}}^{j} \end{pmatrix} = \frac{1}{\sqrt{2}}\begin{pmatrix} (1 + \frac{x-\dot{\phi}}{2s^{j}})^{\frac{1}{2}} \\ \pm(1 - \frac{x-\dot{\phi}}{2s^{j}})^{\frac{1}{2}} \end{pmatrix}, \quad (4.9.4)$$

and their respective eigenstates are

$$s^{1} = -s^{2} = \frac{1}{2}\sqrt{(x-\dot{\phi})^{2} + (\beta + i\beta')^{2}}. \quad (4.9.5)$$

The eigenvalues are no longer real . As we are making the approximation $\beta' \gg \beta$, we shall ignore the term $\beta'^2$ in comparison with $\beta^2$. In this case the eigenvalues may be approximated as

$$s^1 = -s^2 = \frac{1}{2}\sqrt{(x-\dot{\phi})^2+\beta^2} + \frac{i\beta\beta'}{2\sqrt{(x-\dot{\phi})^2+\beta^2}}. \tag{4.9.6}$$

As before the parallel transported phase is zero.

The left hand instantaneous eigenstates of the non-hermitian Hamiltonian (4.9.2) are given by the solutions of

$$(\hat{C}_{\mathbf{0}}^{j^*} \quad \hat{C}_{\mathbf{G}}^{j^*}) \frac{1}{2}\begin{pmatrix} x-\dot{\phi} & \beta+i\beta' \\ \beta+i\beta' & -x+\dot{\phi} \end{pmatrix} = (\hat{C}_{\mathbf{0}}^{j^*} \quad \hat{C}_{\mathbf{G}}^{j^*})\,\hat{s}^{j^*}. \tag{4.9.7}$$

In (4.9.7), and similarly in what follows, the $\hat{}$ signifies that this is the left hand instantaneous eigenstate. Similar to the derivation of the right hand eigenstates, the left hand eigenstates are given by

$$(\hat{C}_{\mathbf{0_0}}^{j^*} \quad \hat{C}_{\mathbf{G_0}}^{j^*}) = \frac{1}{\sqrt{2}}(\ (1+\tfrac{(x-\dot{\phi})}{\hat{s}^{j^*}})^{\frac{1}{2}} \quad \pm(1-\tfrac{(x-\dot{\phi})}{\hat{s}^{j^*}})^{\frac{1}{2}}\ ), \tag{4.9.8}$$

The respective eigenvalues are again given by (4.9.5) and (4.9.6), $s^j = \hat{s}^{j^*}$.

The first order adiabatic approximation for the right hand diffracted wavefunction is then

$$\psi_{\mathbf{G}}(1) = \sum_{j=1}^{2} \hat{C}_{\mathbf{0_0}}^{j^*}(-1) C_{\mathbf{G_0}}^{j}(1) \exp(i\int_{-1}^{1} s^j d\theta) \tag{4.9.9a}$$

Now for simplicity we shall only consider crystals containing a symmetric displacement field, where $\dot{\phi}(\theta) = \dot{\phi}(-\theta)$. Then using (4.9.4), (4.9.8) and (4.9.6), (4.9.7a) becomes

$$\psi_{\mathbf{G}}(1) = \frac{i\beta \sin(\int_{-1}^{1} s^j d\theta)}{\sqrt{(x-\dot{\phi}(1))^2+\beta^2}}, \tag{4.9.9b}$$

where in contrast to (4.6.6b), $s^j$ is imaginary. From (4.9.6) and (4.9.9) the diffracted intesity at the bottom of the crystal is

$$I_{\mathbf{G}}(1) = |\psi_{\mathbf{G}}(1)|^2$$
$$= \frac{\beta^2 \sin^2(\int_{-1}^{1} \sqrt{(x-\dot{\phi})^2 + \beta^2} d\theta)}{(x-\dot{\phi}(1))^2 + \beta^2} \sinh(-\beta\beta' \int_{-1}^{1} \{(x-\dot{\phi})^2 + \beta^2\}^{-1/2} d\theta). \tag{4.9.10}$$

Figures 4.38 and 4.39 show LACBED patterns for a central screw dislocation, where absorption is taken into account in the simplified manner discussed. The figures are taken with $\beta' = 0.1$ and 0.2 respectively. Figures *a* are the exact computed patterns and figures *b* the first order modified approximations, with the diffracted intensity given by (4.9.10). The same values, ranges and scaling is used as for previous patterns, figures 4.6a and 4.22.

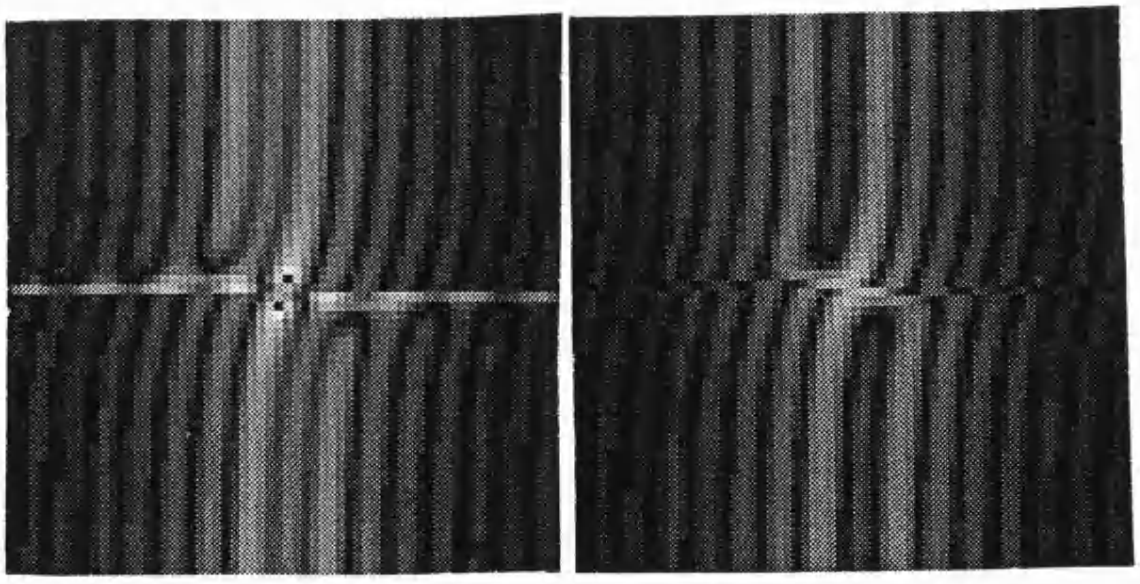

Figure 4.38a&b Figure a (left) exact and figure b (right) first order approximation for a crystal containing a central screw dislocation with absorption parameter $\beta' = 0.1$.

The effect of absorption on both patterns is simply to reduce the contrast slightly,

more so for the larger value of $\beta'$. This is true for both sets of patterns, which both show no changes in form to those previously. The patterns indicate that for thin crystals, which are smaller than the branch 1 absorption lengths, the only effect absorption will have is to reduce the contrast, without altering the pattern in any significant way. We are thus justified in ignoring, for thin crystals, the effects of absorption.

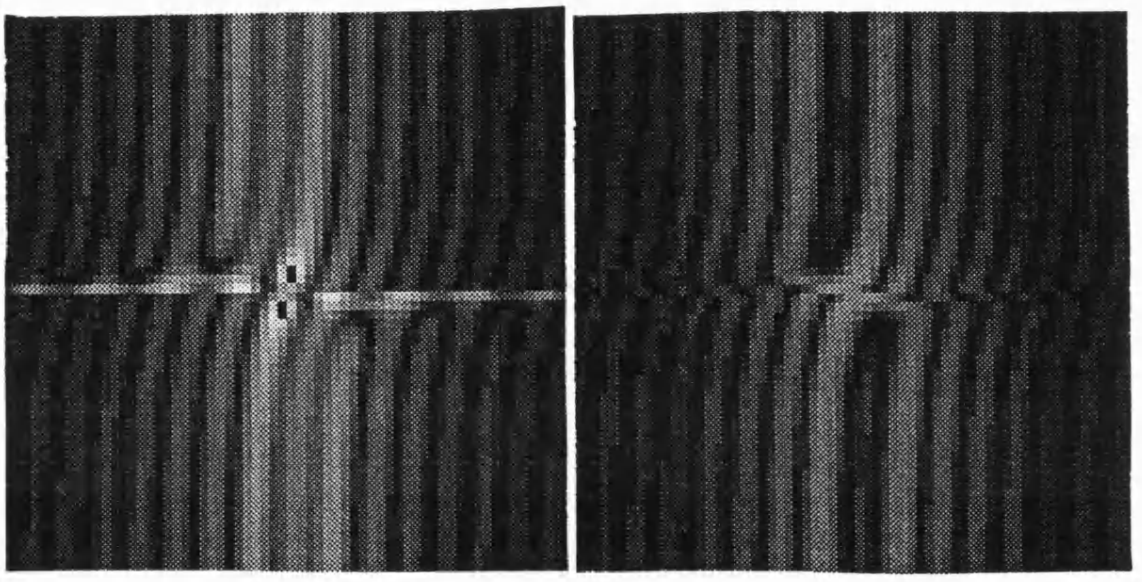

Figure 4.39a&b Figure a (left) exact and figure b (right) first order approximation for a crystal containing a central screw dislocation with absorption parameter $\beta' = 0.2$.

## 4.10 EVALUATION OF THE BURGERS VECTOR.

Now return to the question of why the fringe shift in a LACBED pattern of a crystal containing a screw dislocation is given by the term $\mathbf{G.b}/2\pi$. In order to answer this question we need to derive an expression for the total change in the $x$ value as we follow a line of constant intensity from $y = -\infty$ to $y = +\infty$. For

a given specimen which contains a screw dislocation, the diffracted intensity is a function of both $y$ and $x$, that is real and reciprocal space (see figure 4.3). A line of constant intensity may then be written as

$$dI_{\mathbf{G}} = \frac{\partial I_{\mathbf{G}}}{\partial x} dx + \frac{\partial I_{\mathbf{G}}}{\partial y} dy = 0.$$

Hence on any line of constant intensity

$$\frac{dy}{dx} = -\frac{\partial I_{\mathbf{G}}/\partial x}{\partial I_{\mathbf{G}}/\partial y}. \tag{4.10.1}$$

We shall only consider, because of its simplicity, the intensity given by the zeroth order adiabatic approximation, (4.5.5). We shall integrate (4.10.1) over a single fringe, from $y = -\infty$ to $y = +\infty$ and from $x - \Delta x/2$ to $x + \Delta x/2$, where $\Delta x$ is the total change in $x$ upon following a fringe through the dislocation. From (4.5.5) and (4.5.3) we have

$$\frac{\partial I_{\mathbf{G}}}{\partial x} = \frac{-x\beta^2 \sin(\alpha)\cos(\alpha)}{(x^2+\beta^2)^{3/2}} \left( -2 + \frac{\beta^2}{x(x^2+\beta^2)} \int_{-1}^{1} \dot{\phi}\, d\theta + \frac{2\tan(\alpha)}{(x^2+\beta^2)^{1/2}} \right)$$

and

$$\frac{\partial I_{\mathbf{G}}}{\partial y} = \frac{-x\beta^2 \sin(\alpha)\cos(\alpha)}{(x^2+\beta^2)^{3/2}} \frac{d}{dy} \int_{-1}^{1} \dot{\phi}\, d\theta. \tag{4.10.2}$$

Here we have used the substitution

$$\alpha = \sqrt{x^2+\beta^2} - \frac{x}{2\sqrt{x^2+\beta^2}} \int_{-1}^{1} \dot{\phi}\, d\theta.$$

Substituting (4.10.2) into (4.10.1) gives the expression for a line of constant intensity as

$$\frac{dy}{dx} = -\frac{2 - \frac{\beta^2}{x(x^2+\beta^2)} \int_{-1}^{1} \dot{\phi}\, d\theta - \frac{2\tan(\alpha)}{(x^2+\beta^2)^{1/2}}}{\frac{d}{dy} \int_{-1}^{1} \dot{\phi}\, d\theta}. \tag{4.10.3}$$

If we look at the case where $|x| \gg \beta$, then the second term in the numerator of (4.10.3) may be ignored. Similarly we shall only concern ourselves with what

happens on a dark fringe, where $I_{\mathbf{G}} = 0$ implies that $\tan(\alpha) = 0$. Having done so, rewriting (4.10.3) and integrating over a dark fringe from $y = -\infty$ to $y = +\infty$ and from $x - \Delta x/2$ to $x + \Delta x/2$, (4.10.3) becomes

$$\int_{-\infty}^{+\infty} \frac{d}{dy} \int_{-1}^{1} \dot{\phi} \; d\theta \; dy = -2\Delta x. \tag{4.10.4}$$

At $y = \pm\infty$ because we are so far away from the dislocation, $\phi = 0$ and the left hand side of (4.10.4) may be rewriten as

$$\begin{aligned} \int_{-\infty}^{+\infty} \frac{d}{dy} \int_{-1}^{1} \dot{\phi} \; d\theta \; dy = & \int_{-\infty}^{+\infty} \frac{d}{dy}\phi(\theta = 1) \; dy + \int_{-1}^{1} \dot{\phi}(y = +\infty) \; d\theta \\ & + \int_{+\infty}^{-\infty} \frac{d}{dy}\phi(\theta = -1) \; dy + \int_{-1}^{1} \dot{\phi}(y = -\infty) \; d\theta. \end{aligned} \tag{4.10.5}$$

This may be done because the second and fourth terms on the right hand side of (4.10.5) are zero. But this is equivalent to taking a path around the dislocation (see figure 4.40). Thus (4.10.5) may be rewritten as

$$\int_{-\infty}^{+\infty} \frac{d}{dy} \int_{-1}^{1} \dot{\phi} \; d\theta \; dy = \oint_c d\phi = \mathbf{G}. \oint_c d\Delta\mathbf{R}. \tag{4.10.6}$$

By definition the right hand integral is simply the Burgers vector $\mathbf{b}$. The total change in $x$ in following a fringe of constant intensity from $y = -\infty$ to $y = +\infty$ is then given from (4.10.4) and (4.10.6) as

$$\Delta x = \pi \left( \frac{\mathbf{G}.\mathbf{b}}{2\pi} \right). \tag{4.10.7}$$

Hence we have established relationship between the fringe shift, $\Delta x$, and the expression $\mathbf{G}.\mathbf{b}/2\pi$. Because $\mathbf{b}$ is a crystal lattice vector and $\mathbf{G}$ is a reciprocal lattice vector, $\mathbf{G}.\mathbf{b} = 2n\pi$, where $n$ is an integer. This tells us that $x$ changes by a whole number, $n$, of units of $\pi$.

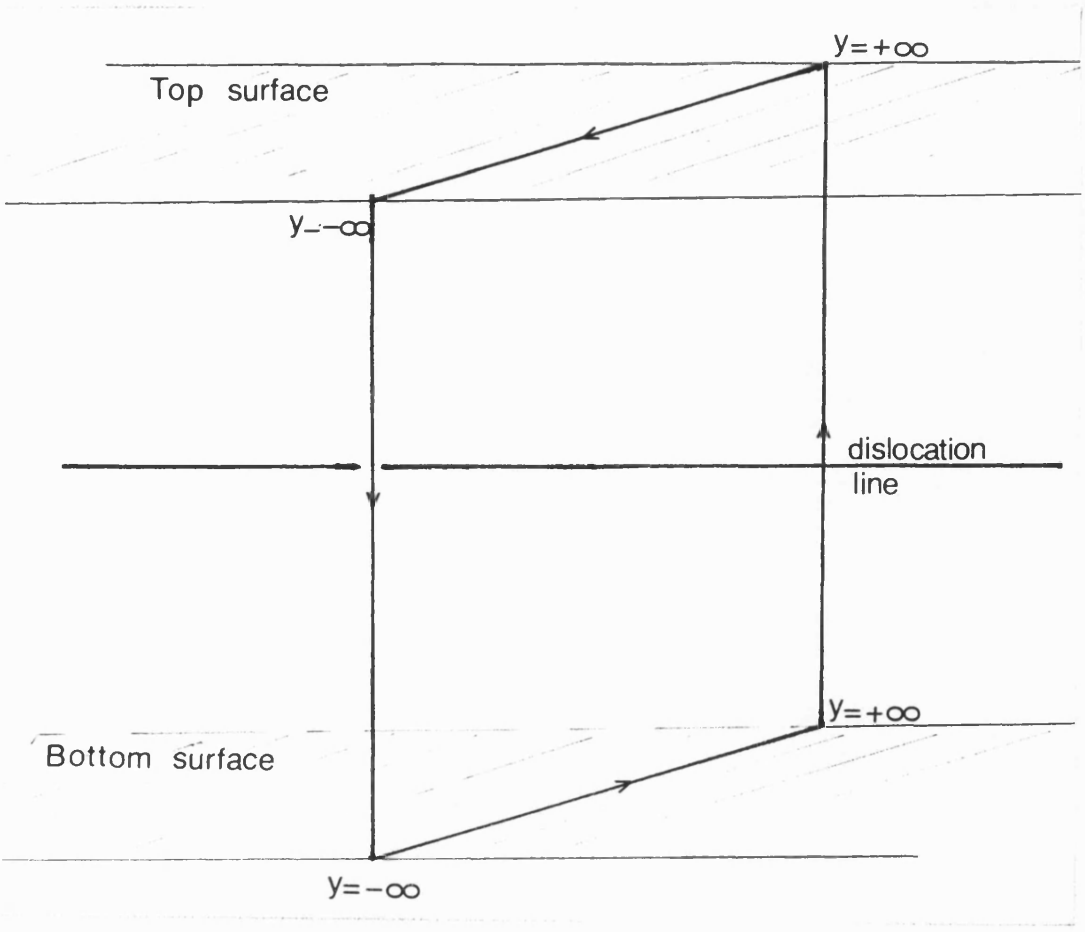


Figure 4.40 Path taken around the dislocation line.

Looking at our expression for the diffracted intensity, (4.5.5), we have for large values of $y$ and where $x \gg \beta$, the diffracted intensity may be written as

$$I_{\mathbf{G}} \approx \frac{\beta^2 \sin^2(x)}{x^2}. \tag{4.10.7}$$

Now before the dislocation is crossed, $x$ is such that $\dddot{x} = x - n\pi/2$ and $sin(x - n\pi/2) = \pm 1$ (i.e. a maximum or minimum). After the dislocation is crossed and we are far away from the dislocation line, because we are changing the argument in sine by a multiple, $n$, of $\pi/2$ it must remain either a maximum or a minumum,

and have passed through $n$ maximums and minimums. Thus $n$ gives the number of dark fringes that are crossed in travelling from $y = -\infty$ to $y = +\infty$ across a dislocation line.

# CHAPTER 5

# SCANNING TRANSMISSION ELECTRON MICROSCOPY.

## 5.1 INTRODUCTION.

In this chapter we shall turn to the general n-beam Howie–Whelan equations. Then the number of diffracted beams included in the calculations is limited only by the amount of computer time and memory, and by the accuracy of solution required. The particular case we shall examine is that of the influence of strain fields upon High Angle Annular Dark Field (HAADF) imaging in a Scanning Transmission Electron Microscope (STEM). In the next two sections we shall discuss STEM and HAADF imaging, together with a brief discussion of the influence of strain fields upon them. In the following section, 5.4, a detailed derivation of the HAADF intensity is presented. This includes both the exact intensity expression and an approximation based upon the adiabatic iteration scheme of chapter 3. In the following sections, 5.5 and 5.6, these HAADF intensity expressions will be used to both simulate and interpret HAADF images, for the cases of both perfect and strained crystals.

## 5.2 HIGH ANGLE ANNULAR DARK FIELD IMAGING.

As is done in CBED, in STEM the incident electron beam is focused to a highly converged probe, which is scanned across the specimen in a raster or pattern of parallel lines. Figure 5.1 shows the principle behind the instrument schematically. The illuminating beam, which may be orders of magnitude brighter than a conventional TEM beam, is provided by a field emission source. This is because, unlike TEM where all the points are illuminated at the same time, in STEM

each point in the raster is illuminated for only a small fraction of the total exposure time. Electromagnetic lenses demagnify the small electron source and project it onto the specimen with a spot diameter which can be 2Å or smaller (Pennycook and Jesson 1991). Scanning coils allow the the probe to be move in a raster over the specimen.

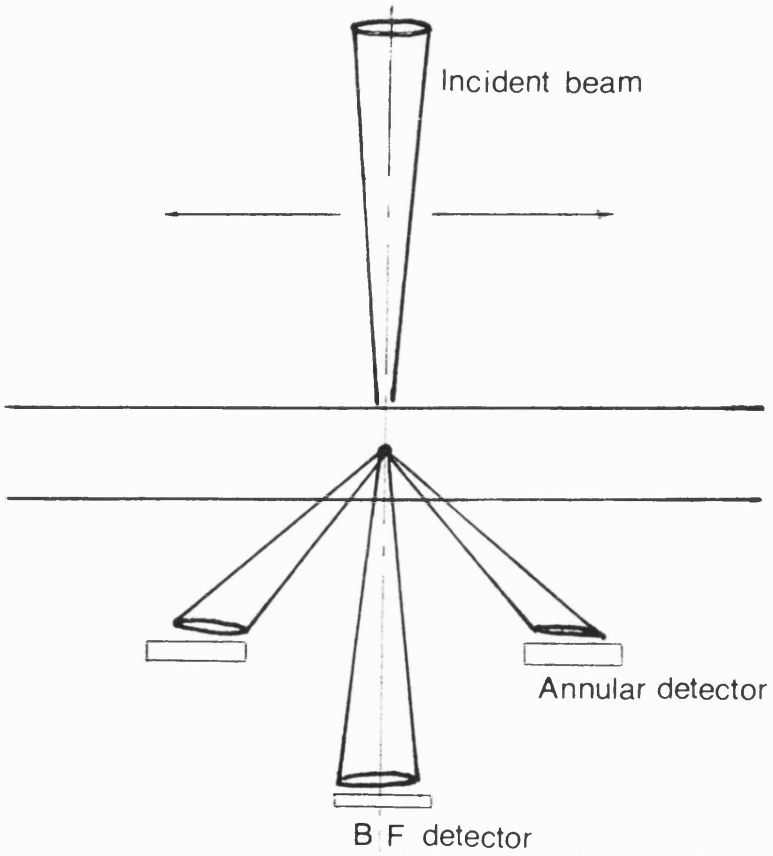


Figure 5.1 Principles of a Scanning Transmission Electron Microscope.

Despite the success of using Z-contrast techniques in STEM to image heavy atoms on thin amorphous substrates (Crewe, Langmore and Isaacson 1975) or in imaging biological specimens (Crewe 1971; Crewe and Wall 1970), the techniques have been less successful when used to investigate crystalline specimens. This is because diffraction plays an important role in imaging crystalline specimens and can significantly complicate the interpretation (Donald and Craven

1980). In order to avoid diffraction affects in imaging crystalline specimens, Howie (1979) suggested collecting those electrons scattered through high angles. This can be done by use of an annular detector. The inner angle of the detector is chosen so that it cuts out Bragg scattering, whilst the detector's outer angle is large enough to collect nearly all of the remaining high angle scattered beam. The advantage of this is that at increasing angles the Bragg refected beams are progressively replaced by thermal diffuse scattering (TDS) (Hall and Hirsch 1965). A disadvantage of collecting only those electrons scattered through high angles is that a smaller proportion of the total electron beam is detected. However the advantages in using High Angle Annular Dark Field imaging more than compensates. HAADF imaging simplyifies the image interpretation by both simplifying the diffraction effects and by improving the compositional sensitivity (Pennycook and Jesson 1990).

In conventional HREM the dominating scattering process is coherent Bragg scattering with TDS playing only a minor background role. In contrast in STEM as the inner collection angle is increased the effects of TDS increasingly replace that of Bragg scattering. Thus in HAADF imaging the dominant scattering process is the incoherent TDS. This destruction of coherent scattering means that the intensity collected at the lower surface of the crystal will be generated from each atom within the crystal scattering essentially independently of all others. Contrast changes due to orientation are then replaced by contrast changes due to channelling.

As we have been doing, we shall continue to use a Bloch wave interpretation. We shall see that this allows a clear and easily interpretable insight into the

formation of images in HAADF. Because the only scattering collected is that which is scattered through large angles, in effect only the tightly bound Bloch states make any significant contribution to the image. The scattering is thus made in proportion to electron intensity at the atomic sites. Clearly the $1s$ states, which are the most tightly bound, will contribute the most and need be considered alone (Pennycoook and Jesson 1991). It is reasonable to assume that when the $1s$ states on one string are so tightly bound that they do not overlap significantly with the $1s$ states on other strings, the intensity which is initially incident upon a string will be channelled down that string and so will allow a simple column by column interpretation.

HAADF imaging in STEM can thus be described in simple terms as the channelling of the incident beam along the $1s$ states of the axial columns of atoms. Due to the destruction of Bragg scattered waves there is no contrast reversal with thickness or focus, and little complication due to diffraction effects. The image seen in a HAADF micrograph will then be representative of the scattering source and can provide a clear, simple and unambiguous determination of atomic structures (see for example Pennycook *et al* 1986; Pennycook and Boater 1988; Pennycook 1989 or Pennycook and Jesson 1991) with resolutions of order only a few Å.

### 5.3 HAADF AND STRAIN FIELDS.

We now turn to the question of how strain will affect HAADF images. First, in this section let examine what happens using only a simple argument, leaving the detailed analysis to the following sections. It is well known that strain fields may seriously alter conventional HREM images (Humphreys 1979; Hirsch *et al*

1977). For example, strain may greatly complicate the interpretation of edge-on interfaces between lattice mismatched materials. In contrast however, there is reason to believe that HAADF images may be much less sensitive to strain than conventional HREM imaging. Recently Pennycook and coworkers have presented a number of papers on HAADF imaging, in which crystal interfaces are examined (see for example Pennycook and Jesson 1990, and other papers mentioned in this chapter). In these images it appears that interfacial strains do not greatly, if at all, affect the HAADF images.

Why should this be so? In conventional HREM the image arises from the interference of several diffracted beams, each of which is governed by all the excited Bloch waves in the specimen. The strain field causes transitions between the Bloch waves, affecting their amplitudes and phases, and therefore changing the details of the HREM image. In HAADF imaging the only Bloch waves which contribute significantly to the formation of an image are those which are tightly bound to the atomic strings (Pennycook and Jesson 1991). In effect this means only the $1s$ states need be considered, and hence the relative phases of different Bloch waves are less important. Because the $1s$ states are tightly bound it is reasonable to expect they will be able to follow the bending of atomic strings and so are relatively unaffected by strain.

Two illustrations of this are shown in figure 5.2, where the crystals are deformed by small strain fields. In figure 5.2a all of the atomic columns are deformed in exactly the same manner. The incident beam is then channelled down the columns by the $1s$ states and the emerging intensity distribution is unchanged from that of the top surface. Similarly in figure 5.2b although the columns are

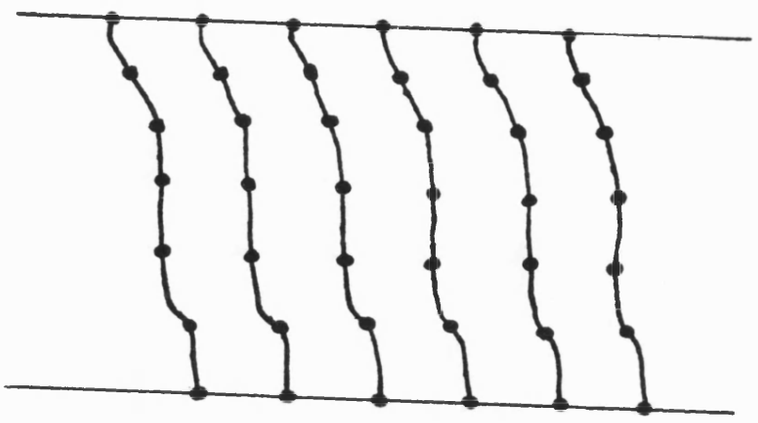

Figure 5.2a Crystal where the atomic columns are deformed in an identical manner.

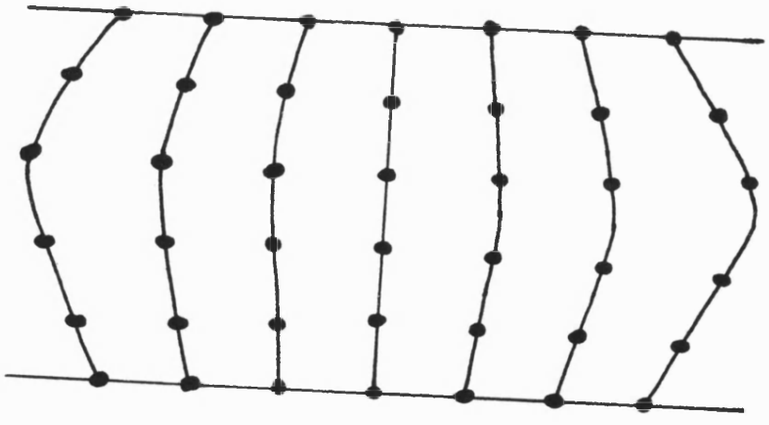

Figure 5.2b Crystal where the atomic columns are deformed in differing ways.

deformed in different ways, the atomic arrangement at both surfaces is the same. The spatial arrangement of the channelled intensity for both figures is then identical to that at the top surface and the deformation will have little effect on the images.

## 5.4 HAADF INTENSITY.

Here in this section we shall derive an expression for the HAADF intensity at the bottom surface of a strained crystal using adiabatic iteration. We shall presume for the moment that absorption plays only a minor role and need not be considered. It may of course be included adding an imaginary component $iV'$ to the real lattice potential, as was done in section 4.9 for the 2-beam case. Later in this chapter we shall only concern ourselves with those cases where absorption may realistically be ignored. First the general HAADF intensity is derived and then simplified by use of the adiabatic iteration scheme.

From (3.1.22) the electron wavefunction at a point $(\mathbf{R}, z)$ inside the deformed crystalline specimen may be written as

$$\psi(\mathbf{R}, z) = \int_{1^{st}BZ} d\mathbf{K} \sum_j \epsilon^j(\mathbf{K}, z)\tau^j(\mathbf{K}, \mathbf{r}) \exp(-\frac{i}{2k}\int_0^z s^j(\mathbf{K}, z')dz'). \quad (5.4.1)$$

Here we have, as we shall continue to do so, assumed there is perfect coherence in the incident beam. We have integrated over the wavevector, $\mathbf{K}$, in (5.4.1) because the effective probe diameter is of order an atomic distance or smaller (i.e. high resolution). The uncertainty principle states that the position of a beam can only be described precisely if it is made up from an infinite range of wavenumbers. For convenience we shall define the integral in $\mathbf{K}$ space to be over the first Brillouin Zone (BZ) only. This is done purely to make the algebra

easier and in does not affect the intensity calculation. Later, when we derive an expression for the boundary conditions, we shall return to the full extended Brillouin zone. The 2-dimensional ($\mathbf{R}$) Bloch states of (5.4.1) at depth $z$ are given by

$$\tau^j(\mathbf{K},\mathbf{r}) = \exp(i\gamma^j(\mathbf{K},z)) \sum_{\mathbf{G}} C^j_{\mathbf{G}}(\mathbf{K},z) \exp(i\{\mathbf{K}+\mathbf{G}\}\cdot\{\mathbf{R}-\Delta\mathbf{R}\}). \quad (5.4.2)$$

As discussed in section 5.2 an expression for the HAADF intensity from a crystalline specimen of thickness $T$, due to an incident probe at position $(\mathbf{R}_0, 0)$ on the top surface can be approximated by summing the intensity scattered from each individual atom, at site $(\mathbf{R}_i, z)$, in the specimen,

$$I(\mathbf{R}_0,T) \propto \sum_{z=0}^{T} \sum_i |\psi(\mathbf{R}_i,z)|^2 . \quad (5.4.3)$$

Because we are looking at a zone axis the atoms will form strings with coordinates $\mathbf{R}_i$. But as we have already mentioned in section 2.2, the wavefunction varies slowly and smoothly in the $z$ direction. Thus the sum over $z$ in (5.4.3) may be simplified by replacing the sum over $z$ with an integral, giving

$$I(\mathbf{R}_0,T) \propto \sum_i \int_0^T dz\, |\psi(\mathbf{R}_i,z)|^2 . \quad (5.4.4)$$

Substituting (5.4.1) into (5.4.4) the HAADF intensity may be approximated as

$$I(\mathbf{R}_0,T) \propto \int_{1^{st}BZ} d\mathbf{K} \int_{1^{st}BZ} d\mathbf{K}' \sum_{jj'} \int_0^T dz \sum_i \tau^{j'^*}(\mathbf{K}',\mathbf{R}_i,z)\tau^j(\mathbf{K},\mathbf{R}_i,z)$$
$$\epsilon^j(\mathbf{K},z)\epsilon^{j'^*}(\mathbf{K}',z) \exp(\frac{i}{2k}\int_0^z \{s^{j'}(\mathbf{K}',z') - s^j(\mathbf{K},z')\}dz'). \quad (5.4.5)$$

We shall now take some complicated paths in order to make the HAADF intensity expression, (5.4.5), easier to both analyse and compute. First let us look

at the sum over $i$. The $i$ dependence enters the intensity expression (5.4.5) only through the Bloch states, given by (5.4.2). For a perfect crystal the position of each atom in the 2-dimensional $\mathbf{R}$ plane may be more conveniently written as

$$\mathbf{R}_i = \mathbf{L} + \mathbf{R}_\chi,$$

where $\mathbf{L}$ is a lattice vector and $\mathbf{R}_\chi$ is the position of the $\chi^{th}$ atom in the unit cell. The effects of the strain field now enters through the changes to the position of the $\chi^{th}$ atom $\mathbf{R}_\chi$, which becomes $\mathbf{R}_\chi \longrightarrow \mathbf{R}_\chi - \Delta\mathbf{R}(z)$ The sum over $i$ is then replaced with sums over $\mathbf{L}$ and $\chi$, i.e.

$$\sum_i \rightarrow \sum_{\mathbf{L}} \sum_{\chi},$$

The sum over $i$ becomes

$$\sum_i \tau^{j'^*}(\mathbf{K}',\mathbf{r})\tau^j(\mathbf{K},\mathbf{r}) \propto \sum_{\mathbf{G}\mathbf{G}'} C^{j'^*}_{\mathbf{G}'}(\mathbf{K}',z) C^j_{\mathbf{G}}(\mathbf{K},z) \exp(i\gamma^j(\mathbf{K},z) - i\gamma^{j'}(\mathbf{K}',z)) \sum_{\mathbf{L}} \sum_{\chi} \exp(i\{\mathbf{K}+\mathbf{G}-\mathbf{K}'-\mathbf{G}'\}\cdot\{\mathbf{L}+\mathbf{R}_\chi - \Delta\mathbf{R}\}). \tag{5.4.6}$$

Now in (5.4.6) $\mathbf{G}$ is a reciprocal lattice vector and $\mathbf{L}$ is a lattice vector, hence $\exp(i\{\mathbf{G}-\mathbf{G}'\}\cdot\mathbf{L}) = 1$. Also $\frac{1}{N}\sum_{\mathbf{L}} \exp(i\{\mathbf{K}-\mathbf{K}'\}\cdot\mathbf{L}) = \delta_{\mathbf{K},\mathbf{K}'}$, where $N$ is a normalising constant (Ziman 1979). This is because we are only concerned with elastic scattering and, for the moment, restricting the wavevectors to lie within one Brillouin zone. Upon substituting (5.4.6) back into (5.4.5) and using the delta function, the expression for the HAADF intensity becomes

$$I(\mathbf{R}_0,T) \propto \sum_{jj'} \int_{1^{st}BZ} d\mathbf{K} \int_0^T dz \epsilon^j(\mathbf{K},z)\epsilon^{j'^*}(\mathbf{K},z) \exp(\frac{i}{2k}\int_0^z \{s^{j'}(\mathbf{K},z') - s^j(\mathbf{K},z')\}dz') \exp(i\gamma^j(\mathbf{K},z) - i\gamma^{j'}(\mathbf{K},z)) \sum_{\mathbf{G}\mathbf{G}'} C^j_{\mathbf{G}}(\mathbf{K},z) C^{j'^*}_{\mathbf{G}'}(\mathbf{K},z) \sum_{\chi} \exp(i\{\mathbf{G}-\mathbf{G}'\}\cdot\{\mathbf{R}_\chi - \Delta\mathbf{R}\}). \tag{5.4.7}$$

This may be rewritten more convieniently as

$$I(\mathbf{R}_0, T) \propto \sum_{\chi} \int_0^T dz \int_{1^{st}BZ} d\mathbf{K} \, |A_\chi(\mathbf{K}, z)|^2 \qquad (5.4.8a)$$

where

$$A_\chi(\mathbf{K}, z) = \sum_j \epsilon^j(\mathbf{K}, z) \exp(-\frac{i}{2k} \int_0^z s^j(\mathbf{K}, z')dz') \exp(i\gamma^j(\mathbf{K}, z)) \sum_{\mathbf{G}} C^j_{\mathbf{G}}(\mathbf{K}, z) \exp(i\mathbf{G} \cdot \{\mathbf{R}_\chi - \Delta\mathbf{R}\}). \qquad (5.4.8b)$$

$A_\chi(\mathbf{K}, z)$ is effectively the Fourier transform of the wavefunction $\psi$, (5.4.1). It describes how the amplitudes of the waves that contribute to $\psi$ vary with wavenumber $\mathbf{K}$ and specifies the wavegroup as completely as does $\psi$. Thus (5.4.8) indicates that, due to the large collection angle, all coherent contributions have been lost and the relative phase information from atoms inside the crystal are ignored. The intensity is in effect formed by squaring the wave amplitudes, $A_\chi(\mathbf{K}, z)$, summing over all atom types in the crystal integrating over the crystal thickness from $z = 0$ to $z = T$ and integrating over $\mathbf{K}$.

**Boundary conditions.**

In order to proceed further we need an expression for the excitation amplitudes at the top surface, $z = 0$. We shall now derive such an expression.

Let the incident probe at $(\mathbf{R}_0, 0)$ be written as

$$\phi(\mathbf{R}, \mathbf{R}_0, 0) = \int_{all\ space} d\mathbf{K} \; P(\mathbf{K}) \exp(i\mathbf{K} \cdot \{\mathbf{R} - \mathbf{R}_0\}). \qquad (5.4.9)$$

where $P(\mathbf{K})$ is a function which desribes the shape of the incident wavefunction. The incident probe is integrated over the whole of $\mathbf{K}$ space. In order to derive the boundary conditions we shall multiply the right hand sides of (5.4.1) and

(5.4.9) by $\tau^{j'^*}$, where

$$\tau^{j'^*}(\mathbf{K}',\mathbf{R}) = \sum_{\mathbf{B}} C_{\mathbf{B}}^{j^*}(\mathbf{K}',0)\exp(-i\{\mathbf{K}'+\mathbf{B}\}\cdot\mathbf{R})$$

and the wavevector $\mathbf{K}'$ lies in the first Brillioun zone. We shall then integrate over all $\mathbf{R}$ space. Doing so to (5.4.1), gives

$$\begin{aligned}
&\int_{1^{st}BZ} d\mathbf{K} \sum_j \epsilon^j(\mathbf{K},0)\tau^{j'^*}(\mathbf{K}',\mathbf{R})\tau^j(\mathbf{K},\mathbf{R}) \\
&\quad = \int_{1^{st}BZ} d\mathbf{K} \sum_j \epsilon^j(\mathbf{K},0) \sum_{\mathbf{GB}} C_{\mathbf{B}}^{j'^*}(\mathbf{K}',0) C_{\mathbf{G}}^j(\mathbf{K},0) \\
&\qquad\qquad \int \frac{d\mathbf{R}}{NA_c}\exp(i\{\mathbf{K}+\mathbf{G}-\mathbf{K}'-\mathbf{B}\}\cdot\mathbf{R}) \\
&\quad = \int_{1^{st}BZ} d\mathbf{K} \sum_j \epsilon^j(\mathbf{K},0) \sum_{\mathbf{GB}} C_{\mathbf{B}}^{j'^*}(\mathbf{K}',0) C_{\mathbf{G}}^j(\mathbf{K},0)\delta_{\mathbf{GB}}\delta(\mathbf{K}-\mathbf{K}') \\
&\quad = \epsilon^{j'}(\mathbf{K}',0). \qquad (5.4.10)
\end{aligned}$$

Here $A_c$ is the unit cell size, and so $NA_c$ is a normalising constant.

Similarly doing the same to (5.4.9) gives

$$\begin{aligned}
&\int_{all\ space} d\mathbf{K}P(\mathbf{K}) \sum_{\mathbf{B}} C_{\mathbf{B}}^{j'^*}(\mathbf{K}',0)\exp(-i\mathbf{K}\cdot\mathbf{R}_0)\int \frac{d\mathbf{R}}{NA_c}\exp(i\{\mathbf{K}-\mathbf{K}'-\mathbf{B}\}\cdot\mathbf{R}) \\
&\quad = \int_{all\ space} d\mathbf{K}P(\mathbf{K}) \sum_{\mathbf{B}} C_{\mathbf{B}}^{j'^*}(\mathbf{K}',0)\exp(-i\mathbf{K}\cdot\mathbf{R}_0)\delta(\mathbf{K}-(\mathbf{K}'+\mathbf{B})) \\
&\quad = \sum_{\mathbf{B}} P(\mathbf{K}'+\mathbf{B}) C_{\mathbf{B}}^{j'^*}(\mathbf{K}',0)\exp(-i\{\mathbf{K}'+\mathbf{B}\}\cdot\mathbf{R}_0). \qquad (5.4.11)
\end{aligned}$$

But at $z = 0$ (5.4.1) and (5.4.9) are equal to one another. Hence equations, (5.4.10) and (5.4.11) are also equal to each other at $z = 0$. The boundary conditions are thus given by

$$\epsilon^{j'}(\mathbf{K}',0) = \sum_{\mathbf{B}} P(\mathbf{K}'+\mathbf{B}) C_{\mathbf{B}}^{j'^*}(\mathbf{K}',0)\exp(-i\{\mathbf{K}'+\mathbf{B}\}\cdot\mathbf{R}_0). \qquad (5.4.12)$$

Note that in substituting (5.4.12) back into (5.4.1) we return to the extended Brillouin zone. Although we have restricted $\mathbf{K}'$ to the $1^{st}$ Brillouin zone, incident waves with $\mathbf{K}'+\mathbf{B}$ all contribute to $\epsilon(\mathbf{K}')$.

**Adiabatic approximation.**

Thus far, within the approximation made in chapter 2, and ignoring absorption and inelastic scattering, equation (5.4.8) is exact. It is however very time consuming to solve computationally, due to the excitation amplitudes, $\epsilon^j$, still being $z$ dependent. To solve it would require finding $\epsilon^j$ at each depth $z$ in the crystal. This in turn would require solving the respective first order differential $n \times n$ matrix equation at each $z$.

In order to simplify the computation we shall use the adiabatic iteration approximation theory derived in chapter 3. In adiabatic approximation the excitation amplitudes, $\epsilon^j$, are approximated as being constant and equal to their initial value at the top surface of the crystal (5.4.12).

Making the adiabatic approximation by substituting (5.4.12) into (5.4.8), the intensity expression becomes

$$\begin{aligned} I(\mathbf{R}_0,T) \propto \sum_{jj'} \int_{1^{st}BZ} d\mathbf{K} \sum_{\mathbf{BB'}} & \exp(i\{\mathbf{B'}-\mathbf{B}\}\cdot\mathbf{R}_0) P(\mathbf{K}+\mathbf{B}) P^*(\mathbf{K}+\mathbf{B'}) \\ & C^{j^*}_{\mathbf{B}}(\mathbf{K},0) C^{j'}_{\mathbf{B'}}(\mathbf{K},0) \int_0^T dz \exp(i\int_0^z \{s^{j'}(\mathbf{K},z') - s^j(\mathbf{K},z')\}dz'/2k) \\ & \exp(i\gamma^j(\mathbf{K},z) - i\gamma^{j'}(\mathbf{K},z)) \sum_{\mathbf{GG'}} C^j_{\mathbf{G}}(\mathbf{K},z) C^{j'^*}_{\mathbf{G'}}(\mathbf{K},z) \\ & \sum_{\chi} \exp(i\{\mathbf{G}-\mathbf{G'}\}\cdot i\{\mathbf{R}_\chi - \Delta\mathbf{R}\}). \end{aligned} \tag{5.4.13}$$

Equation (5.4.13) may be significantly simplified by making the substitutions

$$\begin{aligned} \mathbf{S} &\rightarrow \mathbf{G}+\mathbf{B} \\ \mathbf{S'} &\rightarrow \mathbf{G'}+\mathbf{B} \\ \mathbf{H} &\rightarrow \mathbf{B'}+\mathbf{B} \\ \hat{\mathbf{K}} &\rightarrow \mathbf{K}+\mathbf{B}. \end{aligned} \tag{5.4.14}$$

Then the HAADF intensity from a convergent beam probe centered on $(\mathbf{R}, 0)$ may be written as

$$I(\mathbf{R}_0, T) \propto \sum_{\mathbf{H}} \exp(i\mathbf{H} \cdot \mathbf{R}_0) U_{\mathbf{H}}(T) \qquad (5.4.15a)$$

where

$$\begin{aligned} U_{\mathbf{H}}(T) = & \sum_{jj'} \int_{all\ space} d\hat{\mathbf{K}}\ P(\hat{\mathbf{K}}) P^*(\hat{\mathbf{K}} + \mathbf{H}) C_{\mathbf{0}}^{j^*}(\hat{\mathbf{K}}, 0) C_{\mathbf{H}}^{j'}(\hat{\mathbf{K}}, 0) \int_0^T dz \\ & \sum_{\mathbf{SS'}} C_{\mathbf{S}}^{j}(\hat{\mathbf{K}}, z) C_{\mathbf{S'+H}}^{j'^*}(\hat{\mathbf{K}}, z) \exp(-\frac{i}{2k} \int_0^z \{s^j(\hat{\mathbf{K}}, z') - s^{j'}(\hat{\mathbf{K}}, z')\} dz') \\ & \exp(i\{\gamma^j(\hat{\mathbf{K}}, z) - \gamma^{j'}(\hat{\mathbf{K}}, z)\}) \sum_{\chi} \exp(i\{\mathbf{S} - \mathbf{S'}\} \cdot \{\mathbf{R}_\chi - \Delta\mathbf{R}\}) \end{aligned} \qquad (5.4.15b)$$

and we have returned to an extended zone scheme. The HAADF intensity can thus be approximated as a Fourier series expanded in terms of the reciprocal lattice vectors $\mathbf{H}$. This reflects the periodic nature of the scattering potential. It should be noted that the wavevector $\hat{\mathbf{K}}$ is now allowed to range over the complete Brillouin zone. The advantage of (5.4.15) over the previous intensity expressions lies in its ease of computation. Because the probe postion $\mathbf{R}_0$ enters the intensity expression only in the Fourier exponential, (5.4.15a), the Fourier coefficient $U_{\mathbf{H}}$, (5.4.15b), need only be evaluated once. This repesents a considerable saving in computing time, because the most costly term to evaluate is $U_{\mathbf{H}}$.

In the case of a perfect crystal, (5.4.15), is of course exact. Similar to the results presented in chapters 3 and 4, equation (5.4.15) will also give the exact solution for a crystal containing straight parallel tilted planes.

## 5.5 HAADF IMAGING AND ADIABATIC APPROXIMATIONS.

In this section we shall compare the two lowest order adiabatic approximations with the exact solution. As discussed in section 3.1, this may be done by using equation (3.1.29), however it is both impractical and expensive in computer time to do so. We could also use the intensity expression (5.4.15) to compare and contrast the approximations with the exact intensity results. However this again is expensive in computer time and for the exact solution it would only be practical to use (5.4.15) at a single orientation. Rather we shall use the wavefunction, (5.4.1), as a basis to compare the three solutions. Equation (5.4.1) gives the wavefunction of the electron beam at a point $(\mathbf{R}, z)$ inside the crystal. It is valid for both the exact solution and adiabatic approximations. The approximate wavefunctions differ from the exact wavefunction only by those terms which are dependent upon $z$.

To this end we may separate out the $z$ dependence by rewriting (5.4.1) as

$$\psi(\mathbf{R},z) = \int d\mathbf{K} \sum_{\mathbf{G}} \exp(i\{\mathbf{K}+\mathbf{G}\}\cdot\{\mathbf{R}-\Delta\mathbf{R})\psi_{\mathbf{G}}(\mathbf{K},z), \tag{5.5.1}$$

where for the exact solution

$$\psi_{\mathbf{G}}^{exact}(\mathbf{K},z) = \sum_{j} \epsilon^{j}(\mathbf{K},z) C_{\mathbf{G}}^{j}(\mathbf{K},z) \exp(i\gamma^{j}(\mathbf{K},z) \exp(-\frac{i}{2k}\int_{0}^{z} s^{j}(\mathbf{K},z')dz'). \tag{5.5.2a}$$

Similarly the first order unmodified and modified adiabatic approximation expressions for $\psi_{\mathbf{G}}$ are respectively

$$\psi_{\mathbf{G}}^{unmod}(\mathbf{K},z) = \sum_{j} \epsilon^{j}(\mathbf{K},0) C_{\mathbf{G}}^{j}(\mathbf{K},0) \exp(i\gamma^{j}(\mathbf{K},z) \exp(-\frac{i}{2k}\int_{0}^{z} s^{j}(\mathbf{K},z')dz') \tag{5.5.2b}$$

and

$$\psi_{\mathbf{G}}^{mod}(\mathbf{K},z) = \sum_j \hat{e}^j(\mathbf{K},0)\hat{C}_{\mathbf{G}}^j(\mathbf{K},z)\exp(-\frac{i}{2k}\int_0^z \hat{s}^j(\mathbf{K},z')dz'). \qquad (5.5.2c)$$

The extra notation used here, $\hat{C}$ etc ..., was defined in section 2.7. The only difference between the adiabatic approximations and the exact solution is then through the expression for $\psi_{\mathbf{G}}$. We shall analyse how good the approximations are by comparing the relative amplitude factors $\psi_{\mathbf{G}}$ using (5.5.2).

If the adiabatic approximations gives results which are in close agreement with the exact calculations, it follows that interband scattering must be relatively weak, i.e. the Bloch waves retain their own identity and are not strongly coupled. In this case, the effect on the ADF-STEM image should be small because the $1s$ state acts more-or-less independently of the other Bloch states and if its amplitude is not changing, its contribution to the intensity on the atomic sites will not be strongly affected. The varying phase relationships with the other Bloch waves are unimportant here, although they would of course matter for conventional HREM imaging.

We shall take a simple test case, the [111] axis of Silicon (Si), and include only 13 beams in our many beam calculations. The accelerating voltage is 100kV. The strain is caused by a model screw dislocation running through the center of a 200Å thick crystal, and the strain is varied by looking at the lattice distortion this would cause at various distances from the dislocation core. This particular strain field is chosen for convenience, but the results here are applicable to any distortion. The strain is quantified by a parameter $f$ which gives the ratio of the maximum angle through which the $(2\bar{2}0)$ lattice planes are turned, relative

to the $(2\bar{2}0)$ Bragg angle,

$$f = \frac{\theta}{\theta_B} = \frac{k\mathbf{G} \cdot \Delta\dot{\mathbf{R}}}{G^2}. \tag{5.5.3}$$

The results are shown in tables 1 to 4. These give the amplitude and phase for the reflections (000), $(2\bar{2}0)$ and $(4\bar{2}\bar{2})$, at the exact zone axis orientation, for four values of the strain parameter f. The $(2\bar{2}0)$ and $(4\bar{2}\bar{2})$ results are representative of the other $(2\bar{2}0)$ and $(4\bar{2}\bar{2})$ type reflections.

Table 1 represents the case of a perfect Si crystal (or one containing a dislocation, such that we are so far away from the core that there is no effective distortion). In such a case adiabatic theory is exact and the adiabatic solutions, (5.5.2b and c) agree with the exact solution (5.5.2a). We see that almost all of the HAADF intensity is contained in the undiffracted (000) beam, with the amount in the $(2\bar{2}0)$ beam being an order of magnitude smaller and that of the $(4\bar{2}\bar{2})$ an order smaller still. (Note ampl. = amplitude).

Table 1 Perfect crystal

f=0.0

| | exact solution | | zeroth order | | first order | |
|---|---|---|---|---|---|---|
| (hkl) | ampl. | phase | ampl. | phase | ampl. | phase |
| (000) | 0.93 | 1.17 | 0.93 | 1.17 | 0.93 | 1.17 |
| $(2\bar{2}0)$ | 0.15 | -0.08 | 0.15 | -0.08 | 0.15 | -0.08 |
| $(4\bar{2}\bar{2})$ | 0.02 | 0.11 | 0.02 | 0.11 | 0.02 | 0.11 |

Table 2 shows the results for the case of a Si crystal containing a central screw dislocation. The probe is 158Å perpendicular distance away from the dislocation

core. At this distance the $(2\bar{2}0)$ lattice planes are tilted through a tenth of the $(2\bar{2}0)$ Bragg angle; $f = 0.1$. For this $f$ factor, there is almost no change in the unmodified adiabatic approximation result. In contrast both the adiabatic modified and the exact amplitude factors have changed slightly. The adiabatic modified approximation is in almost perfect agreement with the exact amplitude factor.

Table 2. Deformed crystal

perpendicular distance=158Å

f=0.1

| | exact solution | | zeroth order | | first order | |
|---|---|---|---|---|---|---|
| (hkl) | ampl. | phase | ampl. | phase | ampl. | phase |
| (000) | 0.89 | 1.21 | 0.93 | 1.17 | 0.89 | 1.21 |
| $(2\bar{2}0)$ | 0.20 | -0.06 | 0.15 | -0.09 | 0.20 | -0.02 |
| $(4\bar{2}\bar{2})$ | 0.05 | -0.08 | 0.02 | 0.11 | 0.05 | -0.07 |

Now the adiabatic approximation assumes the excitation amplitudes to be constant (section 3.1). Hence whenever the exact and modified amplitude factors $\psi_{\mathbf{G}}$ are in good agreement, the excitation amplitudes $\epsilon^j$ are unchanging and there is is no significant interband scattering. The amplitudes of the $1s$ states then remain the same, though the phases may change, and the electrons are being channelled in the (modified) $1s$ states. Because the relative phases are less important in HAADF than in conventional imaging, the channelling $1s$ states will produce no change to the image. Table 2 thus indicates that at this level

of strain the modified approximation follows the lattice bending as well as the exact solution, and it is expected that an HAADF-image should therefore not be affected by the dislocation's strain field. Table 2 also shows that the dislocation causes amplitude from the undiffracted (000) beam to be scattered into the diffracted beams.

Table 3. Deformed crystal

perpendicular distance=79Å

f=0.2

| | exact solution | | zeroth order | | first order | |
|---|---|---|---|---|---|---|
| (hkl) | ampl. | phase | ampl. | phase | ampl. | phase |
| (000) | 0.78 | 1.25 | 0.93 | 1.17 | 0.83 | 1.26 |
| $(2\bar{2}0)$ | 0.20 | -0.01 | 0.15 | -0.09 | 0.22 | 0.11 |
| $(4\bar{2}\bar{2})$ | 0.06 | 0.12 | 0.02 | 0.11 | 0.06 | 0.12 |

In table 3 the wavefunction coefficients are shown for strain parameter $f = 0.2$, or at 79Å from the dislocation core. Here we see that the modified approximation is beginning to fail to follow the exact solution, or the lattice bending. However at this $f$ factor the modified results are still good enough to expect its image to be almost identical to that of the exact image. In a conventional high resolution microscope, it would be expected that at this distance, a strain field would clearly and visibly affect the image. In contrast in HAADF imaging, the image is not expected to be significantly altered from that of the perfect crystal image. At this $f$ factor a strain field would still be invisible in HAADF.

By the time the strain parameter increases to $f = 0.3$ (see table 4), at 53Å from the dislocation core, the modified approximation is clearly failing. Its amplitude values are not changing as fast as those of the exact solution, that is the modified approximation can not follow the rapidly bending lattice planes. At this level of strain parameter, or greater, it is expected that the strain field would affect the HAADF image and so be visible.

**Table 4. Deformed crystal**

**perpendicular distance=53Å**

**f=0.3**

| | exact solution | | zeroth order | | first order | |
|---|---|---|---|---|---|---|
| (hkl) | ampl. | phase | ampl. | phase | ampl. | phase |
| (000) | 0.69 | 1.32 | 0.93 | 1.17 | 0.80 | 1.32 |
| $(2\bar{2}0)$ | 0.21 | 0.10 | 0.15 | -0.10 | 0.27 | 0.34 |
| $(4\bar{2}\bar{2})$ | 0.08 | 0.46 | 0.02 | 0.11 | 0.07 | 0.44 |

Tables 1 to 4 imply that for a Si crystal in the (111) direction, HAADF imaging will be relatively insensitive to strain fields until the strain parameter is greater than $f = 0.2$. For strain parameters smaller than this, the strain field will be invisible to the HAADF image. These specific results can be carried across to more general results. We should expect that for any crystal, where the $1s$ states on the axial columns do not overlap, strain fields will not influence a HAADF image until the strain parameter becomes quite large (of order $f > 0.2$). HAADF imaging is then, compared to conventional high resolution imaging, relatively insensitive to small strains.

## 5.6 HAADF AND TILTED PLANES.

Here in this section we shall look at the case of a crystal containing straight parallel tilted planes, figure 5.2a. This may be thought of as an idealised case of a crystal containing very slowly bending planes, figure 5.2b. The reason for looking at crystals with tilted planes, as was discussed in section 2.7, is that the modified Howie-Whelan equations may then be solved exactly. Such solutions, and their interpretations, are expected to be good approximations to more realistically deformed crystals which contain slowly bending planes.

To begin with we shall first look at how the incident wavefunction is affected as it travels through the crystal. Two cases will be examined, those of a perfect and of a deformed crystal. In both of these cases we shall look at what role the potential plays, by first switching it off (so that there is no deforming crystal) and then switching it back on again. Having examined how the wavefunction will behave, we then turn to the appearence of the simulated HAADF images.

We shall take for our example the case of a 100keV electron probe with a Gaussian distribution (width 1.5Å) incident upon a 1000Å Silicon crystal in the [100] direction. The calculations are made from (5.4.1) ($\epsilon^j$ constant and $\tau^j$ $s^j$ "modified" solutions) with 1600 orientations in the **K** integral, all of which are in the first Brillouin zone ($\epsilon^j$ is given from (5.4.12)), and with 21 diffracted beams. Absorption is not included in the calculations. The absorption length for the $1s$ states at Si[100] at 100KeV is of order $\sim$ 1500Å or more (found using a Bird & King (1990) calculation), so absorption is not expected to significantly alter the details of the image, but rather to reduce the contrast slightly. Figures 5.3 and 5.4 represent diagramatically probe wavefunctions incident upon a crystal. The

figures shows a slice taken through the **R** plane and at depths $z = 0, 500$ and 1000Å. In figures 5.3a and 5.4a the probe is initially incident upon an atom site, whilst in figures 5.3b and 5.4b the probe is incident between atomic sites. The distance between the atoms in the **R** plane at Si[100] is 1.92Å, hence the probe (Gaussian width 1.5Å) does not significantly overlap the neighbouring atoms. Figure 5.3 shows how the incident probe develops as it travels through a crystal with no potential. This calculation is done by simply scaling the Fourier coefficients of the potential down by a factor of a 1000. In contrast figure 5.4 shows how the incident probe wavefunction changes as it travels through the crystal which contains a deforming potential (Si[100]).

As we should expect, the probe spreads out greatly when there is no potential, and shows no preference for where the probe is initially sited. Switching the potential back on, figure 5.4, and looking at the case where the probe is sited on an atomic site, figure 5.4a, we see that at 500Å the probe has spread out slightly, but it still does not overlap neighbouring atoms. In contrast for the probe sited between atoms, in figure 5.4b, the probe has spread out to a greater degree. Both cases though, figures 5.4a&b, show the incident probe being held together to a greater degree when compared to that for no potential, figures 5.3a&b. This can be understood in terms of the channelling or focusing of the wavefunction by the atomic strings. It is the crystal potential itself which attempts to hold the probe wavefunction together as it travels through the crystal. This occurs better for the tightly bound states of the potential than those less well bound. If we were to take a scan across the crystal (i.e. form a HAADF image) then the image contrast expected is that due to the *difference* in intensity (amplitude

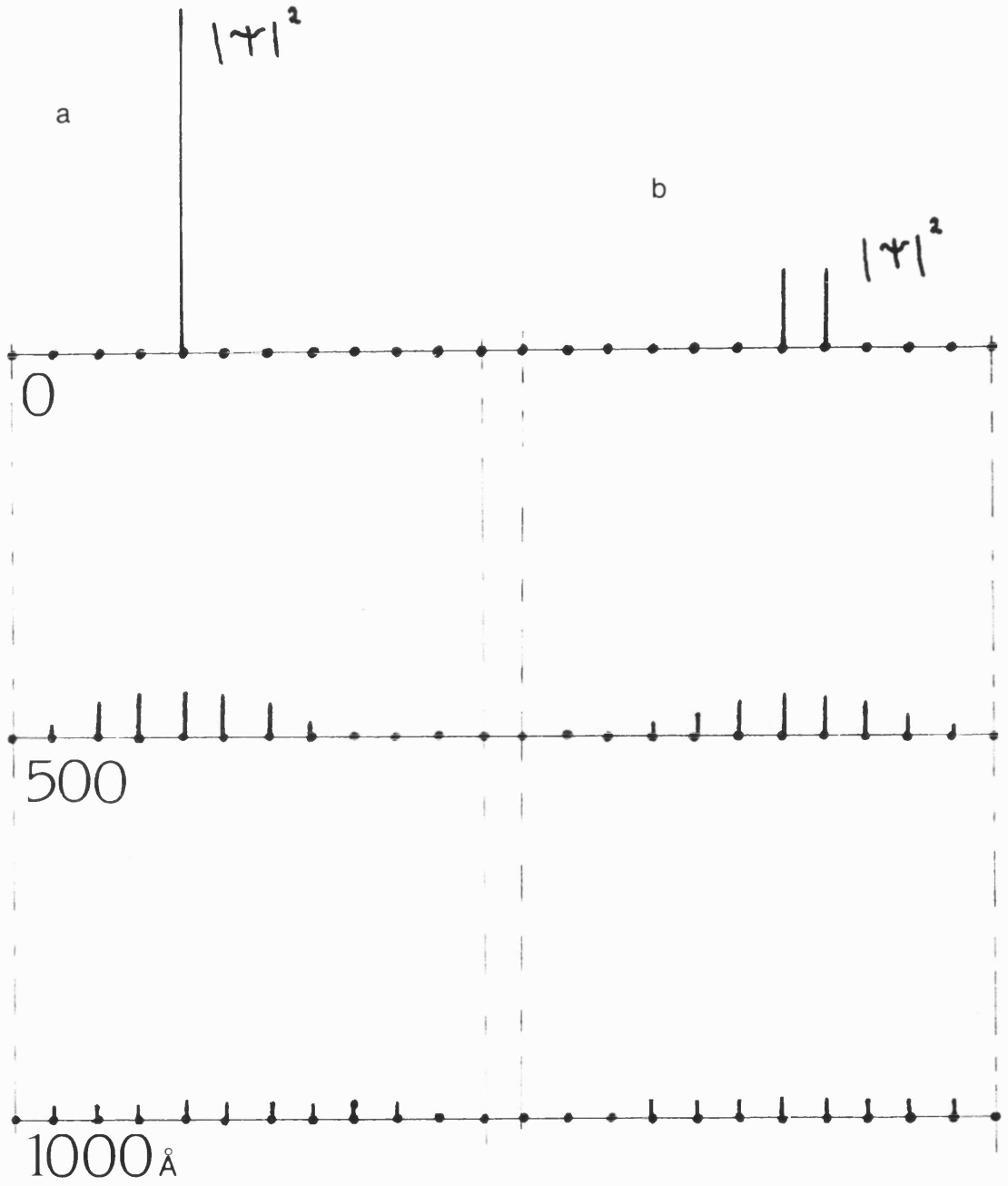


Figure 5.3 Probe intensity, incident upon a crystal with no potential, on the atomic sites. In figure 5.3a the probe is incident upon an atomic site, whilst in figure 5.3b it is incident between atomic sites. The figures show how the intensity has spread out at depths $z = 0, 500$ and $1000$Å.

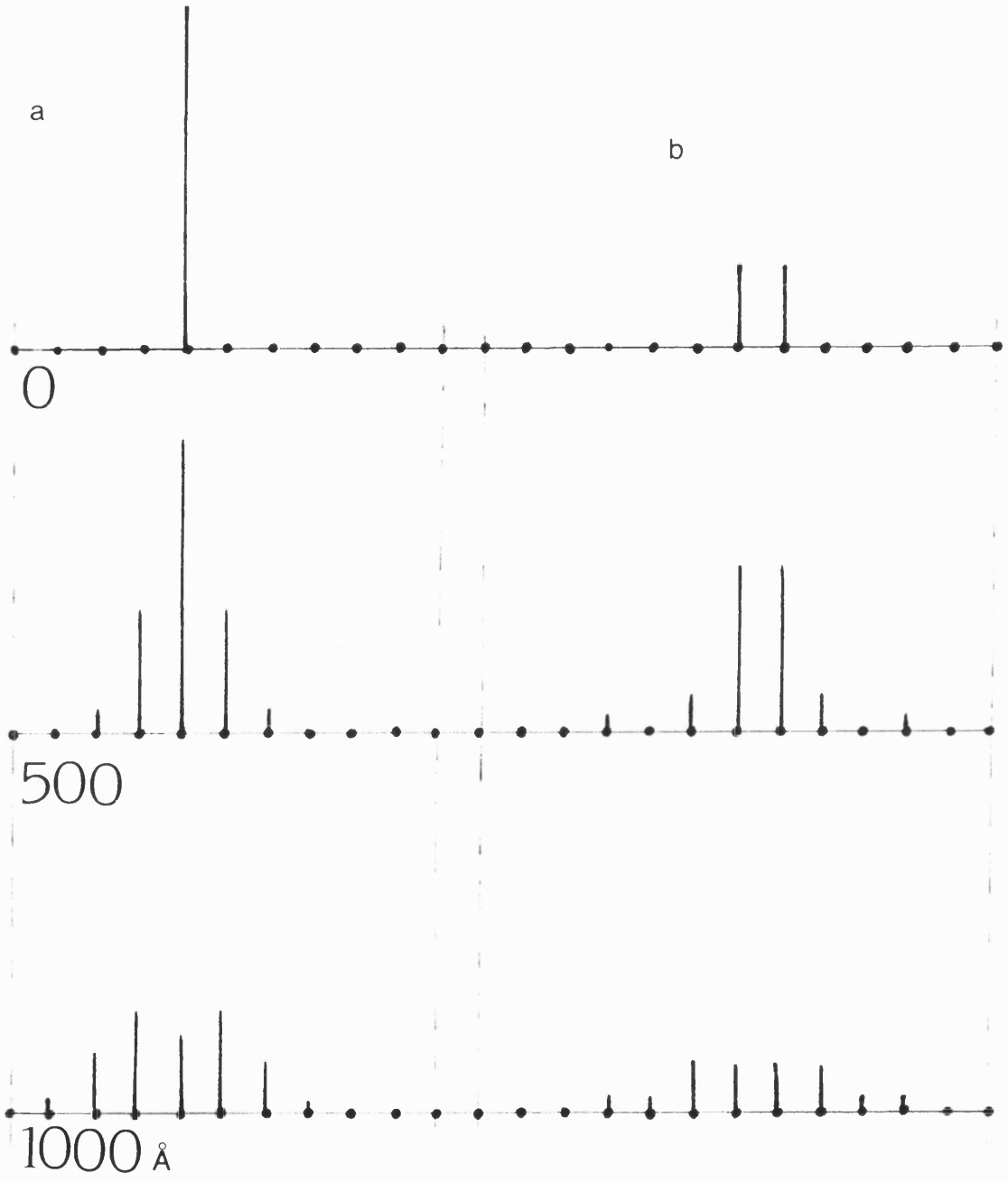


Figure 5.4 Probe intensity, incident upon a silicon crystal, on the atomic sites. In figure 5.4a the probe is incident upon an atomic site, whilst in figure 5.4b it is incident between atomic sites. The figures show how the intensity has spread out at depths $z = 0, 500$ and $1000$Å.

squared) of the wavefunction at the atomic sites for the probe centred on an atomic site to that when the probe is centred beween atomic sites. For a 500Å thick Silicon crystal this intensity ratio is of order $\sim 2$ (see figure 5.4). Thus we should expect to see the atomic strings being imaged in a HAADF pattern, with the intensity from the probe sited between atomic strings forming the background. The atomic strings are expected to to well resolved and completely distinguishable from each other provided the $1s$ states do not overlap.

At 1000Å similar results to those at 500Å are seen, though in travelling a further 500Å the incident wavefunction has spread out to a far greater extent in both cases. The ratio between the amplitude of the probe initially centered on an atomic site to that centered bewteen atomic sites is somewhat smaller than at 500Å, being of order $\sim 3/2$. But this is still large enough to give good, well resolved, though slightly reduced, image contrast.

Figures 5.5 and 5.6 are of the same form as figures 5.3 and 5.4 respectively, except now the Silicon crystal contains straight parallel tilted planes. The tilt is such that the atomic planes are shifted by three atomic spacings in the **R** plane in travelling through a depth of 1000Å. In this case, the $(2\bar{2}0)$ planes are tilted by $\theta = arctan(16.29/1000) \sim 0.016$ radians, whilst the respective $(2\bar{2}0)$ Bragg angle is $\theta_B \sim 0.017$. The tilt parameter is then from (5.5.3) $f \sim 1$. If the potential is switched off, figure 5.5, then as before there are no changes from figure 5.3. However if we examine the case where there is a potential (figure 5.6), then when the probe is initially centered on an atom site we see only a slight difference to that of figure 5.4a. This may be seen by comparing the spreading,

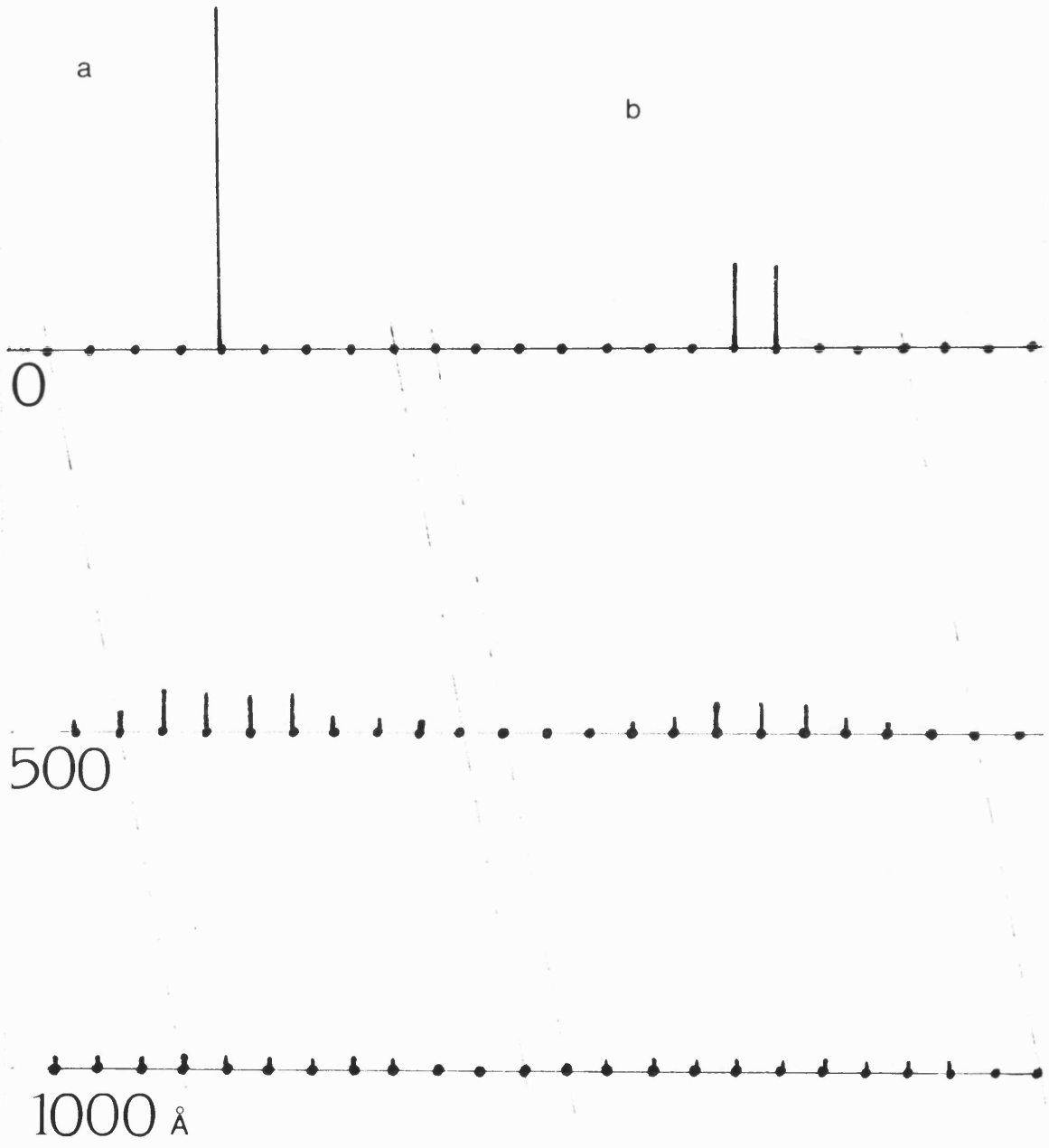


Figure 5.5 Probe intensity, incident upon a tilted crystal with no potential,on the atomic sites. In figure 5.5a the probe is incident upon an atomic site, whilst in figure 5.5b it is incident between atomic sites. The figures show how the intensity has spread out at depths $z = 0, 500$ and $1000$Å.

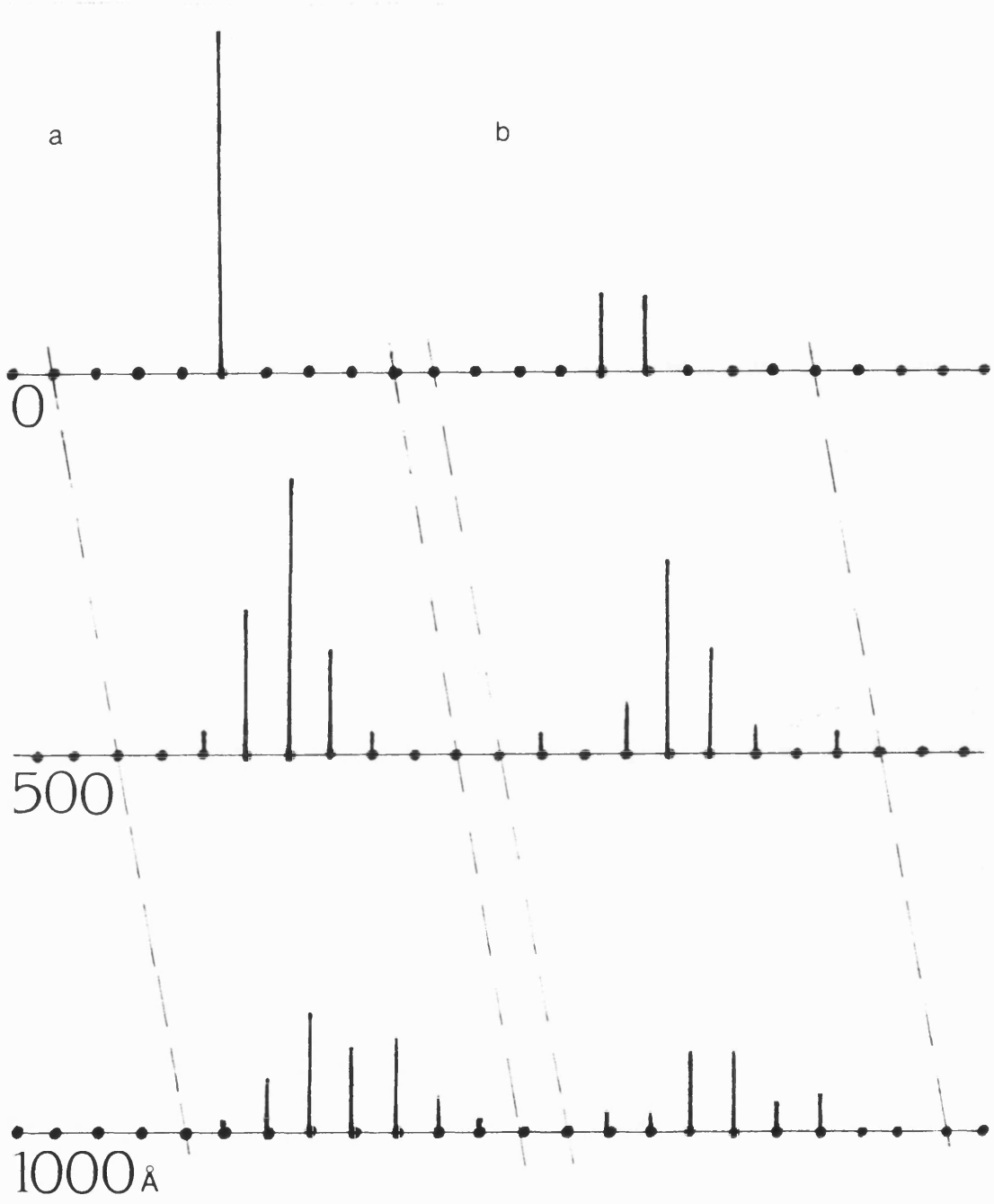


Figure 5.6 Probe intensity, incident upon a silicon crystal with tilted columns (tilt parameter $f \sim 1$), on the atomic sites. In figure 5.6a the probe is incident upon an atomic site, whilst in figure 5.6b it is incident between atomic sites. The figures show how the intensity has spread out at depths $z = 0, 500$ and $1000$Å.

shape and the amplitude of the untilted and tilted crystal wavefunctions. At 500Å the incident wavefunction has followed the tilted strings almost perfectly. By 1000Å the probe is still following the tilting quite well but has a small residue which has not followed the tilting. In contrast to this, when the probe is initially centered between atomic sites, figure 5.6b, the wavefunction does not follow the tilting so well. At 1000Å we see that the center of the wavefunction appears to have been shifted by 2, and not by 3, lattice spacings. There is thus a partial following of the tilting, which occurs in a complicated manner. This is because most of the intensity is initially focused between the atomic sites and there is a higher excitation of less bound states. The complicated nature of the wavefunction arises from the combination of the scattering by the less tightly bound states, which do not follow the tilting, and the tightly bound states which do.

From these calculations we can expect that the effect of tilting the planes on an HAADF image is to first spread out the image in the direction of the tilting and second to reduce the contrast. For crystals whose planes are only slightly tilted, $f \sim 0.1$ or less, the image is expected to show no differences from that of an untilted crystal. As the tilt angle becomes larger the HAADF image will start to lose contrast and become smeared.

Figures 5.7 to 5.10 show the computed first order adiabatic HAADF image of Si[100]. The crystal is 1000Å thick. They were calculated by use of (5.4.15). As for the LACBED patterns of chapter 4, the HAADF patterns (of this and the next section) consist of a 64 by 64 grid in which each square is shaded according to a scaled intensity at that point. The scaling is different for each pattern with

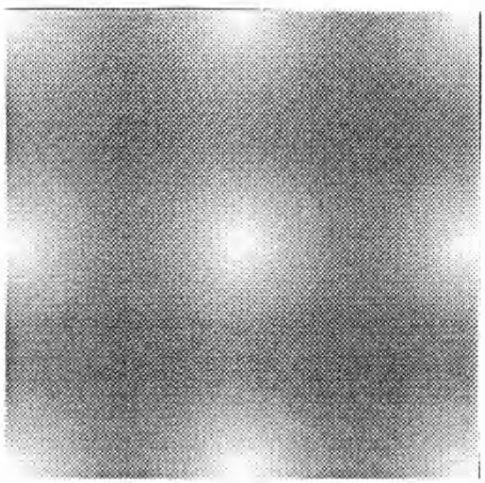

Figure 5.7 HAADF pattern for untilted Silicon crystal in the [100] direction.

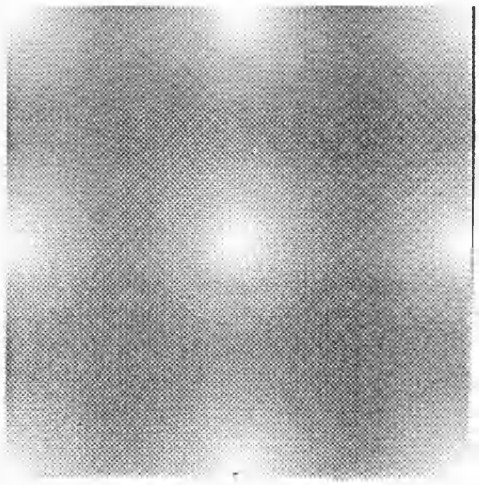

Figure 5.8 HAADF pattern of a Si[100]. The crystal planes have been tilted by $f = 0.1$.

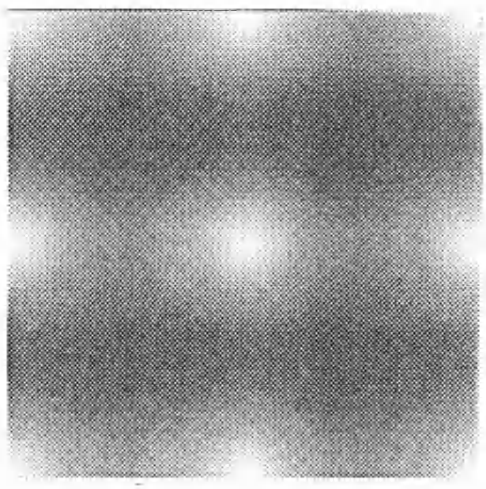

Figure 5.9 HAADF pattern of a tilted Silicon crystal in the [100] direction. The crystal planes have been tilted by $f = 0.5$.

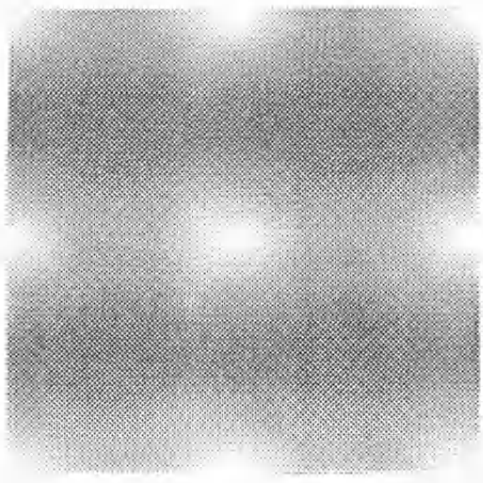

Figure 5.10 HAADF pattern of a tilted Silicon crystal in the [100] direction. The crystal planes have been tilted by $f = 1.0$.

the greatest intensity (scale=1) represented by a completely white square. Other intensities are then shaded relative to

this. Figure 5.7 shows the computed HAADF pattern for an untilted Silicon crystal in the [100] direction. The pattern shows that the atomic strings do not overlap and are well resolved. In figure 5.8 the atomic planes have been slightly tilted, by a tenth of a Bragg angle ($f = 0.1$). The pattern shows no noticable difference from that of the untilted pattern. Thus the intensity is channelled almost perfectly down the tilted atomic strings by the tightly bound states. Next in figure 5.9 we increase the tilt, so that it is now by half a Bragg angle ($f = 0.5$). The HAADF pattern again shows almost no differences from that of the untilted pattern, figure 5.7. There is a slight loss of contrast and spreading by 1000Å, which in an actual experimental micrograph would probably be unnoticable. Figure 5.10 shows an extreme example, where the tilt is by a whole Bragg angle ($f = 1.0$). The contrast is quite noticably reduced and the spreading become so great that the atomic strings are no longer individually resolved. These results indicate that not only do the tightly bound states channel the intensity down the atomic strings, so that they are well resolved, but that this is done so well that HAADF imaging can handle very large strains with little or no noticeable difference.

## 5.7 EXPERIMENTAL RESULTS.

Figure 5.11 shows a montage of Si[110] as a function of crystal tilt. The letters denote the crystal orientation relative to the large angle electron channelling pattern shown, which is formed by rocking the beam at the specimen and col-

lecting the high angle scattering. The point $G$ corresponds to the centre of a displaced 11 mrad objective aperture, and at this stage no image is present. The distance $A - C$ is approximately 5.5 mrad correspoding to $G_{111}$. All of the micrographs show the same image pattern formed, and this is that formed at the surface. HAADF imaging gives rise to a surface probe profile, which is then channelled through the crystal. The experimental results show that the major effect of tilt is to decrease the peak to background contrast in the image, though the form of the image remains the same.

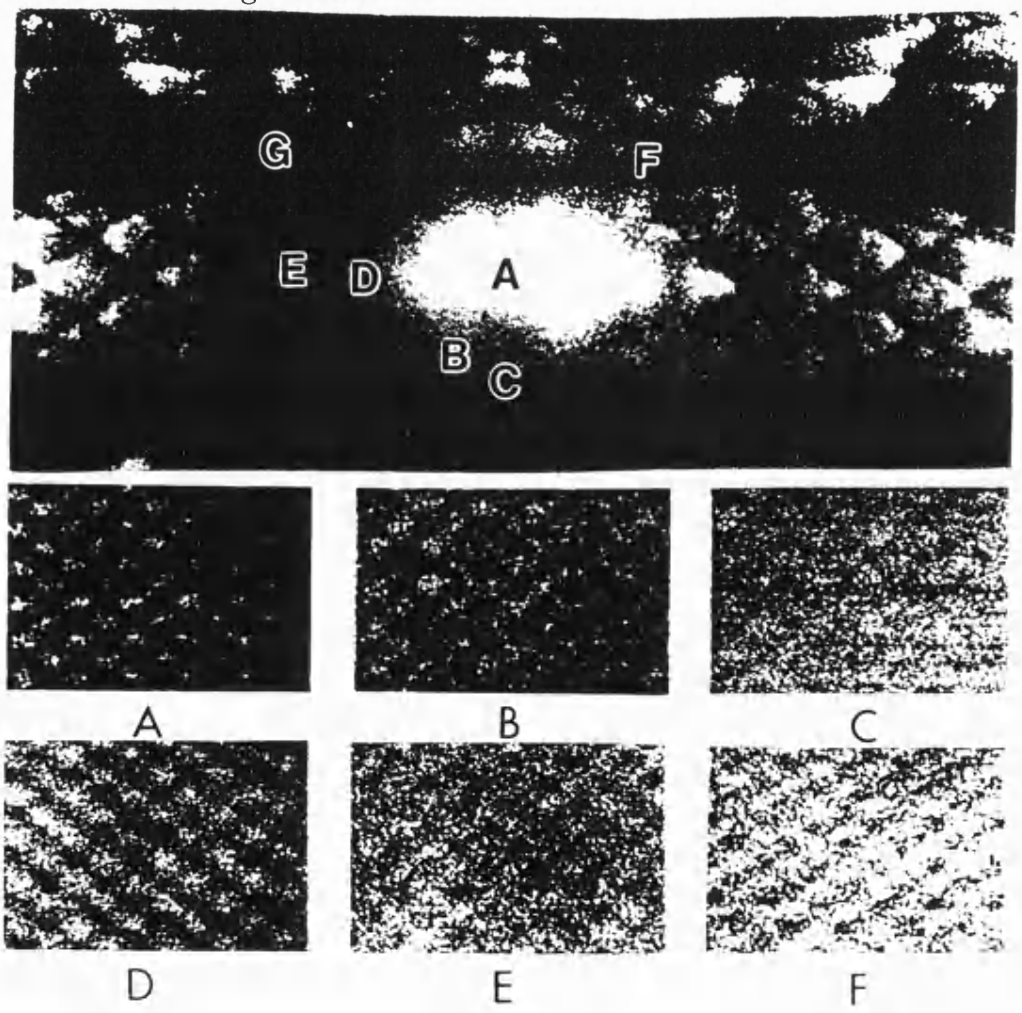


Figure 5.11 Montage of HAADF images of Si[110] taken as a function of crystal tilt (courtesy of D E Jesson). The images show how insensitive HAADF is to small strains. The effects of crystal tilt being to decrease the image contrast but not to change the image's form.

Figure 5.12 shows a HAADF micrograph of $Si/Si_6Ge_4$ superlattice structure which contains an edge dislocation in the Silicon. We can see that far away from the edge dislocation the image shows a clear unaffected pattern. It is only close to the centre of the dislocation, within a few (20 or less) atomic spacings, that the dislocation has any affect upon the image. There is also a fairly sharp boundary betweeen the affected and unaffected areas.

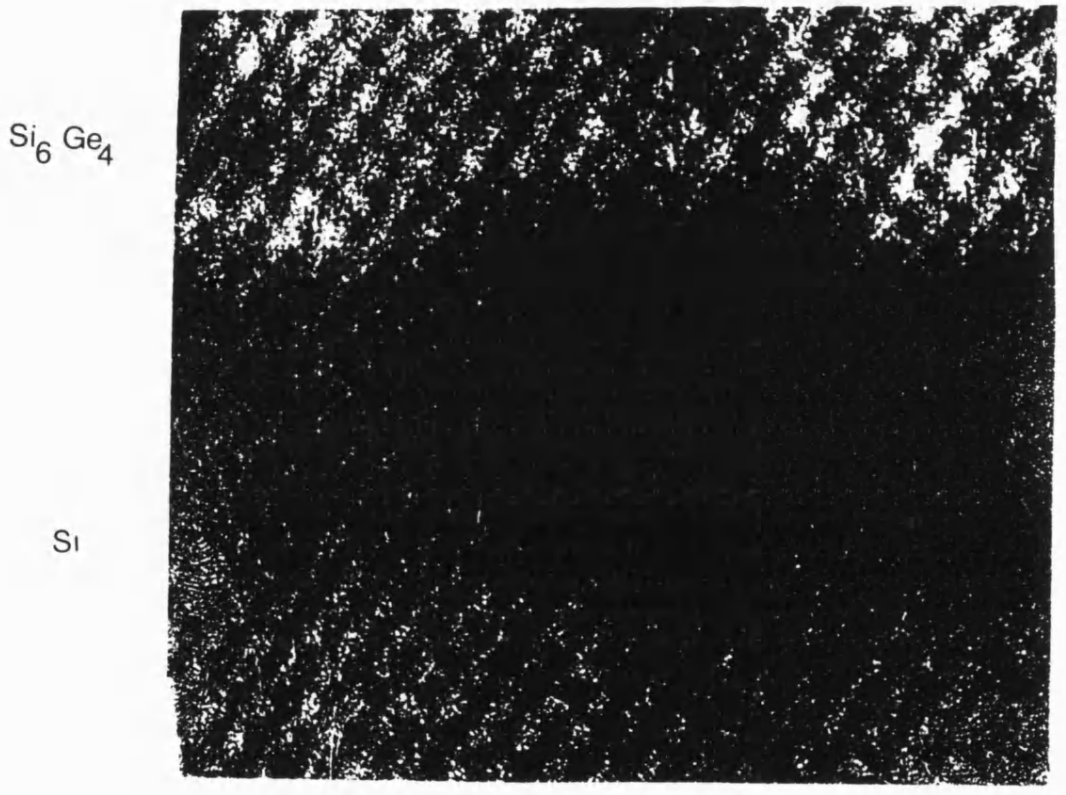


Figure 5.12 HAADF image of $Si$ $Si_6Ge_4$ which contains an edge dislocation (courtesy of D E Jesson). Although the dislocation clearly alters the image close to its core, away from the core centre the image appears relatively unaffected.

These experimental results hence confirm the prediction that HAADF imaging is fairly insensitive to small tilts or small strain fields. Both images show that

the image formed is that seen at the surface, and indicate that the channelling is done by the $1s$ states. Tilting the crystal simply reduces the excitation of the $1s$ states relative to the other states (background).

## 5.8 CONCLUSIONS.

Within this chapter we have concerned ourselves with the effects of strains on HAADF imaging. In section 5.4 an expression for the HAADF intensity from a strained crystal was derived. Although this expression may be found exactly (or to any desired accuracy), in practice approximation methods are used. The adiabatic iteration scheme was shown to be useful and illuminating for crystals with small strains. We have seen that the electron intensity in HAADF imaging attempts to follow any lattice bending and does so most successfully for the tightly bound $1s$ states. For small strains ($f \leq 0.2$ in the example discussed) the $1s$ states are almost completely successful in following the bending, though as the strain increases they are increasingly scattered into the background. For small strains this implies that HAADF imaging will be insensitive to small deformations and that the atomic resolution will be determined by what the probe sees at the entrance surface of the crystal subsequently the atomic strings will effectively carry the probe with them.

# CHAPTER 6

# CONCLUSION

In this thesis we have investigated the effects of long range strain fields in crystalline materials upon HEED images. In doing this, use was made of the adiabatic iteration technique (Berry 1987). This has been illustrated by application to two microscopic techniques, LACBED and HAADF imaging in STEM.

In chapter 2 the Howie–Whelan equations (2.6.1) were derived by making various standard approximations. The Howie–Whelan equations are general, making no mention of the particular specimen studied or of the nature of the deforming strain field. They formed the basis for predicting and interpreting HEED images and diffraction patterns in this thesis.

A general adiabatic iteration scheme was introduced in chapter 3. This is based upon that of Berry (1987) but is derived in matrix form. This is particularly well suited to HEED, as the Howie–Whelan equations can naturally be written in such a form and because it allows a conventional Bloch wave interpretation. The scheme is general and is applicable to areas other than TEM. Although only the case of a hermitian Hamiltonian was discussed, the technique may be extended to accommodate non-hermitian Hamiltonians (as illustrated in section 4.9 for the $2 \times 2$ matrix case). The scheme, like that of Berry, is based around the geometric phase, but unlike Berry's, the path taken by the evolving system is general and is not necessarily closed. Although the scheme is adiabatic it can take into account non-adiabatic terms through a slowness parameter, $\xi$, which is small. Each iteration, $n$, produces a better approximation over its predessor by including terms proportional to $\xi^{n-1}$. However, except for simple cases, the

adiabatic iteration scheme will eventually breakdown and produce worsening approximations.

We have seen in chapter 4 that the simple 2-beam Howie–Whelan equations can be computationally solved to within some small negligible error, and that adiabatic iteration may be used to form approximations to such exact solutions. The advantage of using adiabatic iteration is that it allows an analytical approximation to be formed which may be used to gain insights into the underlying process in HEED and being iterable allows improvememts to be made. The 2-beam case gives general insights into adiabatic iteration without the complexity of the n-beam case. For the case of a crystal containing a screw dislocation, adiabatic iteration is well suited as the electron wave proporgation can be interpreted in terms of the geometric phase. This was shown to be illuminating in explaining the fringe bending rule in LACBED. The scheme is adaptable and can be extended to include such problems as absorption or tilted strain fields. There are however a number of problems in using adiabatic iteration in TEM. Although a good approximation can be formed where the columns bend slowly, wherever they bend rapidly the initial adiabatic approximation fails badly. Moreover each sucessive iteration makes the mathematics involved more complex, harder to interpret and to include rapid changes a large number of iterations must be made. Thus, for example, adiabatic iteration is not suited to studying dislocation cores.

The advantage in using adiabatic iteration to approximate the solutions to the n-beam Howie–Whelan equations lies both in allowing analytic approximations to be formed and in the saving of computer time and memory. The difficulties of the 2-beam case are of course greatly increased and it is only practical to

use the first iteration. Then any strain field core can not be approached closely and regions where the technique may be used are much restricted. However in chapter 5 the HAADF imaging technique in STEM was discussed, and examples were given to illustrate the advantages of adiabatic iteration. There the exact solutions to the general Howie–Whelan equations are unpractical to solve and approximation methods can greatly reduce the necessary computer time and memory needed. In particular it was shown that adiabatic iteration can be used to demonstrate and explain why HAADF imaging is less sensitive to strain fields than is conventional TEM.

## APPENDIXES.

### Appendix A.

Here we shall derive a set of solutions to the instantaneous Schrödinger equation of the hermitian Hamiltonian (3.1.39).

The instantaneous Schrödinger equation may be written as

$$\begin{aligned} z_0 N^j_{1_0} + r_0 \exp(i\varphi_0) N^j_{2_0} &= \lambda^j_0 N^j_{1_0} \\ r_0 \exp(-i\varphi_0) N^j_{1_0} - z_0 N^j_{2_0} &= \lambda^j_0 N^j_{2_0}, \end{aligned} \tag{A1}$$

which may be rewritten as

$$\frac{N_{1_0}}{N^j_{2_0}} = \frac{\lambda^j_0 + z_0}{r_0} \exp(i\varphi_0) = \frac{r_0}{\lambda^j_0 - z_0} \exp(i\varphi_0). \tag{A2}$$

Equation (A2) implies that the eigenvalues are given by

$$\lambda^j_0 = \pm\sqrt{z_0^2 + r_0^2}. \tag{A3}$$

Here we shall take state $j = 1$ to be the positive component and state $j = 2$ to be the negative component.

From the normalisation condition we have that

$$\begin{pmatrix} N^{j^*}_{1_0} & N^{j^*}_{2_0} \end{pmatrix} \begin{pmatrix} N^j_{1_0} \\ N^j_{2_0} \end{pmatrix} = 1. \tag{A4}$$

Substituting (A2) into (A4) implies that

$$|N^j_{1_0}| = \frac{1}{\sqrt{2}} \left(1 + \frac{z_0}{\lambda^j_0}\right)^{\frac{1}{2}} \tag{A5a}$$

$$|N^j_{2_0}| = \frac{1}{\sqrt{2}} \left(1 - \frac{z_0}{\lambda^j_0}\right)^{\frac{1}{2}}. \tag{A5b}$$

In order to have two distinct solutions, we shall define the square root in (A5b) to be positive for j=1 and negative for j=2. The phase factor is defined such that it satisfies (A1), giving the instantaneous eigenstates as

$$\begin{pmatrix} N^j_{1_0} \\ N^j_{2_0} \end{pmatrix} = \frac{1}{\sqrt{2}} \begin{pmatrix} \exp(i\varphi_0/2)(1+\frac{z_0}{\lambda^j_0})^{\frac{1}{2}} \\ \pm\exp(-i\varphi_0/2)(1-\frac{z_0}{\lambda^j_0})^{\frac{1}{2}} \end{pmatrix}. \tag{A6}$$

Again the +ve sign refers to $j = 1$ and the -ve sign to $j = 2$. Equation (A6) defines the instantaneous eigenstates up to a time independent phase factor. They are made unique by insisting that they are parallel transported, obeying (3.1.5). If we define the time dependent phase to be $\gamma^j_0(t)$, the parallel transpored instantaneous eigenstates are

$$\begin{pmatrix} \tilde{N}^j_{1_0} \\ \tilde{N}^j_{2_0} \end{pmatrix} = \frac{1}{\sqrt{2}} \exp(i\gamma^j_0) \begin{pmatrix} \exp(i\varphi_0/2)(1+\frac{z_0}{\lambda^j_0})^{\frac{1}{2}} \\ \pm\exp(-i\varphi_0/2)(1-\frac{z_0}{\lambda^j_0})^{\frac{1}{2}} \end{pmatrix}. \tag{A7}$$

An expression for $\gamma^j_0$ can be found by substituting (A7) into (3.1.5). Differentiating (A7) with respect to time gives

$$\begin{pmatrix} \dot{\tilde{N}}^j_{1_0} \\ \dot{\tilde{N}}^j_{2_0} \end{pmatrix} = \left(i\dot{\gamma}^j_0 \pm i\frac{\dot{\varphi}_0}{2}\right) \begin{pmatrix} \tilde{N}^j_{1_0} \\ \tilde{N}^j_{2_0} \end{pmatrix} + \frac{\exp(i\gamma^j_0 \pm i\varphi_0/2)}{2\sqrt{2}} \left[\frac{d}{dt}\frac{z_0}{\lambda^j_0}\right] \begin{pmatrix} (1+\frac{z_0}{\lambda^j_0})^{-\frac{1}{2}} \\ \mp(1-\frac{z_0}{\lambda^j_0})^{-\frac{1}{2}} \end{pmatrix} \tag{A8}$$

where

$$\frac{d}{dt}\frac{z_0}{\lambda^j_0} = \frac{\dot{z}_0}{\lambda^j_0} - \frac{z_0}{(\lambda^j_0)^2}\dot{\lambda}^j_0 = \frac{r_0}{(\lambda^j_0)^3}(\dot{z}_0 r_0 - \dot{r}_0 z_0). \tag{A9}$$

Subsituting (A7), (A8) and (A9) into (3.1.5) gives

$$\begin{aligned} (\,\tilde{N}^{j^*}_{1_0} \quad \tilde{N}^{j^*}_{2_0}\,) \begin{pmatrix} \dot{\tilde{N}}^j_{1_0} \\ \dot{\tilde{N}}^j_{2_0} \end{pmatrix} &= i\dot{\gamma}^j_0 + i\frac{\dot{\varphi}_0}{2}(\tilde{N}^{j^*}_{1_0}\tilde{N}^j_{1_0} - \tilde{N}^{j^*}_{2_0}\tilde{N}^j_{2_0}) \\ &= i\dot{\gamma}^j_0 + i\frac{z_0\dot{\varphi}_0}{2\lambda^j_0}. \end{aligned} \tag{A10}$$

But the parallel transport rule, (3.1.5), implies that this is simply equal to zero. Thus (A10) gives

$$\gamma^j_0(t) = -\int_0^t \frac{z_0}{\lambda^j_0}\dot{\varphi}_0 \, dt'. \tag{A11}$$

Equation (A7) together with (A3) and (A11) give a complete solution to the 2-beam instantaneous Schrödinger equation (A1).

## Appendix B.

An expression for the off-diagonal terms in the 2-beam case, (3.1.46), will now be derived. These are given by

$$i\sum_{l}\tilde{N}_{l_0}^{j'^*}\dot{\tilde{N}}_{l_0}^{j} = i\begin{pmatrix}\tilde{N}_{1_0}^{j'^*} & \tilde{N}_{2_0}^{j'^*}\end{pmatrix}\begin{pmatrix}\dot{\tilde{N}}_{1_0}^{j}\\ \dot{\tilde{N}}_{2_0}^{j}\end{pmatrix}, \quad j'\neq j. \tag{B1}$$

Because we are looking at $j'\neq j$, we shall write (A9) as

$$\frac{d}{dt}\left(\frac{z_0}{\lambda_0^j}\right) = -\frac{r_0}{(\lambda_0^{j'})^3}(r_0\dot{z}_0 - \dot{r}_0 z_0). \tag{B2}$$

Now because the eigenstates are orthogonal we have that

$$\tilde{N}_{1_0}^{j'^*}\tilde{N}_{1_0}^{j} + \tilde{N}_{2_0}^{j'^*}\tilde{N}_{2_0}^{j} = 0, \tag{B3}$$

and for the two beam case that

$$\begin{aligned}\tilde{N}_{1_0}^{j'^*}\tilde{N}_{1_0}^{j} - \tilde{N}_{2_0}^{j'^*}\tilde{N}_{2_0}^{j} &= \frac{\exp(i\{\gamma_0^j-\gamma_0^{j'}\})}{2}\left((1+\tfrac{z_0}{\lambda_0^{j'}})^{\frac{1}{2}}(1+\tfrac{z_0}{\lambda_0^{j}})^{\frac{1}{2}} + (1-\tfrac{z_0}{\lambda_0^{j'}})^{\frac{1}{2}}(1-\tfrac{z_0}{\lambda_0^{j}})^{\frac{1}{2}}\right)\\ &= \frac{\exp(i\{\gamma_0^j-\gamma_0^{j'}\})}{2}\left((1+\tfrac{z_0}{\lambda_0^{j'}})^{\frac{1}{2}}(1-\tfrac{z_0}{\lambda_0^{j'}})^{\frac{1}{2}} + (1-\tfrac{z_0}{\lambda_0^{j'}})^{\frac{1}{2}}(1+\tfrac{z_0}{\lambda_0^{j'}})^{\frac{1}{2}}\right)\\ &= \frac{r_0}{|\lambda^{j'}|}\exp(-2i\gamma_0^{j'}).\end{aligned} \tag{B4}$$

Now using (A8), (B2), (B3) and (B4), (B1) can more simply be expressed as

$$\begin{aligned}i\sum_{l}\tilde{N}_{l_0}^{j'^*}\dot{\tilde{N}}_{l_0}^{j} &= \frac{ir_0}{2}\left(\frac{i\dot{\varphi}_0}{|\lambda_0^{j'}|} - \frac{(r_0\dot{z}_0-\dot{r}_0z_0)}{2(\lambda_0^{j'})^3}\left[\left(\frac{1+\frac{z_0}{\lambda_0^{j'}}}{1+\frac{z_0}{\lambda_0^{j}}}\right)^{\frac{1}{2}} + \left(\frac{1-\frac{z_0}{\lambda_0^{j'}}}{1-\frac{z_0}{\lambda_0^{j}}}\right)^{\frac{1}{2}}\right]\right)\exp(-2i\gamma_0^{j'})\\ &= \frac{ir_0}{2}\left(\frac{i\dot{\varphi}_0}{|\lambda_0^{j'}|} - \frac{(r_0\dot{z}_0-\dot{r}_0z_0)}{2(\lambda_0^{j'})^3}\left[\left(\frac{\lambda_0^{j'}+z_0}{\lambda_0^{j'}-z_0}\right)^{\frac{1}{2}} + \left(\frac{\lambda_0^{j'}-z_0}{\lambda_0^{j'}+z_0}\right)^{\frac{1}{2}}\right]\right)\exp(-2i\gamma_0^{j'})\\ &= \frac{ir_0}{2}\left(\frac{i\dot{\varphi}_0}{|\lambda_0^{j'}|} - \frac{(r_0\dot{z}_0-\dot{r}_0z_0)}{2(\lambda_0^{j'})^3}\frac{2|\lambda_0^{j'}|}{r_0}\right)\exp(-2i\gamma_0^{j'})\\ &= \frac{i}{|\lambda_0^{j'}|}\left(\frac{ir_0\dot{\varphi}_0}{2} - \frac{(r_0\dot{z}_0-\dot{r}_0z_0)}{2\lambda_0^{j'}}\right)\exp(-2i\gamma_0^{j'}).\end{aligned} \tag{B5}$$

Note that by taking the absolute values in the square roots we are insisting that the instantaneous eigenstates remain hermitian, i.e. $\sum_G N_G^{j'^*} \dot{N}_G^j = -\left(\sum_G N_G^{j^*} \dot{N}_G^{j'}\right)^*$. Equation (B5) gives the 2-beam off-diagonal terms.

## Appendix C.

We shall here derive an expression for the adiabatic second order diffracted intensity from a crystal containing a symmetric displacement function $\phi$.

From (4.7.9b), we find upon substituting for $C_{i_0}^j$ and $C_{i_1}^j$ that

$$\chi = \frac{i}{2}\left[(1+i)\left(1-\frac{x-\dot{\phi}}{2s_0^1}\right)^{1/2} - (1-i)\left(1+\frac{x-\dot{\phi}}{2s_0^1}\right)\frac{\beta|\ddot{\phi}|}{2(2s_0^1)^3}\right] \qquad (C1)$$

and

$$\omega = \frac{1}{2}\left[(1+i)\left(1-\frac{x+\dot{\phi}}{2s_0^1}\right)^{1/2} + (1-i)\left(1-\frac{x-\dot{\phi}}{2s_0^1}\right)\frac{\beta|\ddot{\phi}|}{2(2s_0^1)^3}\right]. \qquad (C2)$$

Similarly

$$\eta = \frac{-i}{2}\left[(1-i)\left(1+\frac{x-\dot{\phi}}{2s_0^1}\right)^{1/2} + (1+i)\left(1-\frac{x-\dot{\phi}}{2s_0^1}\right)\frac{\beta|\ddot{\phi}|}{2(2s_0^1)^3}\right] \qquad (C3)$$

and

$$\mu = -\frac{1}{2}\left[(1-i)\left(1-\frac{x-\dot{\phi}}{2s_0^1}\right)^{1/2} - (1+i)\left(1+\frac{x-\dot{\phi}}{2s_0^1}\right)\frac{\beta|\ddot{\phi}|}{2(2s_0^1)^3}\right]. \qquad (C4)$$

Hence the respective products, ignoring all third order and higher terms, are

$$\chi\omega = \frac{-\beta}{2(2s_0^1)}\left[1+i\frac{x|\ddot{\phi}|}{(2s_0^1)^3}\right] \qquad (C5)$$

and

$$\eta\mu = \frac{\beta}{2(2s_0^1)}\left[1-i\frac{x|\ddot{\phi}|}{(2s_0^1)^3}\right]. \qquad (C6)$$

Substituting (C5) and (C6) into (4.7.9a), gives the second order wavefunction as

$$\begin{aligned}\psi_{\mathbf{G}}(1) =& \frac{-\beta}{2s_0^1}\left[\frac{\exp(i\vartheta)-\exp(-i\vartheta)}{2}+i\frac{x|\ddot{\phi}|}{2(2s_0^1)^3}\left(\frac{\exp(i\vartheta)+\exp(-i\vartheta)}{2}\right)\right] \\ =& \frac{-i\beta}{2s_0^1}\left[sin(\vartheta)+\frac{x|\ddot{\phi}|}{(2s_0^1)^3}\cos(\vartheta)\right],\end{aligned} \tag{C7}$$

where

$$\vartheta = \frac{1}{2}\int_{-1}^{1}\sqrt{(x-\dot{\phi})^2+\beta^2}\;d\theta.$$

Thus the adiabatic approximation for the diffracted intensity, again ignoring all third order and higher terms, is

$$I_{\mathbf{G}}(1) = \frac{\beta^2\sin^2(\vartheta)}{(2s_0^1)^2}+\frac{2\beta^2 x|\ddot{\phi}|\sin(\vartheta)\cos(\vartheta)}{(2s_0^1)^5}. \tag{C8}$$

## REFERENCES


Ashcroft N.W. and Mermin D.N., *Solid state physics*, Holt–Saunders, New York, 1976.

Berry M.V., J. Phys. C **4**, 697, 1971.

Berry M.V., Proc. Roy. Soc. **A392**, 45, 1984.

Berry M.V., Proc. Roy. Soc. **A414**, 31, 1987.

Bird D.M., J. Electron Microscopy Tech. **13**, 77, 1989.

Bird D.M. and King Q.A., Acta. Cryst. **A46**, 202, 1990.

Bird D.M. and Preston A.R., Phy. Rev. Lett. **61**, 2863, 1988.

Bohm D., *Quantum theory*, Prentice-Hall, New Jersey 1951.

Born M. and Fox V., Z. Phys. **51**, 165, 1928.

Buseck P., Cowley J. and Eyring L. *High-Resolution Transmission Electron Microscopy and Associated Techniques*, Oxford University Press, New York, 1988.

Buxton B.F., Eades J.A., Steeds J.W., and Rackham G.M., Phil. Trans. Roy. Soc. **281**, 171, 1976.

Carpenter R.W. and Spence J.C.H., Acta. Cryst. **A48**, 55, 1982.

Carpenter R.W. and Spence J.C.H., J. Microsc. **136**, 165, 1984.

Carter C.B. and Hirsch P.B., Phil. Mag. **A35**, 1509,1977.

Cherns D., Kiely C.J. and Preston A.R., Ultramicrosopy **24**, 355, 1988.

Cherns D. and Preston A.R., Proc. $XI^{th}$ Int. Congr. on Electron Microscopy, Kyoto, Japan, pp. 721, 1986.

Cherns D. and Preston A.R., J. Electron Microscopy Tech. **13**, 111, 1989.

Chisholm M.F. and Pennycook S.J., Nature **351**, 47, 1991.

Cowley J., *Diffraction Physics*, North-Holland, Amsterdam, 1981.

Cowley J.M. and Moodie A.F., Acta. Cryst. **A10**, 609, 1957.

Crewe A.V., Langmora J. P. and Isaacson M. S., in *Phsyical Aspects of Electron Microscopy and Microbeam Analysis*, eds: B. M. Siegal and D. R. Beaman, Wiley, New York, 47, 1975.

Crewe A.V. and Wall J., Optic **30**, 461, 1970.

Dederichs P.H., Solid State Physics **27**, 135, 1972.

Donald A. and Craven A.J., Phil. Mag. **A39**, 1, 1980.

Doyle P.A. and Turner P.S., Acta. Cryst. **A24**, 390, 1968.

Eaglesham D.J., J. Electron Microscopy Tech. **13**, 66, 1989.

Friedel J., *Dislocations*, Pergamon Press, Oxford, 1964.

Fujiwara K., J. Phys. Soc. Japan **16**, 2226, 1961.

Fujiwara K., J. Phys. Soc. Japan **17**, Suppl. BII, 118, 1962.

Fung K.K., Ultramicrosopy **17**, 81, 1985.

Goodhew P.J. and Humphreys F.J., *Electron microscopy and analysis*, Tayler and Francis, London, 1988.

Goodman P. and Moodie A.F., Acta. Cryst. **A30**, 280, 1974.

Hall C.R. and Hirsch P.B., Proc. Roy. Soc. **A286**, 158, 1965.

Hashimoto H., Howie A. and Whelan M.J., Proc. Roy. Soc. **A269**, 80, 1962.

Hirsch P.B., Howie A., Nicholson R.B., Pashley D.W. and Whelan M.J., *Electron microscopy of thin crystals*, Butterworths, London, 1977.

Howie A., Proc. Roy. Soc. **A271**, 268, 1963.

Howie A., J. Micosc. **117**, 11, 1979.

Howie A. and Basinski Z.S., Phil. Mag. **17**, 1039, 1968.

Howie A. and Whelan M.J., Proc. Roy. Soc. **A263**, 217, 1961.

Humble P., in *Introduction to Analytical Electron Microscopy*, eds Hren J.J. Goldstein J.I. and Joy D.C., Plenum, New York, 551, 1979.

Humphreys C.J., Rep Prog. Phys. **42**, 1825, 1979.

Gibson J.M. and Howie A., Chem. Scr. **14**, 109, 1978.

Jesson D.E. ,Pennycook S.J. and Baribeau J.M., Phys. Rev. Lett. **66**, 750, 1991.

Jones P.M., Rackham G.M. and Steeds J.W., Proc. Roy. Soc. **A354**, 197, 1977.

Kirkland E.J., Loane R.F. and Silcox J., Ultramicroscopy **23**, 77, 1987.

Loane R.F., Kirkland E.J. and Silcox J., Acta. Cryst. **A44**, 912, 1988.

Lu, G., Wen J.G., Zhang W. and Wang R., Acta. Cryst. **A46**, 103, 1990.

Messiah A., *Quantum Mechanics II*, North-Holland, Amsterdam, 1966.

Metherell A.J.F, in *Electron microscopy in Material Science*, eds: Valdre U. and Ruedl E., Commission of the European Communities, 397, 1976.

Pennycook S.J., Ultramicroscopy **30**, 58, 1989.

Pennycook S.J., Berger S.D. and Culbertson J., J. Microsc. **144**, 229, 1986.

Pennycook S.J. and Boater L.A., Nature **366**, 565, 1988.

Pennycook S.J. and Jesson D.E., Phys. Rev. Lett. **64**, 938, 1990.

Pennycook S.J. and Jesson D.E., Phys. Rev. Lett. **67**, 765, 1991.

Pennycook S.J. and Jesson D.E., Ultramicroscopy **37**, 14, 1991.

Radi, G., Acta. Cryst. **A26**, 41, 1970.

Ray I.L.F. and Cockayne D.J.H., Proc. Roy. Soc. **A325**, 543, 1971.

Reimer L., *Transmission electron microscopy*, Springer–Verlag, Berlin, 1984.

Rez, P., Phys. Stat. Sol. **A55**, K79, 1970.

Rez, P., Humphreys C.J. and Whelan M.J., Phil. Mag. **A35**, 81, 1977.

Riley K.F., *Mathematical methods for the Physical Sciences*, Cambridge University Press, London, 1974.

Schiff L.I., *Quantum Mechanics*, McGraw–Hill, Tokyo, 1968.

Smith G.H. and Burge R.E. Acta. Cryst. **A15**, 182, 1962.

Steeds J.W., in *Introduction to Analytical Electron Microscopy*, eds Hren J.J. Goldstein J.I. and Joy D.C., Plenum, New York, 387, 1979.

Tanaka M., J. Electron Microscopy Tech. **13**, 27, 1989.

Tanaka M., Saito R., Ueno K. and Harada Y., J. Electron Microscopy **29**, 408, 1980.

Tanaka M., Terauchi M. and Kaneyama T., *Convergent-Beam Electron Diffraction*, JEOL-Maruzen, Tokyo, 1988.

Vincent R., J. Electron Microscopy Tech. **13**, 40, 1989.

Vincent R., Bird D.M. and Steeds J.W., Phil. Mag. **A50**, 745, 1984a.

Vincent R., Bird D.M. and Steeds J.W., Phil. Mag. **A50**, 765, 1984b.

Vincent R., Preston A.R. and King M.A., Ultramicroscopy **24**, 409, 1988.

Wang Z.L. and Cowley J.M., Ultramicroscopy **31**, 437, 1989.

Wang Z.L. and Cowley J.M., Ultramicroscopy **32**, 275, 1990.

Wen J.G., Wang R. and Lu G., Acta. Cryst. **A45**, 422, 1989.

Wilkens M., Rühle M. and Haüssermann F., Phys. Status Solidi **22**, 689, 1967.

Xu P., Kirkland E.J. and Silcox J., Ultramicroscopy **32**, 93, 1990.

Yoshioka H., J. Phys. Soc. Japan **12**, 618, 1957.

Ziman J.M., *The Principles of the Theory of Solids*, Cambridge University Press, Cambridge, 1979.

Zuo J.M., Spence J.C.H. and O Keeffe M., Phys. Rev. Lett. **61**, 353, 1988.